Master's thesis

NTNU
Norwegian University of Science and Technology
Faculty of Natural Sciences
Department of Physics

Fredrik Engelschiøn Akre

Spectral properties of quantum particles in fractal potentials

Master's thesis in Applied Physics and Mathematics
Supervisor: Pietro Massignan & Jon Andreas Støvneng
Co-supervisor: Grigori Astrakharchik
June 2023

NTNU
Norwegian University of Science and Technology

UPC
UNIVERSITAT POLITÈCNICA DE CATALUNYA

Fredrik Engelschiøn Akre

Spectral properties of quantum particles in fractal potentials

Master's thesis in Applied Physics and Mathematics
Supervisor: Pietro Massignan & Jon Andreas Støvneng
Co-supervisor: Grigori Astrakharchik
June 2023

Norwegian University of Science and Technology
Faculty of Natural Sciences
Department of Physics

NTNU
Norwegian University of Science and Technology

UPC
UNIVERSITAT POLITÈCNICA DE CATALUNYA

Preface

This thesis is the final work of a five-year-long combined master's degree program in Applied Physics and Mathematics with a focus on theoretical physics and quantum mechanics. The master's program is administrated by the Norwegian University of Science and Technology (NTNU), and this thesis is written in collaboration with the Polytechnic University of Catalonia (UPC). The thesis is a continuation of the work started by Akre (2023).

The extended lockdown due to the COVID-19 pandemic became a time for discovery for me. I was very intrigued, learning about the properties of fractal structures in the context of chaos and dynamical systems. I spent time reading and writing small programs generating fractals and probing basic properties. In university, I have specialized in quantum physics and condensed matter theory. Having just discovered this world of fractals, I was eager to research correlations between quantum physics, chaos theory and fractals. However, I soon realized that much is still uncharted in this interdisciplinary field of physics, and this became the outset of this thesis.

I would like to thank my supervisor Pietro Massignan who has guided me during the past year, both in the work of this thesis and in my coming to Barcelona. I also thank Jon Andreas Støvneng for his guidance and help throughout this thesis. I want to thank the talented and gracious student advisor Brit Wenche Meland for all her support during the past years. Finally, I thank my fiancée Elsie B. Tandberg for her unwavering support, insightful discussions and for enduring countless monologues.

Fredrik Engelschiøn Akre
Barcelona, Spain
June, 2023

Abstract

This thesis is concerned with the spectral properties of quantum particles in fractal potentials. Fractals are infinitely detailed systems that typically have non-integer dimensions. The study of these systems is motivated both by natural occurrences and possible experimental realizations of such potentials. Several spectral properties were considered for a total of thirty-three fractal potentials. Most properties displayed unique physics due to the fractal character of the systems, but not all.

This thesis starts by providing a discussion on methodology and the combination of concepts from measure theory and quantum mechanics. A highly efficient method of generating fractals was developed and named the Method of Repeated Kronecker Products. In this method, the fundamental properties of the generated fractal become evident through what is referred to as the "generator" of the fractal. A method for reducing the complexity of the Hamiltonian was also implemented leading to significant improvements in performance.

The first property studied was the scaling of the ground state energies as the details of the fractals were gradually increased. It was found that the scaling behaved as expected for a normal Euclidean object. That is, there were no observed consequences arising from the fractal nature of the systems in these results.

Next, the conductances through the fractals were evaluated. The contribution to the total conductance from the state at a given energy was considered. The conductances fluctuated rapidly when the energy was varied, and the conductances were found to be multifractal. The conductances had dimensions (capacity dimensions) equal to the fractal dimensions of the underlying potentials. These results show a clear manifestation of the fractal nature in the physically observable quantities. Furthermore, this property predicts that meaningful information can be determined for an unknown fractal structure by a conductance experiment.

To better understand the observed conductance results, the localization of states was considered. This was evaluated using the participation ratios of eigenstates in the fractal potentials. The results fluctuated rapidly as a function of the eigenenergy, and it was found that the participation ratios were also fractal with dimensions equal to the fractal dimensions of the underlying potentials. This means that for a given extended state in a fractal, there exists no neighborhood of stability in energy where the state is guaranteed to remain extended. These fluctuations between extended and localized states are thought to be the cause of the observed fluctuations in the conductances.

Finally, the level spacing statistics were studied. It was found that the energy level spacings of fractals with low internal connectivity followed decreasing power-law distributions for small energy spacings. This means that the likelihood of finding closely spaced eigenvalues is larger than one would expect in an open system. This might be understood as an effective energy level *contraction*. The result does not correspond to a periodic, aperiodic or quasiperiodic system and seems not to have a satisfactory explanation from random matrix theory.

Sammendrag

Denne avhandlingen omhandler egenskaper til kvantepartikler i fraktale potensialer. Fraktaler er uendelig detaljerte systemer, som oftest med en dimensjon som er et desimaltall. Motivasjonen bak å studere slike systemer kommer både fra naturlige forekomster av slike systemer og mulige eksperimentelle realiseringer. Flere egenskaper ble vurdert for totalt trettitre fraktaler. De fleste egenskapene ga unike resultater for fraktalene, men ikke alle.

Denne avhandlingen starter med en diskusjon om metodikk samt kombinasjonen av konsepter fra målteori og kvantemekanikk. En svært effektiv metode for å generere fraktaler ble utviklet og navngitt Kroneckerproduktmetoden. I denne metoden blir de grunnleggende egenskapene til den genererte fraktalen synlige gjennom det som blir kalt "generatoren" til fraktalen. En metode for å redusere kompleksiteten til Hamilton-matrisen ble også implementert, noe som førte til betydelige forbedringer i ytelse.

Den første egenskapen som ble studert var skaleringen av grunntilstandsenergiene etter hvert som detaljene i fraktalene økte. Skaleringen oppførte seg som forventet for et normalt euklidsk objekt. Det var dermed ingen observerte konsekvenser som følge av den fraktale naturen til systemene i disse resultatene.

Deretter ble ledningsevnene gjennom fraktalene vurdert. Bidraget til den totale ledningsevnen fra tilstanden med en gitt energi ble regnet ut. Ledningsevnene svingte raskt da energien ble variert, og det bel vist at ledningsevnene var multifraktale. Ledningsevnene hadde dimensjoner (Minkowski–Bouligand dimensjoner) lik fraktaldimensjonene til de underliggende potensialene. Resultatene viser tydelig at de fraktale egenskapene til potensialene fører til konsekvenser i de fysiske observerbare størrelsene. Videre så tilsier funnene at man kan hente ut informasjon fra en ukjent fraktalstruktur ved en måling av ledningsevnen.

For å forstå den observerte effekten bedre, ble lokaliseringen av egentilstandene studert. Dette ble gjort ved å regne ut deltakelsesgraden av tilstander i de fraktale potensialene. Resultatene svingte raskt som funksjon av egenenergiene, og det ble vist at deltakelsesgradene også var fraktale med dimensjoner lik fraktaldimensjonene til de underliggende potensialene. Resultatene viser at for en gitt utstrakt tilstand, så finnes det ikke et omegn i energi der tilstanden garanteres å forbli utstrakt. Disse svingningene mellom utstrakte og lokaliserte tilstander sees på som årsaken til de observerte svingningene i ledningsevnene.

Til slutt ble energinivåstatistikken studert. Det ble vist at energinivåforkjellene til fraktaler med lav grad av sammenkobling fulgte en avtagende potensfordeling for små energinivåforskjeller. Dette betyr at det er større sannsynlighet for å finne energier nærme hverandre enn det man ville forventet i et åpent system. Dette kan muligens forståes som en effektiv sammentrekning av energinivåene. Resultatet avviker fra periodiske, aperiodiske og kvasiperiodiske systemer, og har tilsynelatende ikke tilstrekkelig forklaring fra teorien om tilfeldige matriser.

Table of Contents

1 Introduction **1**

1.1 A historical introduction to fractals 1

1.2 The physics of fractals 2

1.3 Overview 4

2 Underlying theory on fractals **5**

2.1 Measure theory 5

2.2 Characterization of fractals 7

2.3 Quantitative analysis of fractal objects 11

2.4 Lindenmayer systems 15

3 Underlying theory on computational quantum mechanics **16**

3.1 Computational methods 17

3.2 Error evaluation methods 18

3.3 Quantum theory 19

3.4 Matrix formulation of quantum operators 20

3.5 Quantum transport theory 20

3.6 Level spacing statistics and random matrix theory 25

4 Studied fractals **27**

4.1 Fractal iteration and the linear length scale resolution 28

4.2 The Method of Repeated Kronecker Products 28

4.3 Sierpinski Carpet 29

4.4 Filled Sierpinski Square 31

4.5 Filled Sierpinski Curve 32

4.6 Sierpinski Gasket 33

4.7 Flag-fractal 35

4.8 Connectivity and ramification number 36

5 Implementation and methods of calculations **37**

5.1 Expressing the eigenvalue problem 37

5.2 Equivalence of enumeration 38

5.3 A reduced method for representation of the eigenvalue problem 40

5.4 Scaling of the ground state energy for increasing fractal iteration . . . 41

5.5 Current and conductance 42

5.6 Level spacing statistics 45

6 Scaling of the ground state energy for increasing fractal iteration **47**

6.1 Ground state of the Sierpinski Carpet 48

6.2 Scaling of the ground state energy of other fractals 52

6.3 Interpretation of the ground state energy scaling 56

7 Conductance **57**

7.1 Conductance through the Sierpinski Carpet 57

7.2 Conductance through the Sierpinski Gasket 61

7.3 Conductance through other fractals 64

7.4 Significance of connectiviy 66

7.5 Multifractal analysis of the conductances 67

7.6 Experimental realization 68

8 Participation ratio **69**

8.1 Participation ratio 70

8.2 Participation ratios of the fractals 70

8.3 Interpretation of results and relation to conductance 72

8.4 Periodicity of fractals 73

9 Level spacing statistics **74**

9.1 Level spacing statistics of the fractals 74

9.2 Level spacing distribution and connectivity 76

9.3 A comment on terminology 77

10 Closing remarks **77**

10.1 Summary and conclusion 78

10.2 Outlook 80

Appendix **83**

A Numerical performance **83**

A.1 Choice of algorithms 83

A.2 Performance of the reduced method 84

B Additional fractals **88**

Bibliography **99**

1 Introduction

This thesis is dedicated to the study of the spectral properties of quantum particles in fractal potentials. The aim is to study correlations between the properties of the fractals and the spectral properties of the confined particles. For this purpose, thirty-three different fractals were studied. The inherent complexity of fractals makes their study challenging, necessitating a partly theoretical approach informed by measure theory. Furthermore, due to the intensive numerical computations involved, computational efficiency plays an important role in this thesis. The analysis is carried out in the context of low-energy quantum mechanics but is likely to have applications in other fields as well.

1.1 A historical introduction to fractals

The term *fractal* was introduced relatively recently, in the 1980s, although the core concepts have a longer history. Fractals are non-differentiable structures that can be continuous and simply connected. This characteristic is one of the reasons why the definition emerged only recently, as it required a revision in the understanding of functions and sets.

Prior to the late 19th century, mathematicians were primarily concerned with the countable, and the concept of "infinite" was more closely linked to philosophy than to empirical science. However, an understanding of such functions and sets is a prerequisite for the study of fractals. The existence of continuous, non-differentiable functions was first demonstrated by K. T. W. Weierstrass in 1872 [Weierstrass (2013) or Hardt (1916)]. Around the same time, George Cantor rigorously investigated the infinite set in his 1874 paper [Johnson (1972)]. The example he provided of an uncountable set with zero measure is now known as the Cantor set [Cantor (1883)].

During the mid-20th century, objects with non-integer dimensions began to gain recognition in various branches of physics, often in connection with dynamics. One of the most influential papers, titled *Deterministic Nonperiodic Flow*, was authored by E. N. Lorenz in 1963 [Lorenz (1963)]. Lorenz demonstrated that a basic three-dimensional system, created to simulate weather, exhibited chaotic behavior on an attractor with a non-integer dimension[1]. Similar objects also emerged in quantum physics, such as electrons confined in crystals exposed to a magnetic field [Hofstadter (1976)].

The word *fractal* was introduced by B. B. Mandelbrot, known for his 1982 book *The Fractal Geometry of Nature*. Mandelbrot argued that numerous natural patterns, including coastlines, leaves, and lightning, were not merely more complex than traditional geometry, but represented an entirely different level of complexity [Mandelbrot (1982)]. Lorenz's findings, which showed that a low-dimensional system could exhibit such complexity, strongly supported this claim. These behaviors could not be modeled using conventional geometric considerations in higher dimensions. Instead, the behavior represented a new form of complexity altogether.

[1] Lorenz referred to this fractal object as a "strange attractor".

In some respects, the research of fractals can be viewed as a rebellion against conventional calculus, whose central assumption is that objects appear smooth when viewed at a sufficiently small scale. Mandelbrot pointed out that many natural patterns, such as turbulent flows, ocean waves, and the shapes of leaves, coastlines, and clouds, do not display this smoothness.

Fractals are frequently associated with self-similar objects, meaning they consist of infinitely repeating versions of themselves. While these patterns are easier to generate and analyze, the definition of a fractal does not impose such a requirement. The focus on self-similarity is an attempt to maintain a sense of regularity in the chaotic realm of fractals. This thesis will consider self-similar fractals for practical reasons, hoping they depict some of the properties of more general fractals.

1.2 The physics of fractals

The following includes a discussion on the emergence of fractals in physics and a brief introduction to the systems that will be considered in this thesis. Fractals have been observed in numerous areas of physics and many modern technologies have started to take advantage of these structures. The technological applications include fractal antennas, used to pick up a spectrum of wavelengths [Azeez, Jabbar and Wang (2016)]. Fractal surfaces are employed in the design of solar panels [Roe et al. (2020)] and acoustic diffusers [Priyadarshinee, Lim and Lee (2018)] to increase surface area. Fractals are also used in heat exchangers [Zhiwei et al. (2016)], in micro-scale capacitors [Samavati et al. (1998)] and more.

Fractal structures frequently result from the time evolution of a quantity or bifurcation in a dynamical system [Strogatz (2015), Chapter 12]. Fractals in dynamical systems are therefore extensively examined in the field of chaos theory. Examples of such fractals include those found in weather systems, chemical chaos, mechanically forced double-well oscillations, and others. A particularly notable example is the bifurcation diagram of the logistic map [Strogatz (2015)].

Quantum effects become important when applying fractals in for example solar panels and micro-scale capacitors. One of the earliest emergences of a fractal within quantum mechanics involved the spectral properties of a single electron confined in a crystal subjected to a magnetic field [Hofstadter (1976)]. The resulting graph of the band structure plotted against the flux forms a fractal pattern known as the Hofstadter butterfly, as illustrated in Figure 1. The Hofstadter butterfly appears in many physical systems, including solid-state physics [Dean et al. (2013)], optics [Ni et al. (2019)], and ultra-cold atoms [Aidelsburger et al. (2013)].

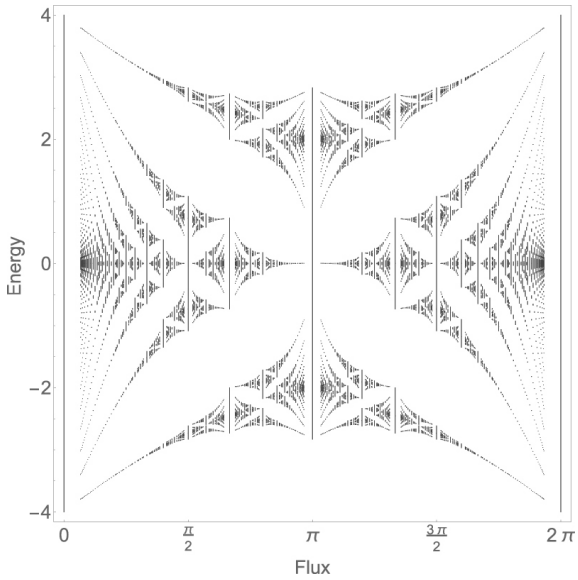


Figure 1: The band structure plotted against the flux $2\pi\alpha$ for non-interacting electrons in a two-dimensional periodic potential, such as a lattice of atoms. The resulting energy level diagram is a fractal known as the Hofstadter butterfly.

Source: Hatsuda, Katsura and Tachikawa (2016).

Physics within such fractal structures exhibits several unique properties. Diffusion in periodic fractals deviates from classical transport laws as seen for other periodic systems [Havlin and Ben-Avraham (1987)], and the spectrum of fractals can be defined on a Cantor set. Furthermore, it has been demonstrated that the conductance through certain fractal structures might be inherently linked to the non-integer dimension of the object [van Veen et al. (2016)]. Even so, there is still much that remains unknown about the properties of quantum particles in such systems.

One of the reasons why physics in fractals is not better understood is that the study of these systems can be challenging. First of all, it is difficult to characterize fractals and even define what they are. Furthermore, analytical methods often fail for fractals due to irregular surfaces. Even in numerical methods, the infinite detail of the systems complicates the discretization and frequently leads to a demand for high-resolution computations that are numerically intensive. Moreover, as mentioned earlier, there is often an inherent connection between fractal structures and a system's dynamics, which exacerbates the computational evaluations.

Due to the above reasons, this thesis will be concerned with the properties of a single quantum particle within highly self-similar, static fractal potentials. Although this is still computationally intensive, it allows for relatively high-precision calculations. Furthermore, studying quantum effects in fractals has become increasingly relevant due to technological applications such as the aforementioned solar panels and microscale capacitors. Finally, the choice is also motivated by the emerging possibility of creating precise fractal structures down to the atomic level in laboratories. This has been demonstrated by Kempkes et al. (2019) in their remarkable paper on "Design and characterization of electrons in a fractal geometry", see Figure 2.

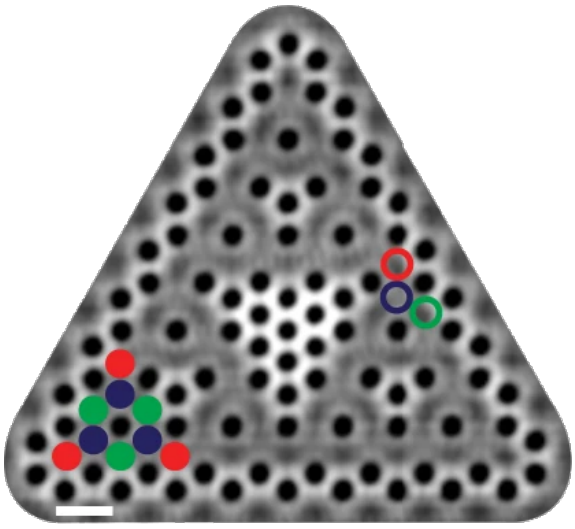


Figure 2: STM image of a physically realized Sierpinski Gasket, made up of carbon monoxide. The indicated white scale bar is 2 nm. A colored version of the first generation of the gasket is overlayed to assist visualization.

Source: Kempkes et al. (2019).

The objective of this thesis is to study the spectral properties of an ensemble of static fractal potentials in the hope that the results convey general properties. Specifically, the study will be carried out for the ground state energy of fractals at infinite resolution, transport properties, the localization of states and level spacing statistics.

1.3 Overview

The thesis is structured as follows. The underlying theory which is relevant to the thesis is presented in Sections 2 and 3. Section 2 discusses the characterization of fractals, including measures of fractal dimensionality together with methods of evaluating these. The section also introduces relevant concepts from measure theory, but in-depth knowledge of these concepts is not necessary to follow the content of this thesis. The discussion on underlying theory continues in Section 3. Here, an introduction is given to computational methods and quantum mechanics. This includes quantum transport theory as well as level spacing statistics and random matrix theory. These discussions are preliminary to the methodology discussed later.

Sections 4 and 5 describe the core methodology used to evaluate different properties of the fractals. In Section 4, the generation of the fractals is discussed along with additional measures to characterize them. Properties of the fractals such as the fractal iteration, connectivity and the minimal grid representations of the fractals are covered. A custom method of generating the fractals using repeated Kronecker products is presented. Section 5 deals with the evaluation of different spectral properties. First, the discretization of the eigenvalue problem is discussed together with a method of dramatically reducing the size of the Hamiltonian for the considered fractal systems. Next, the means of studying the scaling of the ground state energy when approaching infinite fractal detail is considered. The numerical evaluation of

conductance through a system is treated subsequently. Finally, details of evaluating the level spacing statistics of a system are given. This provides the tools for evaluating the spectral properties of the fractals.

Results for the studied spectral properties together with discussions of these are found in Sections 6−9. In Section 6, the results for the scaling of the ground state energy when approaching infinite fractal detail are presented. The application of the methodology is first demonstrated in detail for a particular fractal, namely the Sierpinski Carpet, before being applied to the other fractals. Finally, an interpretation of the obtained results is included. The properties of conductance through a fractal are discussed in Section 7. The calculation and interpretation of the results are carried out in detail for two fractals; the Sierpinski Carpet and the Sierpinski Gasket. Subsequently, the evaluation is done for the other fractals. Extra discussions on the connectivity of the fractals, multifractal structures and a possible experimental realization are included at the end of the section. Section 8 presents a study of localized and extended eigenstates in fractals. This section serves as an extension of the discussion of the results found for the conductances in Section 7. It also motivates the study of the level spacing statistics of the fractals. Finally, the results from the level spacing statistics of the fractals are presented and discussed in Section 9.

Closing remarks are found in Section 10. Here, a summary of the results is presented together with a concluding discussion. The thesis ends with some reflections on the work carried out and an outlook discussing potential further research in the field.

2 Underlying theory on fractals

This section contains discussions on measure theory and the characterization of fractals. First, certain concepts from measure theory will be introduced briefly. These concepts are introduced as a foundation for the discussion on dimensionality and characterization of fractals in Section 2.2. However, a comprehensive understanding of these ideas is not required to follow the reasoning in Section 2.2. Section 2.3 further discusses the dimensional analysis of fractal objects. Finally, a mathematical framework for generating fractals known as the Lindenmayer systems is given in 2.4. This framework will be made use of but is not the one primarily employed in this thesis.

2.1 Measure theory

Measure theory is a branch of mathematical analysis that deals with the quantification of size and volume in a rigorous and generalized way. In the following, certain concepts from measure theory will be introduced. A full understanding of these concepts will not be necessary to follow the reasoning of other sections.

Metric space

The metric space is actually a concept from topology, which is a separate branch of mathematics from measure theory, although the two are interconnected. A metric space consists of a collection of elements, referred to as points, along with a notion of distance between any pair of points, known as a metric [Sutherland (2009)]. In mathematical terms, a metric space is represented by X and h, where X denotes the set of points and h represents the distance function. The metric h must fulfill the following set of properties:

- Non-negativity: $h(x, y) \geq 0$.
- Identity of indiscernibles: $h(x, y) = 0$ if and only if $x = y$.
- Symmetry: $h(x, y) = h(y, x)$.
- Triangle inequality: $h(x, y) + h(y, z) \geq h(x, z)$.

A metric serves as a generalization of the well-known concept of distance in Euclidean space.

σ-algebra

This discussion is heavily based on the treatment of σ-fields in Chapter 2 of *Probability and Measure 3rd ed.* by Billingsley (1995) [2]. In the field of measure theory, a σ-algebra is a particular type of algebra for a subset of a given set. It is the collection of subsets from a set X that remains closed under specific operations, such as taking the complement and creating countable unions and intersections. Formally, a σ-algebra Σ of a set X is a collection of subsets of X that meet the following criteria:

- Σ contains the empty set and X, i.e. $\{\}$ and $X \in \Sigma$
- Σ is closed under complementation, i.e. if $A \in \Sigma$, then its complement $A^C \in \Sigma$
- Σ is closed under countable unions: If $A_1, A_2, A_3, \ldots$ is a sequence of sets in Σ, then so is the union of the sequence $A = A_1 \cup A_2 \cup A_3 \cup \cdots \in \Sigma$.

Together, a σ-algebra and a metric space, $\{X, \Sigma\}$, is frequently referred to as a measurable space.

The power class $\mathcal{P}(X)$ is the largest σ-algebra [Billingsley (1995)]. The power class is the set of all subsets of a given set X. It includes the empty set and the original set itself.

[2] While Billingsley (1995) mainly addresses σ-fields, the closely related concept of σ-algebra is used here [Billingsley (1995)].

The Carathéodory construction

Constantin Carathéodory first introduced the Carathéodory theorem in 1913 in his book *Vorlesungen über reelle Funktionen* [Carathéodory (1913)]. The Carathéodory construction refers to a method for constructing an equivalent measure on a larger space based on a given measure in a smaller space [Tao (2011)]. Considering a set X and a subset $Y \subseteq X$, and a measure h on Y, the Carathéodory theorem guarantees the existence of a unique measure $\tilde{h}$ on the smallest σ-algebra containing Y, so that $\tilde{h}(A) = h(A)$ for all sets A in Y. The definition of a σ-algebra was provided earlier.

Formally, let X, Σ denote a measurable space as mentioned in the σ-algebra discussion. Let Y be a subset of X, and h a measure on the σ-algebra Σ_Y of Y. The objective is to identify a measure $\tilde{h}$ on the σ-algebra Σ_X of X, such that for all A in Σ_Y, $\tilde{h}(A) = h(A)$. Carathéodory's theorem claims that such a measure always exists and is unique.

The Carathéodory construction serves as a method for assigning a measure to a collection of subsets of a given set, based on the Carathéodory theorem. Let Y represent a collection of subsets of the metric space X and h be a measure $h : Y \to [0, \infty]$. Pick an arbitrary positive scalar value denoted by $\delta > 0$. Assume that one can find sets from our collection $\{S_i\} \in Y$ with diameters $diam(S_i)$ less than δ, that cover the entire metric space X. Note that this implies that the sets S_i are nonempty, as they cover the metric space X. Next, assume that for all $\delta > 0$, sets $S_i \in Y$ can be found with measure $h(S_i) < \delta$, while maintaing that their diameter $diam(S_i) < \delta$. In other words, these δ values can be made arbitrarily small. Now, define the Carathéodory construction for values of $\delta > 0$ and subsets of the metric space $A \subseteq X$ as follows:

$$\tilde{h}_\delta^{h,Y}(A) = inf\left\{\sum h(S_i) : A \subseteq \bigcup S_i, diam(S_i) < \delta, S_i \in Y\right\}. \tag{1}$$

Note that the second assumption implies that $\tilde{h}\delta^{h,Y}(\emptyset) = 0$. This can be observed by first noting that if A is the empty set, any collection of sets can cover A, particularly, any one set in the collection $\{S_i\}$ is sufficient. So there is no practical restriction of the set having to cover A. The measure becomes equivalent to the infimum of $h(S_i)$, for S_i whose diameter is smaller than zero. The second assumption says that one can pick δ arbitrarily small, so the infimum is then simply zero.

2.2 Characterization of fractals

Mandelbrot argues that dimensionality is a vague and imprecise notion [Mandelbrot (1982), Chapter *The Idea of Dimension*]. The original definition of a fractal encompasses various ideas of dimensionality as they are necessary to carry out a precise discussion of fractals. A discussion of dimensionality and the features of fractals is presented here. Preliminary concepts from measure theory can be found in Section 2.1. However, detailed knowledge of these concepts is not necessary to follow the discussion.

Lebesgue and Hausdorff dimensions

The Lebesgue covering dimension D_L was first formulated using a brick wall analogy [Mandelbrot (1982)]. When covering a two-dimensional Euclidean square with bricks of arbitrarily small size, Lebesgue demonstrated that each brick must touch at least three other bricks. In the same way, Lebesgue proved that when covering a D_L-dimensional cube, each brick, or open set, would need to be in contact with at least $D_L + 1$ other open sets. This results in an integer measure of dimensionality that remains constant under continuous deformation of space [Edgar (2008)]. In other words, it is invariant under homeomorphism. This concept of dimensionality will also be referred to as the topological dimension.

Next, consider the Hausdorff dimension, represented by D_H. Given a metric space X as defined in Section 2.1, let $\mathcal{P}(X) := S : S \subseteq X$ be the set of all subsets of X, where each subset is denoted S. Introduce a measure $h_q(S) = (diam(S))^q$, where q is a positive and real number and $diam$ denotes the diameter. Additionally, let $\delta \in \langle 0, \infty]$ be a number that will soon be forced to zero. Consider the Carathéodory construction $\tilde{h}_\delta^{h_q,Y}(A)$, as outlined in Section 2.1. If this is unfamiliar, it is not crucial; the physical relevance in the current context will be explained shortly. The Carathéodory construction's parameters include the bounding value δ, the quantity to be measured h_q, and a set $\mathcal{F}$. A set A is taken as the variable. Applying the Carathéodory construction from (1) to this system results in

$$\begin{aligned} \mathcal{H}_\delta^q(A) \equiv \tilde{h}_\delta^{h_q,\mathcal{P}(X)}(A) &= inf\left\{\sum h_q(S_i) : A \subseteq \bigcup S_i, diam(S_i) < \delta, S_i \in \mathcal{P}\right\} \\ &= inf\left\{\sum (diam(S_i))^q : A \subseteq \bigcup S_i, diam(S_i) < \delta\right\}, \end{aligned} \tag{2}$$

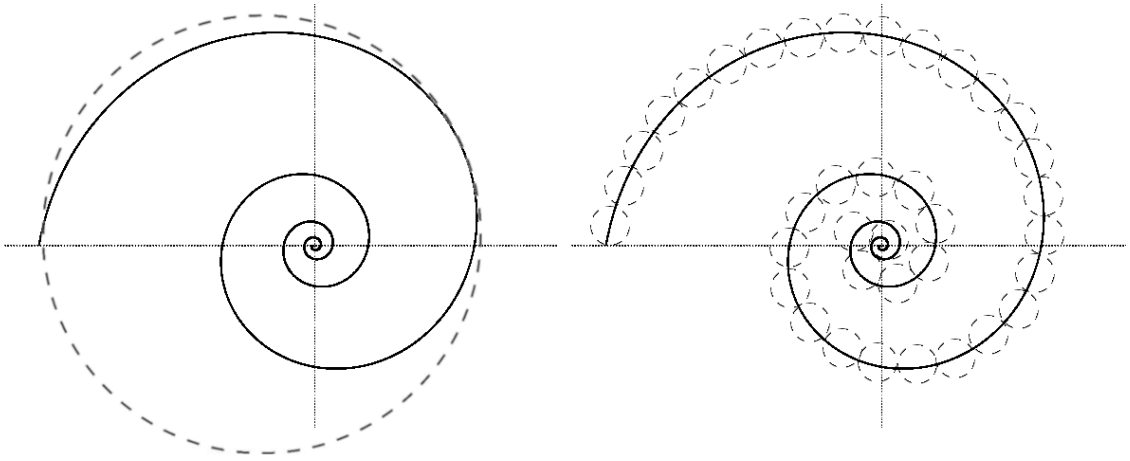
where $\mathcal{P}(X)$ is the power class as given in Section 2.1.

Consider the physical interpretation of the measure in 2, that is, consider what $\mathcal{H}_\delta^q(A)$ measures. Given a smooth, well-behaved curve in $\mathbb{R}^2$, imagine covering the object with small rings. One can choose the size of the rings freely, with the only constraint that their diameter must be less than δ. For higher dimensions, the rings are replaced by spheres. Next, compute the sum of the diameters of all these rings covering the object. For $q = 1$, $\mathcal{H}_\delta^1(A)$ in 2 gives the minimal possible value of this sum of diameters. The input set A is the spiraling curve. This is illustrated in Figure 3a and Figure 3b. The figures also demonstrate the purpose of the confining parameter δ. When δ is very large, the set of rings with the smallest total diameter which covers the curve is, in this case, simply one large circle, as shown in Figure 3a. However, this captures the shape of the object very poorly. By reducing δ, the rings are forced to fit the curve more accurately, as shown in Figure 3b. On the other hand, changing q means taking the sum of the diameters to the power q and minimizing this sum instead. Letting δ approach zero in the case of $q = 1$, one would then get the length of the curve A. This is the next step, letting δ tend to zero for an arbitrary q, one obtains the Hausdorff measure, given by

$$\mathcal{H}^q(A) = \lim_{\delta \to 0} \mathcal{H}_\delta^q(A) = sup_\delta \left\{\delta > 0 : \mathcal{H}_\delta^q(A)\right\}, \tag{3}$$

where the last equality appears since $\mathcal{H}_\delta^q(A)$ is strictly increasing as δ goes to zero. This is because decreasing δ only further limits the choices of rings one can choose

when minimizing the aforementioned sum. Finally, from this measure, the Hausdorff



(a) (b)

Figure 3: The Hausdorff measure of a spiraling curve for different values of δ. The combination of circles that completely cover the object and has the smallest sum of diagonals is chosen. This is done with the restriction that the individual circles have diameters less than δ. The actual measure is obtained when letting $\delta \to 0$. (a) When δ is large the combination of circles with minimum total diameter is trivially one large circle. (b) For smaller δ the circles start to follow the shape of the curve more closely.

dimension can be defined. In the case of the smooth curve, notice that when setting $q < 1$ one obtains an infinite Hausdorff measure from 3. On the other hand, setting $q > 1$ gives zero Hausdorff measure, while setting $q = 1$ one obtains a finite Hausdorff measure. For a square, this transition occurs at $q = 2$. That is, the square has an infinite length ($q = 1$), finite area ($q = 2$), and zero volume ($q = 3$). The positive and real number q can also take on non-integer values. For a general object, the Hausdorff dimension is defined by the q-value that marks this transition. For $q < D_H$ the Hausdorff measure in 3 is infinite, for $q = D_H$ the measure is finite, and for $q > D_H$ the measure is zero. That is,

$$D_H(A) = inf\left\{q \geq 0 : \mathcal{H}^q(A) = 0\right\} = sup\left\{q \geq 0 : \mathcal{H}^q(A) > 0\right\}. \tag{4}$$

Hausdorff dimension quantifies how much the measure of an object changes when you rescale it.

The definition of a fractal

With the Lebesgue and Hausdorff dimensions defined, it is straightforward to reproduce the original definition of a fractal. However, this is not a unique or problem-free definition.

First, observe that for smooth geometric shapes, $D_L = D_H$. However, while D_L must take integer values for all shapes, D_H is not restricted to integers. In general, the dimensional measures comply with

$$D_H \geq D_L,$$

as stated in Edgar (2008) theorem 6.3.10. Mandelbrot's original definition of a fractal is any set where

$$D_H > D_L, \tag{5}$$

Mandelbrot (1982), Chapter *Definition of the Term Fractal*. It is important to note that a fractal can have integer dimensionality, and its definition does not require self-similarity.

Before continuing, it is worth mentioning that although (5) is the first definition of a fractal, this definition has faced criticism from many, including Mandelbrot himself. The definition excludes traditional, smooth geometric objects but does not encompass all objects that one might intuitively consider fractals. The definition appears to be sufficient but not necessary. For more information on this topic, see Chapter *Fractals (on the Definition of)* in Mandelbrot (1982).

Similarity dimension

The formal definition of the Hausdorff dimension is often difficult to apply. However, the more intuitive similarity dimension D_S is sometimes a suitable alternative. Self-similar objects are composed of multiple copies of themselves, scaled down by a factor of $1/r$. For instance, a Euclidean box with side lengths of 1 consists of four smaller boxes with side lengths of $1/2$. Of course, it also consists of nine smaller boxes with side lengths of $1/3$. This concept is illustrated in Figure 4, from Strogatz (2015). After rescaling each side by a factor $1/r$, let the number of new copies obtained be denoted by m. The factor r will be referred to as the linear rescaling factor, and m as the number of copies. Clearly, rescaling the box by a factor of $1/r$ results in $m = r^2$ new boxes. For a line, it yields $m = r^1$ new lines, and for a cube, it produces $m = r^3$ new cubes. In general, a D-dimensional self-similar object rescaled by a factor of $1/r$ can be said to create $m = r^{D_S}$ new copies of itself. This measure of dimensionality, called the similarity dimension D_S, does however not have to be an integer [Strogatz (2015)]. It can be calculated by

$$D_S = \log_r(m) = \frac{\log(m)}{\log(r)} \tag{6}$$

where r is the linear rescaling factor and m is the number of self-similar copies.

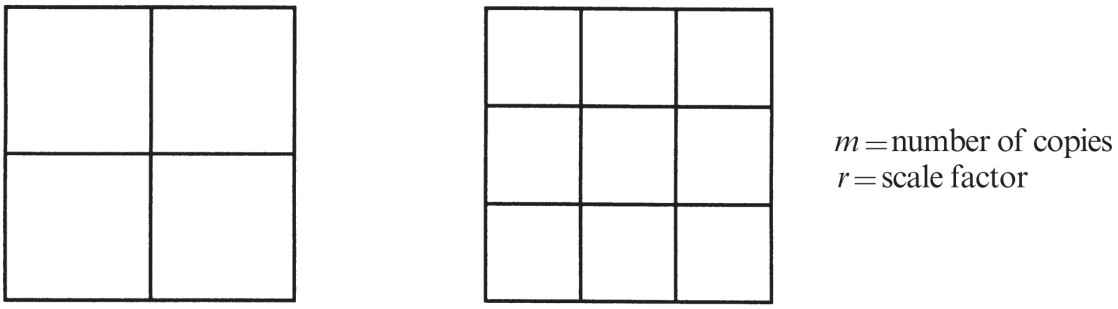


Figure 4: The classical box is a perfectly self-similar object. It can be said to consist of copies of itself scaled down to infinitely small sizes. Rescaling it by a factor $1/r$ produces $m = r^2$ copies.

Source: Strogatz (2015).

To understand the application of the similarity dimension, we must first define the open set condition. The set of self-similar objects $S_0, \ldots S_N$ that make up, for example, a fractal, satisfies the open set condition if and only if a non-empty open set O exists such that $S_i(O)$ are pairwise disjoint and contained within O [Hutchinson (1981)]. Explicitly written,

$$\begin{aligned} &S_i(O) \subset O \ \ \forall\, i \in [0, N]\,, \ \text{ and} \\ &S_i(O) \cap S_i(O) = \emptyset \ \text{ if } \ i = j. \end{aligned} \tag{7}$$

In other words, the open set condition can be described as necessitating that the object is perfectly self-similar, meaning that the object is entirely covered by replicas of itself without any overlap. Moreover, if a self-similar set satisfies the open set condition, then the Hausdorff dimension D_H is equal to the similarity dimension D_S [Hutchinson (1981)]. For perfectly self-similar fractals, this offers a convenient method for calculating the Hausdorff dimension.

2.3 Quantitative analysis of fractal objects

Analytical evaluation of the dimensionality of an object is not always possible or practical. In these cases, a variety of methods and measures can be applied. In the following, one such method called the box-counting analysis will be treated. Following this, a discussion on multifractals and a measure for this is included.

Box-counting analysis

The box-counting analysis provides a method for numerically estimating the fractal dimension of an object when the similarity dimension is unavailable or the open set condition is not satisfied. The obtained estimate for the dimension is called the box-counting dimension or Minkowski–Bouligand dimension and will be denoted D_{BC}.

In the analysis, one divides an object into boxes of a certain size and counts the number of boxes that are needed to cover the object [Falconer (2003), Chapter 2]. Next, the box size is varied and the new corresponding number of covering boxes is counted. The relationship between the size of the boxes and the number of boxes needed provides an estimate of the dimension of the object.

Let $h(\epsilon)$ be the number of boxes of size ϵ needed to cover the object. For an infinitely detailed system, the box-counting dimension is then given by

$$D_{BC} = -\lim_{\epsilon \to 0} \frac{\log(h(\epsilon))}{\log(\epsilon)}. \tag{8}$$

This is the case for an infinitely detailed system. However, in numerical calculations, one typically has objects represented by a finite collection of discrete points, and therefore does not want to evaluate the dimension at $\epsilon \to 0$ as this would yield imprecisions due to the finite sampling of the object.

In a discrete system, three regions are expected to appear as shown in Figure 5. Note that Figure 5 is a log-log plot and that the leftmost part of the figure corresponds to large boxes, and they become gradually smaller towards the right. When the boxes are very large, farthest to the left in Figure 5, the entire object will be covered by a single box, that is $h(\epsilon) = 1$ and $\log(h) = 0$. If the box size is gradually reduced then two boxes will eventually be needed, but the two will at first overcover the object. As one then slightly reduces the box size further, two boxes will still be sufficient and the number of boxes won't change. This leads to the plateaus seen to the left in Figure 5. Furthermore, in this region, every box present is highly likely to be occupied. Due to this, the box-counting method is expected to always yield the topological dimension of the object, even if the object has a smaller fractal dimension. This is simply because when the boxes are large enough, they will all be filled, and the details of the system are not recovered. The fractals studied here have a topological dimension of 2, and it is therefore expected that the box-counting analysis gives a slope equal to 2 in the left-most region.

On the other hand, if the boxes become too small, the resolution of the object that is being sampled will start affecting the results. At some point, each box has either 1 or 0 discrete points inside it. Reducing ϵ and thereby adding more boxes will thus not increase $h(\epsilon)$. This leads to the asymptotic tail of slope equal to 0 to the right in Figure 5. This only occurs in a discrete system, and shows why one does not want to consider (8) for too small ϵ in such systems.

In between these two regions, a scaling region is found, where the number of boxes needed to cover the object goes as $h(\epsilon) \propto \epsilon^{-D_{BC}}$, where it is expected that $D_{BC} = D_H$. The power law scaling is seen as a straight line in the log-log graph in Figure 5. For a finite system, one measures this slope inside the scaling region to get an estimate of the box-counting dimension of the system D_{BC}. The object must be represented by a sufficiently large amount of points in order to get accurate results from the box-counting method. The box-counting dimension is equal to 1 for a regular one-dimensional line and 2 for a two-dimensional system when sampled to sufficient precision.

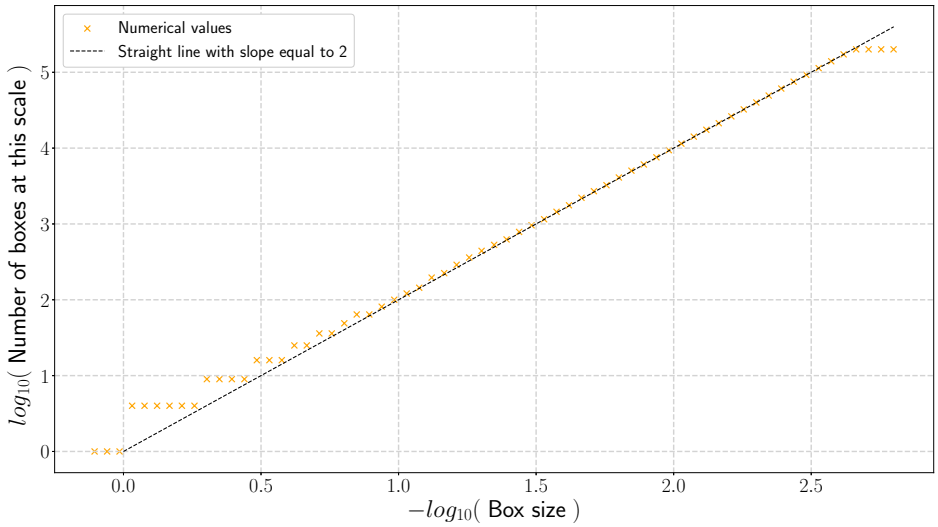


Figure 5: Box-counting analysis performed on a regular two-dimensional box. The procedure yields the expected dimension $D_{BC} = 2$.

It is worth noting that it is sometimes not trivial to determine the scaling region [Jiang and Liu (2012)]. As mentioned above, the plot is expected to have a slope equal to 2 (the topological dimension) for large boxes, and 0 for very small boxes. Distinguishing true scaling from edge effects can be challenging, and this presents a limitation for the box-counting analysis.

Multifractal analysis

In some cases, a system is characterized by more than one fractal dimension. While simple fractals are typically self-similar at all scales, multifractals are characterized by having a more complex internal structure, showing different scaling behavior at different locations or for different moments [Falconer (2003), and Budroni, Baronchelli and Pastor-Satorras (2017)]. Different measures of multifractals can be defined, see Falconer (2003), Chapter 17. This discussion will be concerned with the generalized dimensions or Renyi dimensions, $D(q)$, as discussed by Budroni, Baronchelli and Pastor-Satorras (2017). The theory behind this measure was first introduced by Rényi (1961) in his article *On Measures of Entropy and Information.*

The core idea behind the generalized dimension is to study the scaling behavior of different statistical moments in the fractal. The definition of the generalized dimension reads

$$D(q) = \frac{1}{q-1} \lim_{\epsilon \to 0} \frac{\log(h_q(\epsilon))}{\log(\epsilon)}, \tag{9}$$

Budroni, Baronchelli and Pastor-Satorras (2017). The measure $h_q(\epsilon)$ will be explained in the following. Equation (9) bears similarity to (8), and the method can be thought of as a generalization of the box-counting analysis. The studied object is again covered by boxes of a given size. This time, however, a measure is evaluated

for each box. The measure can for example be the number of data points that fall into the box[3]. This yields a matrix, or a heatmap, where each element represents the measure evaluated for a particular box. The heat map is normalized to have a total sum of elements equal to 1, and the elements are then raised to a power q. After this, the elements are summed. Call this sum $h_q(\epsilon)$, where ϵ refers to the box size used. The procedure is repeated for several box sizes. A scaling analysis is carried out equivalent to the one depicted for the box-counting analysis in Figure 5, comparing the value of $h_q(\epsilon)$ to the size of the boxes used ϵ while keeping q fixed. The scaling follows a power law with an exponent τ. Once again, by using a log-log plot, the value of τ is easily measured as the slope of the obtained straight line. This procedure is then repeated for different exponents q. For varying ϵ and q, one then has the scaling

$$h_q(\epsilon) \propto \epsilon^{-\tau(q)}, \tag{10}$$

where the function $\tau(q)$ gives the slope of the scaling when changing box sizes for a certain exponent q. Next, notice that

$$h_q(\epsilon) \propto \epsilon^{-(q-1)D(q)}. \tag{11}$$

Combining (10) and (11) yields a method for numerically estimating $D(q)$, writing

$$D(q) = \frac{1}{q-1}\tau(q). \tag{12}$$

In this analysis, one recovers the regular box-counting dimension in the case of $q = 0$.

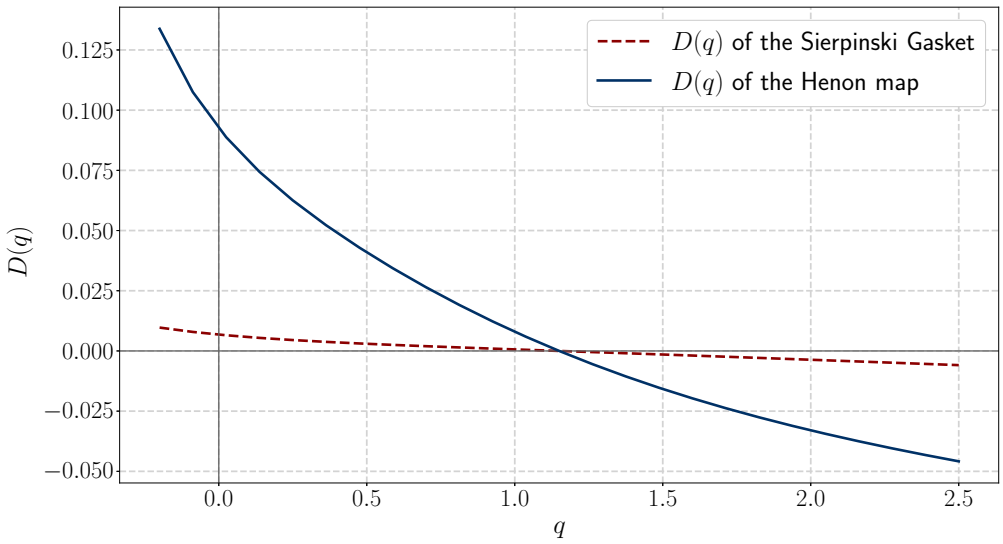


Figure 6: The generalized dimension $D(q)$ is plotted against moments q between -0.2 and 2.5 for the Sierpinski Gasket and the Henon map. The results are vertically adjusted to cross the horizontal axis at the center of the plot. For monofractals, the generalized dimension has a weak dependence on q, exemplified here using the Sierpinski Gasket. For multifractals, on the other hand, the generalized dimension depends strongly on the moments q, as is demonstrated by the Henon map.

[3]The partition function is a usual choice of measure. For a continuous system, the length of the curve within the box can be used.

A non-fractal, Euclidean object is expected to have a constant generalized dimension $D(q) = D$. The generalized dimension of a simple fractal characterized by a single fractal dimension is expected to be almost constant. However, a slow decrease in $D(q)$ as the exponent q increases is expected. Such structures are called monofractals. On the other hand, the generalized dimension of a multifractal has a much stronger dependence on q, decreasing much faster. The results of a multifractal analysis are demonstrated for a monofractal named the Sierpinski Gasket and a multifractal named the Henon map in Figure 6. The Sierpinski Gasket will be discussed in greater detail in later sections. In the figure, the generalized dimensions $D(q)$ of both systems are adjusted vertically to intersect the horizontal axis at the center of the plot. This is done to help illustrate the difference between the variation in $D(q)$ in the two cases. Clearly, the generalized dimension varies strongly in the case of the multifractal Henon map as compared to the monofractal Sierpinski Gasket.

When the value of the exponent q is large, the dense regions of the fractals will dominate. This is because the measure $h_q(\epsilon)$ becomes very large in these regions for large exponents. This means that the values of $D(q)$ to the right in Figure 6 reflect the dimension and scaling properties of the densest regions of the object. On the other hand, setting q small, and particularly $q < 0$, would make the dilute regions more dominant.

Finally, in the context of multifractal analysis, $D(q = 0)$ is referred to as the capacity dimension and is equal to the box-counting dimension. Furthermore, $D(q = 1)$ is the information dimension and $D(q = 2)$ is the correlation dimension.

2.4 Lindenmayer systems

A Lindenmayer system, or L-system, is a mathematical framework made by A. Lindenmayer in 1962 to model biological systems [Lindenmayer (1968)]. It is an iterative procedure and was first applied to generate the shapes of plants, but it is useful for other self-similar systems as well, including self-similar fractals. An L-system comprises a set of symbols, for instance, the symbols F, G. Additionally, a set of transformation rules are specified, like $F \to G$ and $G \to FG$. An axiom, or starting point, is established, and the rules are applied iteratively. With the axiom set to F, the initial few iterations of the described system would be

$$F \to G \to FG \to GFG \to FGGFG \to ...$$

Typically, F and G are interpreted as specific geometric shapes, such as straight lines with lengths L_F and L_G. The generated string, here $FGGFG$, then forms a set of construction. Starting from the right, one draws the given instructions. This results in a pattern that expands with each iteration, here it would simply be a growing straight line.

By convention, several standard symbols are normally used. Typically, $+$ and $-$ correspond to counterclockwise and clockwise rotations, respectively. Furthermore, [is understood as saving the current location and orientation when drawing shapes,

while] is interpreted as loading the last stored location and orientation. In this way, a string segment, or instruction segment, enclosed in brackets will not impact the next commands in the rest of the string.

Consider a more advanced example of an L-system. Set the axiom to F, and the angle applied by $+$ and $-$ to $22.5°$. Then, define the rules

$$F \to G[-F][F]G[-F] + GF,$$
$$G \to GG.$$

Starting with the axiom and applying the rules repeatedly produces a rapidly growing set of instructions. Now, interpret both F and G as straight lines of equal length. The obtained structure is shown in Figure 7. This example shows why this model is used to describe biological systems. The framework illustrates how the repeated application of simple rules can generate large-scale structures with intricate details and a high degree of self-similarity. L-systems can be utilized to generate fractals. This also gives insight into why biological structures from for example cell division or branching processes often appear fractal.

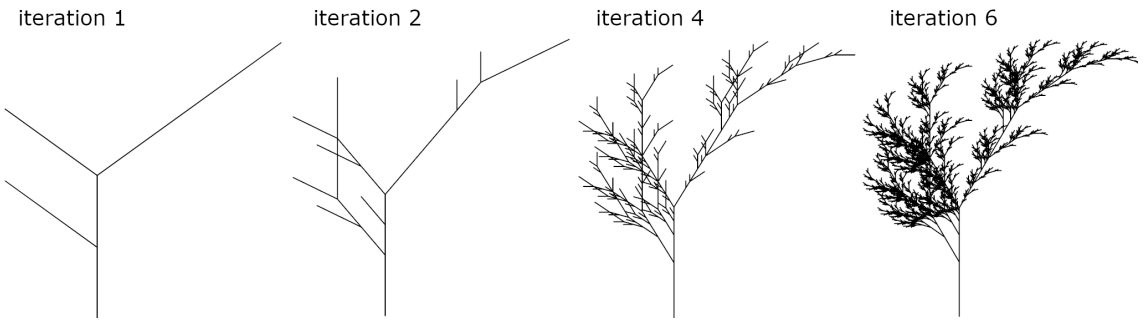


Figure 7: The first few iterations of the described Lindenmayer system. The system's application to the modeling of biological structures becomes evident as the iteration increases. In the described system, the G -values become branches that grow for each iteration. The F-values appear as leaves and indicate where the next branches should emerge.

3 Underlying theory on computational quantum mechanics

This section treats theory from computational quantum mechanics. It starts by introducing elementary means of discretizing and numerically evaluating systems. Next, basic concepts from quantum mechanics are reviewed in Sections 3.3 and 3.4. Following this, the scattering theory of transport is discussed. Finally, random matrix theory and level spacing statistics in quantum systems are considered in Section 3.6.

3.1 Computational methods

The primary focus of computational calculus involves evaluating derivatives and integrals [Sauer (2011)]. Numerical approximation of differentiation can be achieved using finite difference formulas. From the definition of a derivative one can obtain the two-point forward-difference formula, namely

$$\frac{df(x)}{dx} = \frac{f(x+d) - f(x)}{d} - \frac{d}{2}f''(c), \tag{13}$$

where d represents the stepsize, and c is a value between x and $x+d$. A very common approximation is the three-point compact stencil, which can be expressed as

$$\frac{df(x)}{dx} = \frac{f(x+d) - f(x-d)}{2d} - \frac{d^2}{6}f'''(c). \tag{14}$$

As the stepsize d tends to zero, the first term of both (13) and (14) converges to the exact derivative. However, the convergence is faster in the latter case, as can be seen from the error terms square dependence on stepsize d. For the second derivative, the same approach results in

$$\frac{d^2f(x)}{dx^2} = \frac{f(x-d) - 2f(x) + f(x+d)}{d^2} - \frac{d^2}{12}f^{(iv)}(c). \tag{15}$$

Retaining only the first term provides an approximation of the second derivative. When extended to two dimensions, the expression becomes

$$\begin{aligned}\Delta f(x,y) \approx & \frac{f(x-d_x,y) - 2f(x,y) + f(x+d_x,y)}{d_x^2} \\ & + \frac{f(x,y-d_y) - 2f(x,y) + f(x,y+d_y)}{d_y^2}.\end{aligned} \tag{16}$$

Discretize the system onto a grid $\mathbf{G}$ consisting of $N_x \times N_y$ uniformly spaced sites over the dimensions L_x and L_y. The discretization of coordinates x and y are represented by $\tilde{x}$ and $\tilde{y}$. For a one-dimensional derivative along the x-coordinate, the function $f(x)$ can be approximated by a vector $\tilde{f}(x) \equiv f(\tilde{x})$ with N_x elements. The Laplacian in equation (15) then becomes an $N_x \times N_x$ matrix and can be written as

$$\Delta_x \approx \frac{1}{d_x^2}\begin{bmatrix} -2 & 1 & 0 & 0 & & 0 \\ 1 & -2 & 1 & 0 & \dots & 0 \\ 0 & 1 & -2 & 1 & & 0 \\ & \vdots & & & \ddots & 0 \\ 0 & 0 & 0 & 0 & 1 & -2 \end{bmatrix}, \tag{17}$$

assuming open boundary conditions. For the two-dimensional derivative in x and y, the approximated function $\tilde{f}(x,y) \equiv f(\tilde{x},\tilde{y})$ becomes an $N_x \times N_y$ matrix. The Laplace operator can be expressed as a tensor with the shape $N_x \times N_y \times (N_x \cdot N_y)$. Alternatively, the state $\tilde{f}(x,y)$ can be redefined as a one-dimensional vector $\tilde{f}(r)$ with $N_x \cdot N_y$ elements. Here, r is determined by an enumeration $I : \mathbf{G} \to \mathbb{N}$, given by $r_{i,j} = x_i \cdot N_x + y_j$. The corresponding Laplacian would then have the

form $(N_x \cdot N_y) \times (N_x \cdot N_y)$. In the case of non-periodic boundary conditions, the two-dimensional Laplace operator would have the form

$$\Delta_{x,y} \approx \begin{bmatrix} -\frac{2}{d_x^2} - \frac{2}{d_y^2} & \frac{1}{d_x^2} & \cdots & \frac{1}{d_y^2} & \cdots & \\ \frac{1}{d_x^2} & -\frac{2}{d_x^2} - \frac{2}{d_y^2} & \frac{1}{d_x^2} & \cdots & \frac{1}{d_y^2} & \cdots \\ & & & \ddots & & \\ \cdots & \frac{1}{d_y^2} & \cdots & & \frac{1}{d_x^2} & -\frac{2}{d_x^2} - \frac{2}{d_y^2} \end{bmatrix}. \tag{18}$$

Here, the first off-diagonal elements are zero for every N_x'th value. The two-dimensional Laplace operator in equation (18) can be more conveniently expressed using a Kronecker sum of two one-dimensional Laplace operators [Brewer (1978)]. The Kronecker sum for two matrices of the same size, M_1 and M_2, is given by

$$M_1 \oplus M_2 = M_1 \otimes \mathbb{1} + \mathbb{1} \otimes M_2, \tag{19}$$

where $\mathbb{1}$ represents the identity matrix with the same dimensions as M_1 and M_2 [Brewer (1978)]. Employing this approach, the Laplace operator of a two-dimensional system, $\Delta_{x,y}$, can be expressed using the Laplace operators for individual one-dimensional systems, Δ_x and Δ_y. This is explicitly written as

$$\Delta_{x,y} = \Delta_x \oplus \Delta_y = \Delta_x \otimes \mathbb{1} + \mathbb{1} \otimes \Delta_y. \tag{20}$$

Boundary Conditions

Boundary conditions for a general partial differential equation can be either Neumann or Dirichlet conditions. Dirichlet conditions involve setting the boundary points to known values, while Neumann conditions involve setting the derivatives. These boundary conditions can be expressed generally as

$$u = g_D \quad \text{(Dirichlet)} \quad \text{or} \quad \frac{\partial u}{\partial n} = g_N \quad \text{(Neumann)} \quad \text{on } \delta\Omega \tag{21}$$

where g_D and g_N can be functions of x and y. The normal direction, $\frac{\partial}{\partial n}$, is typically chosen to point away from the domain.

3.2 Error evaluation methods

The error evaluation methods included here are related to the propagation of error in products and chi-squared error approximation.

Error propagation

Consider a function $z(x_1, x_2, x_3...)$ represented as the product $z(x_1, x_2, x_3...) = x_1^l \cdot x_2^m \cdot x_3^n ...$, where $x_1, x_2, x_3...$ are variables with uncertainties $\delta x_1, \delta x_2, \delta x_3....$ The uncertainty in z can then be expressed as

$$\frac{\delta z}{z} = |l|\frac{\delta x_1}{x_1} + |m|\frac{\delta x_2}{x_2} + |n|\frac{\delta x_3}{x_3} \ldots, \tag{22}$$

from Adams (2013).

Chi-square error approximation

The chi-square error approximation is a method employed in interpolation to estimate the error between a collection of data points and a function that approximates these data points. Let (x_i, y_i) denote the observed data points, $(x_i, f(x_i))$ represent the value of the function at that point, and σ_i^2 be the variance of the data point. The chi-square error can then be formulated as

$$\chi^2 = \sum_{i=1}^{k} \frac{(y_i - f(x_i))^2}{\sigma_i^2}, \tag{23}$$

where the sum extends over all k data points [Press et al. (2007)].

3.3 Quantum theory

Quantum theory postulates that for any observable physical quantity q, there exists a corresponding operator $\hat{O}$ [Hemmer (2005)]. Furthermore, measurements of the observable can only produce values that are eigenstates of this corresponding operator, q_i. The eigenvectors of the problem are the projections of the system's state wave function, $\Psi(\mathbf{r}, t)$, onto the space associated with the operator. The wave functions $\Psi(\mathbf{r}, t)$ are the eigenstates of the Schrödinger equation. The postulates of quantum theory further say that the wave function $\Psi(\mathbf{r}, t)$ completely characterizes the system's state. In terms of mathematics, $\Psi(\mathbf{r}, t)$ exists in a Hilbert space, with its dimension equaling the number of potential states the system can attain through measurement, which is frequently, but far from always infinite. This is expressed in the Schrödinger equation given by

$$i\hbar \frac{\partial}{\partial t} |\Psi(\mathbf{r}, t)\rangle = \hat{H} |\Psi(\mathbf{r}, t)\rangle . \tag{24}$$

Here, $\hat{H}$ represents the energy operator, also known as the Hamilton operator, or *Hamiltonian* from its classical counterpart. The allowed energies and states of the system are the eigenvalues and eigenstates of $\hat{H}$, and the Schrödinger equation gives their time-evolution. The Hamiltonian is defined as

$$\hat{H} = \frac{\hat{P} \cdot \hat{P}}{2m} + V(\mathbf{r}, t), \tag{25}$$

where the initial term corresponds to the system's kinetic energy, and the second term represents potential energy. $\hat{P}$ is the kinetic momentum operator. When the potential is time-independent, i.e., $V(\mathbf{r}, t) = V(\mathbf{r})$, the equation can be solved using separation of variables. Setting $|\Psi(\mathbf{r}, t)\rangle = \xi(t) |\psi(\mathbf{r})\rangle$, we obtain

$$\begin{aligned} i\hbar \frac{\partial}{\partial t} \xi(t) &= E\xi(t), \\ \hat{H} |\psi(\mathbf{r})\rangle &= E |\psi(\mathbf{r})\rangle . \end{aligned} \tag{26}$$

The first equation in (26) has the solution $\xi = e^{-iEt/\hbar}$, with the integration constant set to zero. The second equation in (26) represents the time-independent Schrödinger

equation. For the systems under consideration, the kinetic momentum operator $\hat{P}$ in (25) is $-i\hbar\nabla$, and the Hamiltonian is time-independent. This results in

$$\hat{H} = -\frac{\hbar^2}{2m}\nabla^2 + V(\mathbf{r}). \tag{27}$$

3.4 Matrix formulation of quantum operators

Let us examine the time-independent Schrödinger equation as shown in (26). Assume that $|u_i\rangle$ constitutes a full set of orthonormal basis vectors, allowing the system's wave function to be expanded within these basis states, as

$$|\psi\rangle = \sum_i |u_i\rangle . \tag{28}$$

For a quantum mechanical operator $\hat{O}$, the operator's expectation value is expressed by

$$\left\langle \hat{O} \right\rangle = \langle\psi| \hat{O} |\psi\rangle , \tag{29}$$

[Hemmer (2005)]. Expanding the wave function results in

$$\left\langle \hat{O} \right\rangle = \sum_{i,j} O_{ij}, \text{ where} \tag{30}$$

$$O_{i,j} = \langle u_i| \hat{O} |u_j\rangle . \tag{31}$$

In this context, $O_{i,j}$ is known as the matrix element, and the expectation value can be written in its expanded form as

$$\left\langle \hat{O} \right\rangle = \begin{bmatrix} O_{1,1} & O_{1,2} & \dots & O_{1,N} \\ O_{2,1} & O_{2,2} & & \\ \vdots & & \ddots & \\ O_{N,1} & & & O_{N,N} \end{bmatrix} . \tag{32}$$

3.5 Quantum transport theory

Transmission through a medium is evaluated using the quantum scattering theory of transport and the Landauer-Büttiker formalism. This is then used to derive current and conductance. The theory was first put forward by Rolf Landauer in 1957 [Landauer (1957)], and further developed by Markus Büttiker in 1988 [Büttiker (1988)]. The formalism is well-suited for the study of mesoscopic and nanoscale systems, where the dimensions are comparable to the electron wavelength, and quantum effects become significant. An alternative approach could use Green's functions, however, the theories are equivalent and related through what's known as the Fisher-Lee relation [Datta (2005) ch. 9, and Datta (1995) ch. 3].

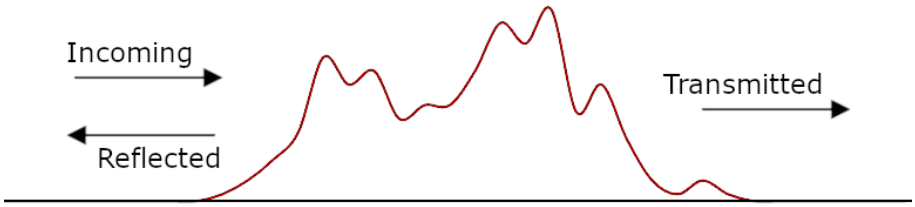


Figure 8: One-dimensional scattering process. An incoming wave scatters against a potential of a finite extent. A part of the wave is reflected, creating interference with the incoming wave, while the rest is transmitted. The regions before and after the potential are referred to as leads or reservoirs.

Consider a one-dimensional system where an incoming plane wave scatters against a region of finite potential. For convenience, assume that the potential $V(x)$ is independent of time, although it is straightforward to include time dependency. The potential $V(x)$ is greater than zero in the domain $x \in (0, D)$, and zero otherwise. The system is depicted in Figure 8. This system will be treated with a basis in the approach of Datta (1995). An equivalent derivation holds for higher dimensions with only small adjustments. See Chapter 3 of Datta (1995) for more details.

Scattering

Some of the incoming wave in Figure 8 is transmitted, while the rest is reflected. The wave function describing the quantum particle to the left of the potential is then given by

$$\psi^L(x) = e^{ikx} + re^{-ikx}. \tag{33}$$

The first term is the incoming plane wave, and the second term arises from the part reflected by the potential. In principle, the weights in front of both terms could be solved generally. Here it is however imposed that the coefficient in front of the incoming wave should be 1, and we're solving for the corresponding r. In the region of finite potential, the state is given by the time-independent Schrödinger equation (26). Lastly, after the scattering region, the transmitted wave function is given by

$$\psi^R(x) = te^{ikx}, \tag{34}$$

where the superscript refers to this being to the right of the scattering region in the depicted system. The two regions before and after the scattering region are referred to as leads or reservoirs.

Solving the Schrödinger equation

The system will now be solved for the leads, the scattering region and the boundary layers between them. First, insert the a plane wave $\psi(x) = e^{ikx}$ into (26) with $V = 0$, yielding

$$E(k) = \frac{\hbar^2 k^2}{2m} \tag{35}$$

This is then the dispersion relation for the one-dimensional wire in the leads. The solution within the scattering region will depend on the exact potential $V(x)$, and we write this simply as $\psi^{inside}(x)$. Finally, consider the boundary layer between the scattering region and the leads. Matching the wave functions and derivatives at the transitions yields

$$\begin{aligned}
\psi(0^-) = \psi(0^+) &\rightarrow 1 + r = \psi^{inside}(0) \\
\psi(L^+) = \psi(L^-) &\rightarrow t = \psi^{inside}(L) \\
\frac{d\psi(x)}{dx}\Big|_{x=0^-} = \frac{d\psi(x)}{dx}\Big|_{x=0^+} &\rightarrow ik \cdot (1 + r) = \frac{d\psi^{inside}(x)}{dx}\Big|_{x=0} \\
\frac{d\psi(x)}{dx}\Big|_{x=L^+} = \frac{d\psi(x)}{dx}\Big|_{x=L^-} &\rightarrow ik \cdot t = \frac{d\psi^{inside}(x)}{dx}\Big|_{L=0}
\end{aligned} \tag{36}$$

The system is then solved for the state vector.

Solving this system yields values for r and t. Next, consider sending a wave through the potential in the opposite direction. That is, from right to left in Figure 8. This gives transition- and reflection amplitudes r', t'. The results are conveniently combined in the scattering matrix, given as

$$S = \begin{bmatrix} r & t' \\ t & r' \end{bmatrix}. \tag{37}$$

Particle current

In order to find physical observables, start by considering the particle current. For non-relativistic systems, the probability current associated with a wave function is given by

$$\mathbf{J} = \frac{\hbar}{2mi}\left[\psi^*(x)\frac{\partial}{\partial x}\psi(x) - \psi(x)\frac{\partial}{\partial x}\psi^*(x)\right] \tag{38}$$

see Hemmer (2005) or another elementary textbook on quantum mechanics. Equation (38) can be evaluated for each lead by inserting $\psi^L(x)$ and $\psi^R(x)$. For the right lead, $\psi^R(x) = te^{ikx}$, and (38) becomes

$$J^R = \frac{\hbar k}{m}|t|^2. \tag{39}$$

Next, define the velocity $v(k)$ as $\hbar v(k) \equiv \frac{\partial}{\partial k}E(k)$. In higher dimensions, the currents and velocities are vectors. Making use of the dispersion relation in (35), this yields $v(k) = \hbar k/m$, and (39) can be rewritten as

$$J^R = |t|^2 v(k) \tag{40}$$

Equation (40) is often found written as $J = n \cdot v(k)$, where n refers to the particle density, here simply $|t|^2$.

Next, inserting $\psi^L(x) = e^{-ikx} + re^{ikx}$ into (38) and making use of the same velocity yields

$$J^L = \left(1 - |r|^2\right) v(k) \tag{41}$$

for the left lead.

Conservation of current dictates that the incoming and outgoing current in the system must be equal, giving

$$1 - |r|^2 = |t|^2 = |t'|^2 = 1 - |r'|^2 \tag{42}$$

This is equivalent to stating that the scattering matrix in (37) is unitary, $SS^\dagger = 1$. This means that the scattering matrix conserves amplitudes through time evolution, which is a general criterion for all quantum mechanical operators [Hemmer (2005)]. However, it is worth mentioning as a sidenote that although the total system always needs to be unitary, non-unitary operators are commonly found in the literature on quantum transport. These typically appear in the context of dissipation and decoherence. The implication is then made that one is considering a particular subsystem, which in itself is non-unitary. For example, a lab setup that is influenced by human measurements. However, such a system must then be coupled to an external system through collapse operators. In the case considered in this thesis, the scattering matrix is unitary itself.

Physically observable quantities

The particle current in (38) only describes the flow of particles per quantum state, which is unsuited for measurements in the lab. However, the real electrical current can be calculated from this in just a few extra steps. First, consider the average current produced by a single state i. This must be given by the charge of the carrier q, times the probability current of the state J, multiplied by the probability of the state being occupied. For electrons, the charge $q = -e$ and the probability distribution is given by the Fermi-Dirac distribution $f(E)$ [Hemmer (2005)]. Finally, the probability current J is given by (38). In order to obtain the observable electrical current, one needs to fill the states up to the Fermi level and integrate over all momentum of incoming states k. This yields

$$\begin{aligned} I &= -\frac{2e}{\hbar}\int \frac{dk}{2\pi} J \cdot f[E(k)], \text{ with} \\ f(E) &= \frac{1}{e^{(E-\mu)/kT}+1}, \end{aligned} \tag{43}$$

where the factor 2 is included to account for spin degeneracy. Apply (43) for the left and right leads separately, with different particle currents and Fermi-Dirac distributions, giving

$$\begin{aligned} I &= \frac{2e}{\hbar}\int \frac{dk}{2\pi} v(k) \left\{ \left(1-|r|^2\right) f^L[E(k)] - |t|^2 f^R[E(k)] \right\}, \text{ with} \\ f^L[E(k)] &= \frac{1}{e^{(E(k)-\mu^L)/k_B T^L}+1}, \text{ and } \; f^R[E(k)] = \frac{1}{e^{(E(k)-\mu^R)/k_B T^R}+1}. \end{aligned} \tag{44}$$

In one dimension, the velocity is the inverse of the density of state, dk/dE. Use this to rewrite the integral to run over energy instead. Next, set $1 - |r|^2 = |t|^2$ yielding the Landauer formula, namely

$$I = \frac{2e}{h}\int dE |t|^2 \left\{ f^L[E(k)] - f^R[E(k)] \right\}. \tag{45}$$

At zero temperature, the Fermi-Dirac distributions become step functions given by $f[E(k)] = 1$ for $E(k) < \mu$ (the Fermi energy) and $f[E(k)] = 0$ for $E(k) > \mu$. This is because at zero temperature all states up to the Fermi energy are occupied and all states above it are empty. Consider a small deviation from the Fermi energy in each lead, writing the chemical potentials as $\mu^L = E_F + eV/2$, and $\mu^R = E_F - eV/2$. This gives a slight difference in the Fermi energy levels, creating a voltage bias V across the system. Energies below μ^R or above μ^L do not contribute to the current in (45) since the differences between the Fermi-Dirac distributions $f^L[E(k)] - f^R[E(k)]$ are zero. The integral over energy in (45) therefore becomes an integral from μ^R to μ_L. Putting this together, in the zero-temperature limit, the current expression simplifies to

$$I = \frac{2e}{h} \int_{\mu^R}^{\mu^L} dE|t(E)|^2. \tag{46}$$

Finally, assume that the transmission probability $|t|^2$ does not change much over the energy range from μ^R to μ^L and that it can be approximately evaluated at the Fermi level E_F. Pulling $|t|^2$ out of the integral leads to the Landauer formula, namely

$$I = \frac{2e}{h}|t(E_F)|^2 eV = \frac{2e^2}{h}|t(E_F)|^2 V. \tag{47}$$

This is the Ohmic behavior expected in the linear response regime and provides a good approximation provided that the applied voltage is small enough and the temperature is low enough. From the Ohmic relation $I(E) = g(E)V$, the conductance is then given by

$$g(E_F) = \frac{2e^2}{h} \cdot |t(E_F)|^2 = G_0|t(E_F)|^2. \tag{48}$$

Note that this is the conductance from the eigenstate at energy E_F, and it will be evaluated for varying E_F. This is sometimes called the conductance fluctuations or the differential conductance. This differs from the total conductance, often denoted $G(E)$ and given as

$$G(E) = \int_0^E g(E)dE$$

where all the conducting states up to the desired energy are integrated.

From (48) one can observe a general property, namely that the maximum conductance through one channel connecting two leads is given by q^2/h [Datta (2005)]. This can be seen by realizing that the factor $|t|^2$ can take a maximum value of 1, and that there are in fact two channels available in the discussed system, one for each electron spin configuration, yielding the factor of 2 in (48). The factor $G_0 = 2e^2/h \approx 7.75 \times 10^{-5} S$ is called the conductance quantum.

In real systems, one can have multiple different modes in the leads. Even if the leads are 1D wires, there are different modes available at different energies. These modes can be thought of as different energy channels available for transport, and each of these modes has its own transmission probability. Label the incoming modes k and the outgoing l, and the left lead by L and the right lead by R. Instead of a single transmission probability t as in (48), one now has a scattering matrix S, where each element $S_{k,l}$ gives the amplitude for an electron to scatter from mode k to mode l.

To get total conductance from the left lead to the right lead, one then sums over all incoming and outgoing modes, giving

$$g(E) = \frac{2e^2}{h} \sum_{k \in L,\, l \in R} |S_{k,l}|^2. \tag{49}$$

The method described here holds for coherent transport. This is the case when the objects that the wave scatters against can be considered constant and unaffected by the impact. On the other hand, if an incoming electron scatters against a crystal structure, causing the atoms to oscillate significantly, the transport is not coherent.

3.6 Level spacing statistics and random matrix theory

Random matrix theory (RMT) is a mathematical framework initially introduced by Eugene Wigner to model the energy levels of heavy atomic nuclei [Wigner (1955)]. In particular, RMT states that the level spacing statistics of random matrices will follow predictable distributions depending on the matrices' symmetries. By classifying the properties of these random matrices, one can predict results for physical systems with the same symmetries. Much of the mathematical framework in the field was developed by Madan Lal Mehta [Mehta (1967), Mehta (2004)].

Level spacing statistics and random matrix theory are interrelated fields often applied to quantum mechanics, particularly in the realm of quantum chaos [Gutzwiller (1990), Chapter 16]. In this context, level spacing refers to the differences between consecutive energy levels of a quantum system. The study of level spacing statistics is typically concerned with the probability distribution $P(\Delta E)$ of spacings ΔE between energy levels. The distribution $P(\Delta E)$ is computed from the spacings $\Delta E_n = E_{n+1} - E_n$, where E_n is the nth energy level, and it is assumed that the energy levels are sorted an normalized. The normalization process is done such that the mean level spacing becomes 1, and the distribution $P(\Delta E)$ beomes a density. Details of the normalization process will be discussed further in Section 5.6.

Freeman Dyson categorized random matrices into three classes depending on their symmetry properties [Dyson (1962)]. These are the Gaussian Orthogonal Ensemble (GOE), the Gaussian Unitary Ensemble (GUE) and the Gaussian Symplectic Ensemble (GSE). This led to the prediction of three different types of level spacing statistics, now known as the Wigner-Dyson distributions. Consider the properties of these three main classes of matrices [Mehta (2004), Chapter 2].

The first class of matrices is the Gaussian Orthogonal Ensemble (GOE), which is a set of real symmetric matrices with elements that have a Gaussian probability distribution. Their physical counterparts are systems with time-reversal symmetry and no spin-orbit coupling. The Hamiltonians of such systems are real and symmetric. The level spacings $P(\Delta E)$ of these systems follow the distribution given by

$$P_{GOE}(\Delta E) = \frac{\pi}{2} \cdot \Delta E e^{-\pi \Delta E^2/4}, \tag{50}$$

see Chapter 4 of Haake (2010).

The second class is the Gaussian Unitary Ensemble (GUE), composed of complex Hermitian matrices invariant under unitary transformations. These then represent systems without time-reversal symmetry, so that the Hamiltonian becomes complex. These level spacings of systems are described by the distribution

$$P_{GUE}(\Delta E) = \frac{32}{\pi^2} \cdot \Delta E^2 e^{-4\Delta E^2/\pi}. \tag{51}$$

The third and final main class is the Gaussian Symplectic Ensemble (GSE) which is composed of quaternionic Hermitian matrices invariant under symplectic transformations. These represent systems with time-reversal symmetry and half-integer spin.

$$P_{GSE}(\Delta E) = \frac{262144}{729\pi^3} \cdot \Delta E^4 e^{-64\Delta E^2/(9\pi)}, \tag{52}$$

The three distributions (50), (51) and (52) are referred to as Wigner-Dyson distributions and can be written compactly as

$$P(\Delta E) = C \cdot \Delta E^{\beta} e^{\alpha \cdot \Delta E^2}. \tag{53}$$

The key observation is the different values of the exponent β in the GOE, GUE and GSE. For small values of ΔE, the exponential factor in the Wigner-Dyson distribution can be approximated by writing $exp(\alpha \cdot \Delta E^2) \approx 1 + \alpha \cdot \Delta E^2 \approx 1$. In this case, the GOE, GUE and GSE follow increasing power laws with exponents $\beta = 1$, $\beta = 2$ and $\beta = 4$, respectively.

Level repulsion: Chaotic, periodic and quasi-periodic systems

Level repulsion describes the statistical tendency for energy levels of a quantum system to avoid crossing one another [Haake (2010), Chapter 3]. Level repulsion is one of the key signatures of quantum chaos. That is, the energy levels of quantum systems that exhibit chaotic (aperiodic) behavior are less likely to be closely spaced than what one would expect if the levels were independent of each other. This is understood as an increased coupling strength between different degrees of freedom in chaotic systems, leading to level crossings being avoided [Gutzwiller (1990), Chapter 16.4].

Level repulsion is closely related to the Wigner-Dyson distributions discussed above. This is because the Hamiltonians of systems corresponding to the GOE, GUE, and GSE have linear, quadric and quartic level repulsions, respectively [Haake (2010), Chapter 3.4]. This means that, for example, for the GOE the probability of finding two eigenvalues very close together is suppressed, and the probability increases linearly with their spacing. The degree of level repulsion can be measured directly by measuring the slope of the power law scaling, β, at low energy level spacings. By measuring the value of β one then determines the Wigner-Dyson distribution of the system and gains information about the level repulsion. In turn, this helps determine whether the system displays chaotic (aperiodic) behavior or not.

On the other hand, integrable, typically periodic, systems do not display level repulsion. That is, these systems have quantum energy levels that can cross each

other since the different degrees of freedom are independent. This leads to a high probability of small energy level spacings. In fact, the energy level spacing of such systems follows a Poisson distribution, given by

$$P(\Delta E) \propto e^{-\Delta E}. \tag{54}$$

An illustration of the Poisson distribution together with the three discussed Wigner-Dyson distributions is borrowed from Haake (2010) and given in Figure 9. In this illustration, the Poisson distribution is labeled $\beta = 0$, however, this is slightly misleading as simply setting $\beta = 0$ in (53) would yield a Gaussian distribution, and not a Poisson. As seen from this figure, a high degree of level spacing repulsion yields a more narrowly peaked energy level spacing distribution. One sees that the probability of observing small energy level spacings is suppressed in the Wigner-Dyson distributions.

Finally, quasi-periodic systems can show a crossover between these two behaviors, depending on the specific parameters of the system.

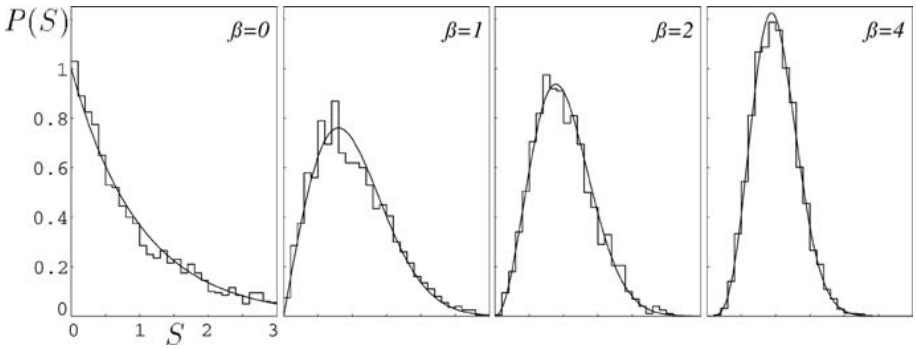


Figure 9: The figure depicts different level-spacing distributions corresponding to systems with different symmetry properties. The integrable, periodic system has no level repulsion and its level spacing distribution resembles the Poisson distribution labeled here by $\beta = 0$. The remaining three distributions display level repulsion and correspond to aperiodic systems. Particularly, linear, quadric and quartic level spacing repulsion corresponds to Wigner-Dyson distributions with $\beta = 1$, $\beta = 2$ and $\beta = 4$, respectively. This is related to the symmetries of the systems. Quasi-periodic systems can display an interplay between the Poisson and Wigner-Dyson distributions.

Source: Haake (2010).

4 Studied fractals

The creation and representation of the fractals are discussed here as well as some properties. Detailed information for a representative selection of fractals is also included here. A more exhaustive list of the studied fractals is found in Appendix B. Parts of this discussion were first introduced in Akre (2023).

The fractals studied in this project thesis are all self-similar. That is, they appear to consist of multiple copies of themselves. Most are perfectly self-similar as defined in

Section 2.2 and satisfy the open set condition, but not all. Furthermore, the fractals considered here are simply connected as we want the wavefunctions to spread out and occupy the fractal. That is with the exception that the fractal can be divided by fully localized points or lines of zero width. In these cases, a wavefunction placed upon the fractal can still reside on either side of the dividing barrier, so long the wavefunction's amplitude can be positive on one side, zero at the barrier and negative on the other side. Lastly, as the fractal iteration increases the available area in the system should tend toward zero. This choice is made partly because these fractals are expected to exhibit similar properties. In addition, the complexity of Hamiltonians of fractals with vanishing areas can be dramatically reduced. For the sake of rigorousness, we next define exactly what is meant by the fractal iteration. In addition, notes are given on the quantization of grid resolutions.

4.1 Fractal iteration and the linear length scale resolution

A fractal has infinite detail, and however much one zooms in on it, it never smoothens. This is not numerically obtainable, and instead, details are added successively to an object. By doing calculations for these intermediate stages, one hopes to be able to extrapolate information for the infinitely detailed system. The intermediate steps are referred to by a fractal iteration $l \in \mathbb{N}$. Here, $l = 0$ is a completely open system and $l = 1$ adds the first layer of detail. For a perfectly self-similar object, the transition from l' to $l' + 1$ should satisfy the following. $l' + 1$ should consist only of copies of iteration l'. Furthermore, $l' + 1$ should not be dividable into any larger, identical constituents than the object from l'. That is, l' should be the largest possible set that constitutes $l' + 1$ besides itself. Intuitively, this clarification is simply made to forbid going directly from for example fractal iteration $l = 1$ to $l = 3$, skipping an intermediate step. This is important when comparing the properties of different fractals.

Consider the grid resolutions $N \times N$ needed to represent the fractals. Here, N is the linear grid resolution. As will be seen in the following, these grid resolutions are highly different for the fractals. Therefore, a different metric is introduced, namely the linear length scale resolution $n \in \mathbb{N}$. The linear length scale resolution n gives the number of grid points used to represent the smallest linear length scale of the fractal. This will be used in most cases, and it makes it easier to compare results from different fractals.

4.2 The Method of Repeated Kronecker Products

To efficiently generate fractals, an iterative method was developed using repeated application of Kronecker products.

Define a matrix G called the "generator" and a matrix A_0 called the "axiom". The elements of both matrices are either 0 or 1. The fractal at fractal iteration $l' + 1$ is denoted $A_{l'+1}$ and is found as the Kronecker product of G and $A_{l'}$. The fractal is then generated by taking the product of G and $A_{l'}$ repeatedly, each time updating

the value of $A_{l'}$ to the last result until the desired iteration depth is reached. The first generation A_1 is calculated from the Kronecker product between the generator G and the axiom A_0. That is

$$A_{l'+1} = G \otimes A_{l'} = \begin{bmatrix} g_{1,1}A_{l'} & g_{1,2}A_{l'} & \dots & g_{1,n}A_{l'} \\ g_{2,1}A_{l'} & g_{2,2}A_{l'} & & \\ \vdots & & \ddots & \\ g_{n,1}A_{l'} & & & g_{n,n}A_{l'} \end{bmatrix} = G \otimes G \otimes \cdots \otimes A_0. \tag{55}$$

The scheme generates a self-repeating pattern defined by the instructions in G, and A_l acts as an evolving building block. Any fractal generated by this scheme fulfills the open set condition in (7) and is perfectly self-similar. This is because only the last iteration is used to generate the next, and there is no overlap. Therefore, the Hausdorff dimension D_H equals the similarity dimension D_S. Furthermore, the similarity dimension is trivial to find, and therefore also the Hausdorff. This can be seen by noting that each non-zero element in G propagates a copy of the previous iteration into the next. That is, each non-zero element of G means that there's a copy of the last iteration in the next. In the limit of infinite iterations, this means that there's an *exact* copy of the system in itself. Therefore, by summing the elements of G one finds the number of copies m used in the similarity dimension. The scaling factor r can be found as the linear side length of G. That is, the shape of G is $r \times r$. The fractal dimension is found using (6) to be

$$D_H = D_s = \frac{\log\left(\sum_{i,j} g_{i,j}\right)}{\log(r)}. \tag{56}$$

Notice that the properties of A_0 do not affect the fractal dimension, and fractals with the same generator will have the same fractal dimension. This shows that fractals that can be created through this algorithm are expected to share fractal dimensions with many other fractals. This corresponds to a degeneracy for a given fractal dimension.

Lastly, the topological dimension of our system is the dimension of G, that is 2. Therefore, in addition to providing a highly efficient routine to generate fractals, the Method of Repeated Kronecker Products also yields directly the Hausdorff dimension D_H, the number of copies m, the rescaling factor r and the topological dimension D_L, which are all the measures we need to characterize the fractals in this thesis.

4.3 Sierpinski Carpet

The base of a Sierpinski Carpet is a blank square. A smaller square of side lengths 1/3 of the original in the center of the base is colored black, this is fractal iteration $l = 1$. This new shape can be thought of as a central black square with eight smaller copies of the base placed around it. Repeat the operation, coloring squares inside the eight new basis', yielding 8×8 new smaller basis'. This is fractal iteration $l = 2$. Repeating the process infinite times yields the Sierpinski Carpet fractal. The

process is depicted in Figure 10. The colored areas are to be considered illegal later, that is, having high potential.

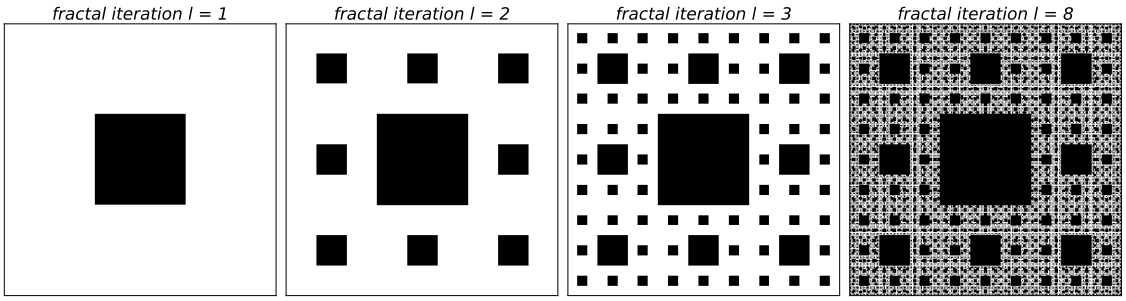


Figure 10: The first few fractal iterations l of the Sierpinski Carpet. Each iteration consists of eight copies of the last.

The Sierpinski Carpet can be generated using the Method of Repeated Kronecker Products described in Section 4.2. To do so, set the generator G and axiom A_0 equal to

$$\begin{aligned} G &= \begin{bmatrix} 1 & 1 & 1 \\ 1 & 0 & 1 \\ 1 & 1 & 1 \end{bmatrix}, \text{ and} \\ A_0 &= 1. \end{aligned} \tag{57}$$

To exactly represent the shape of the object, only certain grid resolutions are adequate. Inspecting the fractal iteration $l = 2$ in Figure 10 it is clear that $9, 18, 27 \ldots$ are linear resolutions that accurately capture the object. On the other hand, a grid resolution $N \times N$ of for example 17×17 would not. Some of the allowed linear resolutions are shown in Table 1. The resolutions follow the function

$$N_{l,n} = 3^l \cdot n.$$

Here, n gives the number of grid points used to represent the smallest length scale of the fractal, called the linear length scale resolution.

Table 1: The allowed grid resolutions of the Sierpinski Carpet.

Fractal iteration l	Allowed linear grid resolutions N
1	3, 6, 9, 12, 15 ...
2	9, 18, 27, 36, 45 ...
3	27, 54, 81, 108, 135 ...
4	81, 162, 243, 324, 405 ...
5	243, 486, 729, 972, 1215 ...
6	729, 1458, 2187, 2916, 3645 ...

Consider next the dimensionality of the Sierpinski Carpet, following the discussion of Section 2.2. The topological dimension, or Lebesgue dimension, is $D_L = 2$. Next,

study the Sierpinski Carpet for a fractal iteration $l = 3$ and $l = 2$. The former consists of eight copies of the latter, exactly. In the limit $l \to \infty$, the Sierpinski Carpet consists of eight exact copies of itself, and we have $m = 8$ in (6). Each of these copies is rescaled linearly by a factor of $1/r = 1/3$. Furthermore, the fractal is perfectly self-similar, and per the discussion in Section 2.2, the Hausdorff dimension D_H equals the similarity dimension D_S. Using (6) gives then a similarity and Hausdorff dimension of $D_H = D_S = \log(8)/\log(3) \approx 1.893$. This could also be found directly from the generating matrix G as discussed in Section 4.2, equation (56). This method will be used when applicable in later examples. The area of the Sierpinski Carpet approaches zero as the fractal iteration l grows.

4.4 Filled Sierpinski Square

The filled Sierpinski Square, or simply the Sierpinski Square, can be constructed using a Lindenmayer system, or L-system, as described in Section 2.4. In order to create the Sierpinski Square, set the axiom equal to $F + XF + F + XF$ and define the rules

$$F \to F,$$
$$X \to XF - F + F - XF + F + XF - F + F - X.$$

Iterating this generates a string of instructions. Next, interpret F as a straight line and X as nothing. Set the angle rotated by $+/-$ to $90°$ and draw the result on a grid. The result of the process is shown in Figure 11.

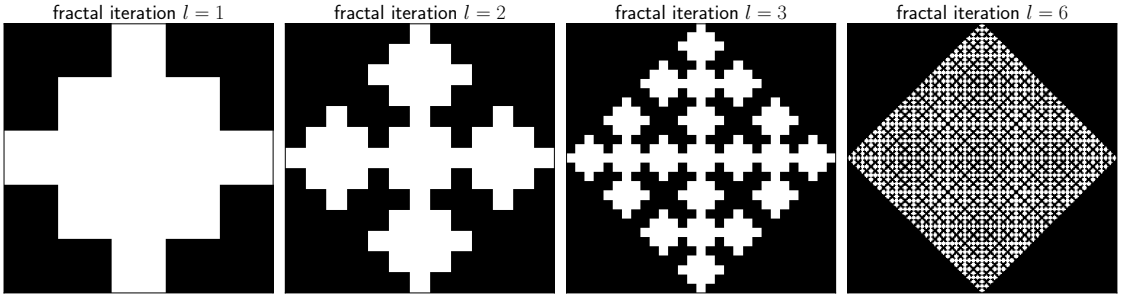


Figure 11: The first few fractal iterations l of the Sierpinski Square.

The allowed linear grid resolutions N are given in Table 2. The resolutions follow the equation

$$N_{l,n} = \left[1 + 4 \cdot \sum_{a=1}^{l} 2^{a-1}\right] \cdot n. \tag{58}$$

Table 2: The allowed linear grid resolutions of the Sierpinski Square.

Fractal iteration l	Allowed linear grid resolutions N
1	5, 10, 15, 20, 25 ...
2	13, 26, 39, 52, 65 ...
3	29, 58, 87, 116, 145 ...
4	61, 122, 183, 244, 305 ...
5	125, 250, 375, 500, 625 ...
6	253, 506, 759, 1012, 1265 ...

Inspecting Figure 11, note that the fractal iteration $l = 3$ consists of four copies of iteration $l = 2$, connected through a central box. As the fractal iteration, l tends towards infinity, the fractal will consist of four exact copies of itself, connected through a central box. The fractal is not perfectly self-similar, and the open set condition is not satisfied. Therefore the Hausdorff dimension and similarity dimension are not necessarily equal. However, the central box has an area that tends toward zero as l approaches infinity, it is proportional to $(3^l)^{-2}$. Therefore, neglect the contribution from the central square in the limit of $l \to \infty$. Ignoring the central box, the fractal becomes perfectly self-similar. Furthermore, the sides of the four smaller copies constituting the fractal are of a length scale $1/2$ of that of the fractal. This gives a dimension equal to $D_H \approx D_S \approx \log(4)/\log(2) = 2$. This means the Sierpinski Square seems to have scaling properties similar to that of a regular two-dimensional object. This is not a fractal by the original definition given by Mandelbrot but shares many of the same properties.

4.5 Filled Sierpinski Curve

As was the case for the Sierpinski Square, the filled Sierpinski Curve can also be constructed using a Lindenmayer system. To create the Sierpinski Curve, set the axiom equal to $F--XF--F--XF$ and define the rules

$$F \to F,$$
$$X \to XF + G + XF--F--XF + G + X.$$

Analogous to the Sierpinski Square, F is interpreted as a straight line and X as doing nothing. However, G is now interpreted as a straight line with length $\sqrt{2}$ longer than that of F. The angle of rotation is set to 45°. The result is shown in Figure 12.

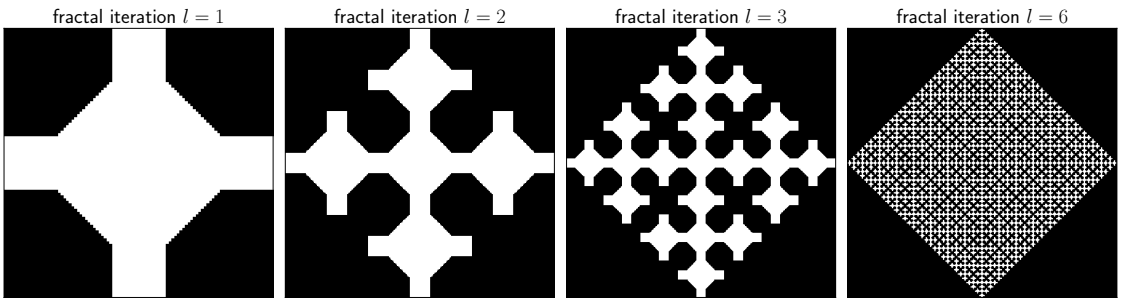


Figure 12: The first few fractal iterations l of the Sierpinski Curve for a resolution $n = 20$. That is, the smallest length scale of the fractal is split into 15 points.

Unlike the fractals considered previously, the Sierpinski Curve has non-square angles. Generally, representing an angle on a square grid will lead to aliasing. That is, it will lead to errors due to the finite partition of the grid. In order to find the best representation of a line with an arbitrary slope at a given grid resolution, the Bresenham line algorithm can be used [Bresenham (1965)]. However, representing a 45° angle is trivial.

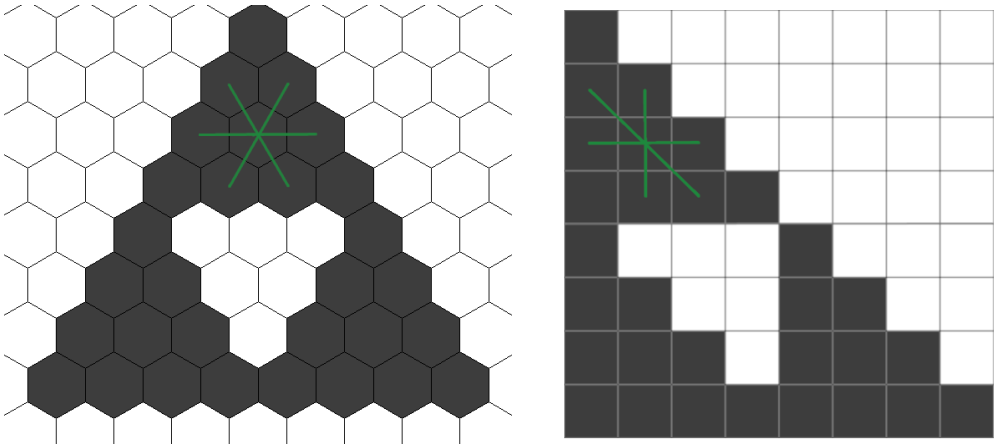
On a square lattice, a 45° degree angle should not lead to any issues so long only nearest neighbor interactions are considered (north, west, south, east). If however second-nearest neighbor couplings were to be considered, there could exist direct couplings between points on opposite sides of a thin 45° barrier. This would be unphysical.

Certain grid resolutions are desired to maintain the symmetries of the curve. The allowed resolutions are the same as those for the Sierpinski Square given in Table 2 and by (58). Note that setting the linear length scale resolution $n = 1$ yields the same shape as the Sierpinski Square.

The dimensionality can be found by the same method as used for the Sierpinski Square. Again the Hausdorff dimension is found to be approximately that of a two-dimensional object, $D_H \approx 2$.

4.6 Sierpinski Gasket

The Sierpinski Gasket has an equilateral triangular base. An upside-down triangle of 1/4 of the measure of the original is then removed from the center of the base. This yields three new bases. The process is repeated for the new bases and so on. The equilateral triangles have 60° angles that are difficult to represent using a square lattice. This could lead to significant aliasing. Fortunately, the Sierpinski Gasket can be accurately expressed using a hexagonal lattice as shown in Figure 13a. In fact, when doing calculations, the structure will still be represented by a regular square matrix. However, the hexagonal lattice can be taken into account in the square matrix by including an extra pair of nearest neighbors. This representation is depicted in Figure 13b.



(a) (b)

Figure 13: Grid representation of the Sierpinski Gasket. In (a) the Sierpinski Gasket is well represented on a hexagonal grid. Figure (b) depicts the Sierpinski Gasket represented on a square grid, treating the upper-left to lower-right diagonal as nearest neighbors.

The object in Figure 13b can be generated using the Method of Repeated Kronecker Products as described in Section 4.2. The generating matrix G and the axiom matrix A_0 are given by

$$\begin{aligned} G &= \begin{bmatrix} 1 & 0 \\ 1 & 1 \end{bmatrix}, \text{and} \\ A_0 &= L_{n+1}^T, \end{aligned} \tag{59}$$

where L_{n+1}^T is the lower triangular matrix of shape $(n+1) \times (n+1)$. Here, n dictates the resolution of the obtained Sierpinski Gasket. A few fractal iterations of the Sierpinski Gasket for grid resolution $n = 3$ are shown in Figure 14.

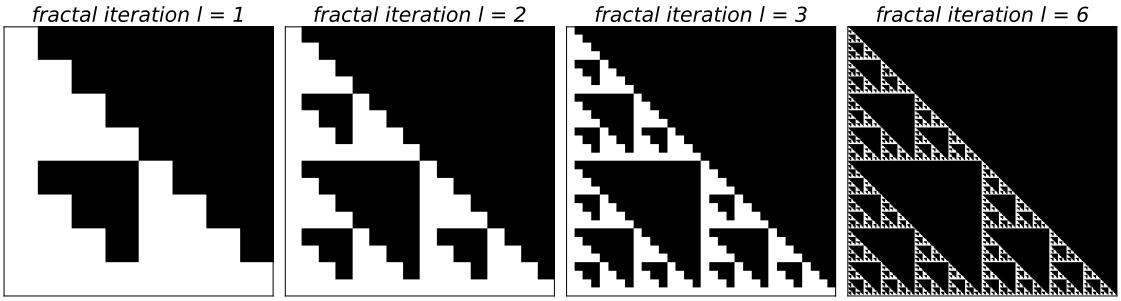


Figure 14: The first few fractal iterations l of the Sierpinski Gasket. This is in the square grid representation and with $n+1 = 4$. That is, the smallest triangles present are represented by 4×4 lower-triangular matrices.

The allowed grid resolutions are given in Table 3 and follow

$$N_{l,n} = 2^l(n+1). \tag{60}$$

Table 3: The allowed grid resolutions of the Sierpinski Gasket.

Fractal iteration l	Allowed linear grid resolutions N
1	4, 6, 8, 10, 12 ...
2	8, 12, 16, 20, 24 ...
3	16, 24, 32, 40, 48 ...
4	32, 48, 64, 80, 96 ...
5	64, 96, 128, 160, 192 ...
6	128, 192, 256, 320, 384 ...

As it was generated by the Method of Repeated Kronecker Products, one can immediately state that it fulfills the open set condition in (7) and that the Hausdorff dimension is given by (56). This yields $D_H = D_S = \log(3)/\log(2) \approx 1.585$.

4.7 Flag-fractal

The last show-cased fractal is the Flag-fractal. This fractal can be constructed using the Method of Repeated Kronecker Products using a generator G and an axiom A_0 given by

$$G = \begin{bmatrix} 0 & 1 & 0 & 0 \\ 0 & 1 & 0 & 0 \\ 1 & 1 & 1 & 1 \\ 0 & 1 & 0 & 0 \end{bmatrix}, \text{and} \qquad A_0 = 1. \tag{61}$$

The first few iterations of the Flag-fractal are shown in Figure 15.

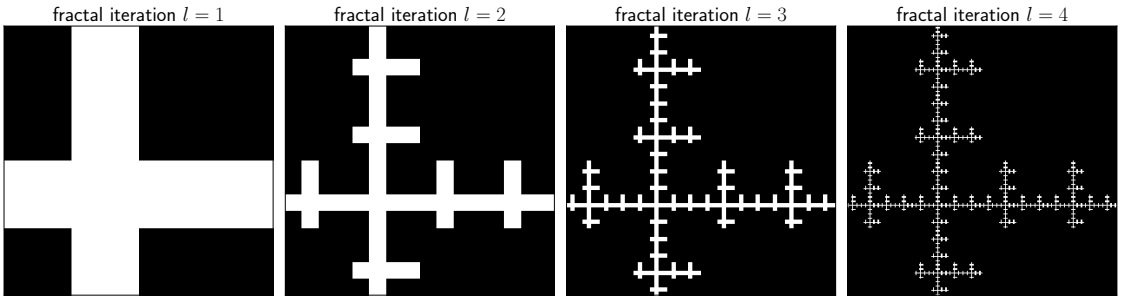


Figure 15: The first few fractal iterations l of the Flag-fractal. The detail in the system grows rapidly.

The details of the fractals grow fast for increasing fractal iteration l, and the allowed grid resolutions follow the function

$$N_{l,n} = 5^l \cdot n. \tag{62}$$

The first few values for the linear grid resolution N are shown in Table 4.

Table 4: The allowed grid resolutions of the Flag-fractal.

Fractal iteration l	Allowed linear grid resolutions N
1	5, 10, 15, 20, 25 ...
2	25, 50, 75, 100, 125 ...
3	125, 250, 375, 500, 625 ...
4	625, 1250, 1875, 2500, 3125 ...
5	3125, 6250, 9375, 12500, 15625 ...
6	15625, 31250, 46875, 62500, 78125 ...

From the generator of the fractal, it is seen that the rescaling factor $r = 5$ and the number of copies $m = 7$. The logic in this is described at the end of Section 4.2. Using (6) one obtains a similiarity dimension $D_S = \log(7)/\log(5)$. Furthermore, as it was generated by the Method of Repeated Kronecker Products, it must fulfill the open set condition in (7). Therefore the Hausdorff is equal to the similarity dimension, that is, $D_H = D_S = \log(7)/\log(5) \approx 1.209$.

The detail of the Flag-fractal grows rapidly as the fractal iteration l is increased. However, it is also worth noting that the allowed area in the fractal tends to zero fast, yielding the small Hausdorff dimension. As it turns out, this makes high-precision calculations still realizable for the system. A discussion on this is given in Appendix A.2.

4.8 Connectivity and ramification number

Before continuing, a remark is made on the concept of connectivity as it will prove useful in later discussions. The connectivity or connectedness of a fractal refers to how many paths there exist connecting two points within the fractal. It will only be used in a broad, qualitative sense in this thesis, and a proper definition will not be put forward.

Consider the Sierpinski Carpet and Sierpinski Gasket as shown in Figures 10 and 14. In a discrete representation of a fractal, the number of available paths will naturally always be finite, as the fractal is represented by a finite collection of sites. However, consider taking the Sierpinski Carpet at a given fractal iteration l' and using an infinite grid resolution. In such a continuous realization of the Sierpinski Carpet, there exists an infinite amount of paths one can take from one point to another. On the other hand, in the Sierpinski Gasket, there are only so many paths available, even for a continuous system. This is what is meant by connectivity in the context of this thesis.

Equivalently one can use the ramification number, which refers to the number of bonds one has to remove to separate a subset of the fractal. Notice that one can always separate a third of the Sierpinski Gasket by cutting two bonds, even in a

continuous realization of the fractal. The Sierpinski Gasket, thereby, has an intrinsically low connectivity that does not disappear in a continuous system. In the Sierpinski Carpet, on the other hand, the number of bonds one would have to cut is infinite. Low connectivity corresponds to a finite, low ramification number and high connectivity corresponds to a high or infinite ramification number.

Other quantifications of connectivity can be used. By viewing the sites in the lattice as vertices, and the couplings between them as edges, one can interpret the fractals as complex networks. The clustering coefficient from complex networks might then be used to quantify the connectivity of the fractal. One can also consider using Lacunarity, betweenness or concepts from network partition. However, as mentioned earlier, this thesis will only make some broad qualitative statements regarding connectivity, and a precise quantification is not necessary.

5 Implementation and methods of calculations

Spectral properties of multiple fractal-shaped potentials will be studied numerically. Specifically, the ground state energy, transport properties, localization of states, and energy level spacing distributions will be considered. The discretization of the Hamiltonians of the systems will be treated in this section together with a method to reduce its complexity. Furthermore, the methodology for the evaluation of the ground state energy, conductance and level spacing statistics will be given.

5.1 Expressing the eigenvalue problem

In order to evaluate the different spectral properties, one needs to assess the energy levels and wave functions of particles confined in fractal potentials. In line with the postulates of quantum mechanics given in Section 3.3, the associated energy operator, the Hamiltonian, must be expressed and evaluated. The possible states of the system will then be given by the eigenvalues and eigenstates of the Hamiltonian. The Hamiltonian can be expressed as a matrix following Section 3.4. A discrete matrix representation will be given in the following.

The general form of the Hamiltonian is shown in equation (27). In the problem to be evaluated, $\mathbf{V} : \Omega \to \mathbb{R}$ is the external fractal potential. Here, $\Omega \subset \mathbb{R}^2$ is the domain with boundary $\delta\Omega$. This potential is infinite in the forbidden areas of the fractal, and zero in the allowed areas. In reality, the potential only needs to be large enough to make a clear gap in energy between the states residing in the illegal areas and those not. However, setting it equal to infinite simplifies the calculations since the wave function becomes exactly zero in these areas. The Schrödinger equation in (26) can be written

$$(\Delta_{x,y} + V(x,y))\psi(x,y) = \lambda\psi(x,y) \to \psi(x,y) = 0 \text{ in } \Omega, \tag{63}$$

where λ is a constant. Without loss of generality, the universe is set to be the unit square $\mathcal{U} = [0,1] \times [0,1]$, containing our fractal, $\Omega \subseteq \mathcal{U}$.

In order to apply numerical approximations, the domain must be discretized into a grid, $\mathbf{G}$. To this end, $\mathcal{U}$ is split into $N_x \times N_y$ linearly spaced grid points in the x and y directions. The new coordinates are $x_i = i \cdot d_x$ and $y_j = j \cdot d_y$, where d_x and d_y are the step sizes $1/(N_x + 1)$ and $1/(N_y + 1)$ respectively. The notation $\psi(x_i, y_j) = \psi_{i,j}$ will be used.

Since the differential equation does not include any mixed derivatives, the compact three-point stencil is chosen to approximate the Laplacian in (63). The formula for the two-dimensional, second-order three-point stencil is given in (16). Next, the fractal potential $V(x, y)$ is placed on the grid, giving a matrix representation of the potential $V_{i,j}$. As discussed in Section 4, the grid resolution and the lattice type should be compatible with the fractal to avoid aliasing. Equation (63) at site $\{i, j\}$ becomes

$$\left(\frac{\psi_{i+1,j} - 2\psi_{i,j} + \psi_{i-1,j}}{d_x^2} + \frac{\psi_{i,j+1} - 2\psi_{i,j} + \psi_{i,j-1}}{d_y^2}\right) + V_{i,j} \cdot \psi_{i,j} = \lambda\psi_{i,j}, \tag{64}$$

which holds for all $i, j \in G$. This matrix formulation is in line with the theory of Section 3.4 and (31), using the grid nodes as the basis set of expansion. In this thesis, the boundary conditions used will be Dirichlet as described in the discussion of (21). For $i, j \notin \mathbf{G}$, the amplitudes $\psi_{i,j} = 0$. Expressing the Laplacian using the Kronecker sum, as in (20), yields

$$(\Delta_x \otimes \mathbb{1} + \mathbb{1} \otimes \Delta_y + V_{i,j}) \cdot \psi_{i,j} = \lambda\psi_{i,j}. \tag{65}$$

The system of equations is collected into a matrix equation on the form

$$A\psi = \lambda\psi.$$

The eigenvalue has non-trivial solutions when

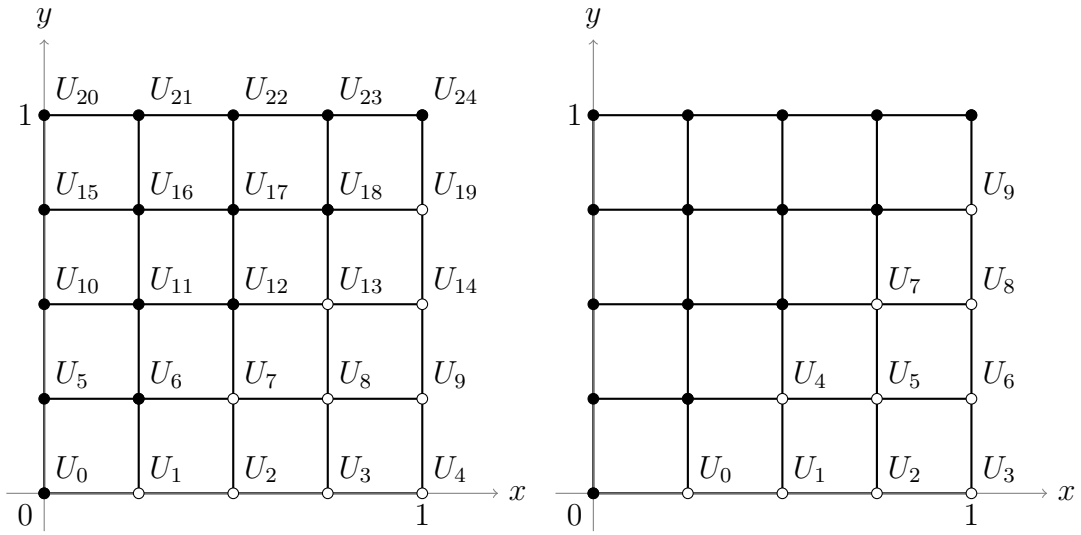
$$||A - \lambda \cdot \mathbb{1}|| = 0.$$

5.2 Equivalence of enumeration

In Section 3.1 an enumeration of the grid sites $I : \mathbf{G} \to \mathbb{N}_0$ was suggested. The suggested enumeration was the natural numbering of the grid, namely $I_n(i, j) = i + j \cdot (N_x + 1)$. However, other enumerations conserving $\psi_{i,j} = \psi_{I(i,j)}$ can also be constructed. Specifically, define an enumeration numbering only interior points of the boundary, $I_d(i, j)$. That is, the enumeration only includes the sites that lie in the allowed regions of the fractals, where the potential $V_{i,j}$ is zero. Name this enumeration the *interior indexing*. Both enumerations are visualized in Figure 16.

Equivalence of enumeration

One can choose enumeration freely without changing the obtained eigenvalues. Changing enumeration corresponds to a change of coordinate matrix P. For a permutation matrix P, an eigenvalue of A is shared with PAP^{-1}. If P interchanges



(a) Natural indexing $I_n(i,j)$ (b) Interior indexing $I_d(i,j)$

Figure 16: Grid of size 4×4. Black lattice points are exterior points and white interior. Different enumerations can be chosen. (a) Natural indexing starting from the lower left. A total of 24 points are included. (b) Interior indexing starting from the lower left. Only interior points are included, yielding a total of 9 points.

rows of the matrix, then the following inverse permutation interchange the corresponding columns. It is however not necessary that P only interchange rows. The proof that this does not alter the eigenvalues can be seen as follows.

Assume we have $Ax^n = \lambda x^n$, where the superscript n refers to the natural indexing. Superscripts are used to avoid confusion with the lattice point index j. Furthermore, let P be the matrix that projects a vector from natural indexing, x^n, to interior indexing, x^d. That is, $x^d = Px^n$. If x^n is an eigenvector of A with eigenvalue λ, then

$$PAP^{-1}x^d = PAx^n = \lambda Px^n = \lambda x^d.$$

Furthermore, let A be the matrix attained from using I_n, and $\tilde{A}$ be the matrix attained from I_d. There exists a permutation matrix P yielding $x^d = Px^n$. This change of coordinate matrix can be picked to form

$$PAP^{-1} = \begin{bmatrix} \tilde{A} & B \\ \mathbf{0} & \tilde{V} \end{bmatrix}. \tag{66}$$

If λ is an eigenvalue of $\tilde{A}$, then it is also an eigenvalue of PAP^{-1}, since if $\tilde{A}u = \lambda u$, then

$$\begin{bmatrix} \tilde{A} & B \\ \mathbf{0} & \tilde{V} \end{bmatrix} \begin{bmatrix} u \\ \mathbf{0} \end{bmatrix} = \begin{bmatrix} \tilde{A}u \\ \mathbf{0} \end{bmatrix} = \lambda \begin{bmatrix} u \\ \mathbf{0} \end{bmatrix}.$$

Therefore, λ is an eigenvalue of PAP^{-1}. Hence, this coordinate change invariance property of eigenvalues shows that an eigenvalue of $\tilde{A}$ is also an eigenvalue of A.

5.3 A reduced method for representation of the eigenvalue problem

By changing the indexing of the grid from the natural indexing in Section 5.2 to the interior indexing, one can significantly reduce the complexity of the systems Hamiltonian. As was shown in Section 5.2, this will not change the eigenvalues of the problem. This method first changing the indexing before solving for the eigenvalues will be referred to as the reduced method,

In this project thesis, we consider systems with a confining potential that is assumed to be infinite (large). The wavefunctions will have no amplitude on the exterior grid sites, as this would lead to infinite (large) eigenvalues. Therefore, the couplings between internal points and external points in the Hamiltonian can be set to zero, without any effect on the eigenstates of interest. Furthermore, the coupling between external points can also be set to zero. Thus, we obtain a system where only the interior points are of interest. This is equivalent to the interior indexing $I_d(i,j)$ and $\tilde{A}$ in Section 5.2, and the systems Hamiltonians can be written on the form of the right-hand side of (66). In addition, the columns and rows corresponding to a site in the forbidden region, $\tilde{V}$, can simply be removed. The removal of these rows is analogous to the before-mentioned transformation. In order to recover eigenvectors of the original Hamiltonian, the inverse transformation must be applied to the obtained result.

For a universe discretized into $N \times N$ points, the matrix representation of the Hamilton operator on the left-hand side of (65) with a natural indexing has $N^2 \times N^2$ elements. This is per the discussion in Section 3.1. However, using the interior indexing, $I_d(i,j)$, gives a new discretization with $\tilde{N}^2 \times \tilde{N}^2$ points. Clearly, $\tilde{N} \leq N$, where the equality holds for a fractal boundary given by the empty set. Generally, $\tilde{N}$ depends on the shape of the confining potential which separates interior and exterior points and will vary for different fractals. In the case of large forbidden areas, it will be significantly smaller than N. In such cases, using the reduced method leads to a dramatic improvement in performance times for numerical calculations. This method proved essential for the study of fractals in this thesis, and the impact on performance is discussed in further detail in Appendix A.2.

Note that the reduced method is only valid as described above when the exterior areas have a finite width. That is, there's a neighborhood around an exterior point that consists of other exterior points. If the potential is localized to a point or a line of no width, the wavefunction could be zero at that point but have a positive amplitude on one side and a negative on the other. That is, sites on either side of an infinitely thin barrier can have indirect coupling to each other, even if the potential is infinite. In such cases, removing the coupling terms through the illegal area would be unphysical. This is for example the case between triangles in the Sierpinski Gasket, shown in Figure 14. The method can still be used, it is just important to make sure that the indirect coupling through illegal areas is preserved.

5.4 Scaling of the ground state energy for increasing fractal iteration

The goal of this section is to develop tools to study the energy ground states as the fractal iteration l approaches infinity. Furthermore, it is desirable to consider continuous systems, that is, with infinite grid resolution, $n \to \infty$. The first step will be to determine the ground state energy for a fixed value of l, letting n approach infinity and extrapolating a result. Next, this will be done for different values of l, extrapolating the result as l approaches infinity.

Obtaining the ground state at fixed iteration

Consider finding the ground state energy of a fractal at fixed iteration l as the grid resolution approaches infinity, Consider first a grid resolution of $N \times N$, where N is an integer. As the resolution is gradually increased, it is expected that the eigenvalue approaches the exact energy level. Specifically, as the resolution is increased, it is expected that the error ϵ goes as $\epsilon(d) \propto d^2$, where d is the stepsize used in the grid. This is based on the error term of the three-point compact stencil for second derivatives in (15). Using a box of physical extent $L = 1$ gives $\epsilon(d) \propto d^2 = (1+N)^{-2}$, and $\epsilon(d) = \epsilon(N)$, where N is the linear grid resolution[4].

To estimate the asymptotic value of the energy as $N \to \infty$, the energy is plotted against $1/N$. The limit $N \to \infty$ then corresponds to $1/N = 0$ and the expected error convergence goes as $\epsilon(1/N) \propto (1+1/N)^{-2}$. Next, fit functions to the obtained points, using both linear and quadric fits. Call these fits $\tilde{E}_1(\frac{1}{N})$ and $\tilde{E}_2(\frac{1}{N})$ respectively. The value of $E(N = \infty)$ can be estimated as $\tilde{E}_{1,2}(\frac{1}{N} = 0)$. That is, as the intersection between the energy axis and either of the fitted functions. This provides a method for extrapolating the ground state of the system.

In general, for a given fractal at fractal iteration l, only certain grid resolutions are compatible with the shape of the fractal. These resolutions are given in Tables 1, 2, 3 and 4 for the Sierpinski Carpet, Sierpinski Square, Sierpinski Gasket and Flag-fractal, respectively. In order to compare the results from different fractals, the linear length scale resolution n as introduced in Section 4.1 is used instead of the linear resolution N.

Energy scaling for increasing fractal iteration

Having found a method to extrapolate the ground state energy at infinite grid resolution n in the previous section, we now need tools to study the ground state energy for increasing fractal iteration l. For these highly self-similar fractals, each iteration $l' + 1$ consists of m copies of iteration l' where each linear side has been rescaled by a factor $1/r$, as described in Section 2.2.

[4]This is true as long as the used resolution does not lead to stepsizes d in (64) that approach machine precision ϵ_{mach}. This will rapidly lead to inaccurate results.

Consider a simple box whose edges decrease by a factor of $1/r$ for each fractal iteration l. In units of $\hbar^2/m$, one would expect the energy at a given iteration to be $E_l = \frac{\pi^2}{A_0} \cdot r^{2l} = E_0 \cdot r^{2l}$. That is, the energy follows a power law given by r^{2l}. This is the expected result for any Euclidean, two-dimensional system. The equivalent result for a one-dimensional system is $E_l = E_0 \cdot r^{1l}$, and for a three-dimensional system it is $E_l = E_0 \cdot r^{3l}$. It is however not trivial to determine the expected result for a fractal-dimensional system.

Define the energy ratios of the ground states s_l such that $s_l = E_l/E_{l-1}$. Furthermore, define the energy scaling factor s as

$$s = \lim_{l\to\infty} s_l = \lim_{l\to\infty} E_l/E_{l-1}. \tag{67}$$

That is, s is the energy scaling between consecutive fractal iterations, in the limit of large fractal iterations, assuming this converges. In the case of the box, $s_l = s = r^2 \ \forall \ l$. However, this will not necessarily be the case for other objects, which is why it is good to separate the quantities. In the proceeding calculations, r is named the fractal rescaling factor and is considered known. On the other hand, the energy ratios s_l and the energy scaling factor s need to be measured numerically.

Generally, the ground state energy of a confined particle with no other external potential is inversely proportional to the area in which the wave function resides. The rate at which these changes is equivalently captured by the change in energy, and therefore s_l. It is suggested that these scaling factors might go as $s = r^{D_H}$ for fractals, where D_H is the Hausdorff dimension of the fractal. This is motivated by the fact that the Hausdorff dimension describes the scaling properties of measures such as the area of the fractals.

5.5 Current and conductance

The wave function formalism for the calculation of transport through a potential was given in Section 3.5. In the following, a discretization of the equations from this section will be discussed, remaining in the one-dimensional system. This is largely based on Datta (1995), where an extension to higher dimensions is also demonstrated. The potential itself will be discretized as discussed in Sections 5.1−5.3, using the reduced method.

Discretization of the system

In order to perform numerical calculations, the system needs to be discretized. Divide the scattering region in Figure 8 into N equally-spaced points with a spacing d. Replace the continuous variable x by $x_j \equiv j \cdot d_x$, as depicted in Figure 17. Furthermore, let $\psi(x) \to \psi(x_j) \equiv \psi_j$ and equivalently $V(x) \to V(x_j) \equiv V_j$. The potential is greater than zero in the interval $[1, N]$, where the index $j = 0$ is purposely excluded as this will simplify later equations. Approximate the Laplacian in the Schrödinger equation using the three-point stencil in one dimension, given by (15). Next, absorb all the appearing constants into one, writing $\tilde{t} = \hbar^2/2md_x^2$. This yields the

discretized Schrödinger equation

$$-\tilde{t} \cdot \psi_{j-1} + (V_j + 2\tilde{t})\psi_j - \tilde{t} \cdot \psi_{j+1} = E\psi_j. \tag{68}$$

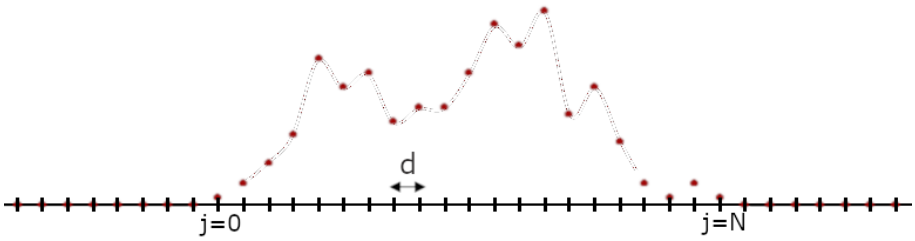


Figure 17: The scattering process depicted in Figure 8 is discretized. The first site with potential greater than zero is labeled by index $i = 0$, and the last site is labeled $i = N$.

The Schrödinger equation in (68) describes a tight-binding model. Usually, the potential is redefined such that $V_j + 2\tilde{t} \to V_j$, while maintaining that the potential should be zero outside the scattering region. Naturally, adding or subtracting along the diagonal only leads to a constant shift in the energy eigenvalues. Making this redefinition of V_j gives symmetry around $E = 0$. This redefinition will be applied in the transport calculations considered in this thesis.

The wave functions in the leads were given by (33) and (34) for the continuous system. In the discretized system, the wave function in the left-hand lead becomes $\psi_j^L = e^{ikx_j} + re^{-ikx_j} = e^{ik\cdot jd_x} + re^{-ik\cdot jd_x}$. Equivalently, the wave function in the right-hand lead becomes $\psi_j^R = te^{ikx_j} = te^{ik\cdot jd_x}$. It is important to note that while the dispersion relation in the leads in the continuous case was given by (35), the dispersion relation in this discretized system is given by

$$E_j(k) = -2\cos(k \cdot d_x), \tag{69}$$

in the units of $\tilde{t}$, where the subscript j is added to distinguish this from the continuous case. This can be found by inserting the expression for, for example, the wave function in the right-hand lead into the discretized Schrödinger equation in (68). Next, make use of Euler's formula, writing $e^{i\theta} + e^{-i\theta} = 2\cos(\theta)$, to obtain (69). The continuous dispersion relation in 35 is recovered in the continuous limit of (69), taking $d_x \to 0$ and Taylor expanding the cosine.

Boundary layers

Having formulated the discrete wave equation in (68), the system can now be solved numerically. The dispersion relation for the leads was given in (69). Now match the wave functions at the transitions between the leads and the scattering region, and apply the discrete Schrödinger equation in (68) to the sites inside the Scattering region. This is equivalent to (36) in the continuous system. The matching yields

the linear set of equations given by

$$\begin{aligned}
\text{W.F. at } j=1 &: re^{-ikd} - \psi_1 = -e^{ikd}, \\
\text{S.E. at } j=1 &: r + (E - V_1)\psi_1 + \psi_2 = -1, \\
\text{S.E. at } j \in [2, N-1] &: \psi_{j-1} + (E - V_j)\psi_j + \psi_{j+1} = 0, \\
\text{S.E. at } j=N &: \psi_{N-1} + (E - V_N)\psi_N + te^{ik(N+1)d} = 0, \\
\text{W.F. at } j=N &: \psi_N - te^{ikNd} = 0.
\end{aligned}$$

This can be expressed in matrix form as

$$\begin{bmatrix}
e^{-ikd} & -1 & 0 & \dots & \dots & \dots \\
1 & E-V_0 & 1 & 0 & \dots & \dots \\
0 & 1 & E-V_1 & 1 & 0 & \dots \\
\dots & \dots & \dots & \dots & \dots & \dots \\
\dots & \dots & 0 & 1 & E-V_N & e^{ik(N+1)d} \\
\dots & \dots & \dots & 0 & 1 & -e^{ikNd}
\end{bmatrix}
\begin{pmatrix} r \\ \psi_1 \\ \psi_2 \\ \dots \\ \psi_N \\ t \end{pmatrix}
=
\begin{pmatrix} -e^{ikd} \\ -1 \\ 0 \\ \dots \\ 0 \\ 0 \end{pmatrix}. \tag{70}$$

The system is then solved for the wave function. The wave function vector in (70) is expressed by the set $\{\psi_j\}$ together with r and t, giving the amplitudes at every discrete point inside the scattering region as well as the leads. This is then set equal to the injected wave function on the right-hand side of (70). The solutions for r and t, as well as the solutions for the reverse process, r' and t', form the scattering matrix as given in (37).

Pay notice to the distinction between the transmittance amplitude t and the constant $\tilde{t}$. In literature, both are frequently referred to by simply "t", but the tilde is added here for readability. The system specific constant $\tilde{t}$ is also referred to as the hopping amplitude as it corresponds to the matrix element coupling two neighboring sites. In this thesis, the hopping amplitude is simply constant but that is not always the case.

Current and conductance

The particle current in (38) can be written in the discrete representation. Substitute the derivatives in (38) by using the two-point forward method from (13) yielding

$$J_j = \frac{\hbar}{2mi}\left[\psi_j^*\psi_{j+1} - \psi_j\psi_{j+1}^*\right]. \tag{71}$$

For the transmitted plane wave in the right-hand lead, the wave function is given as $\psi_j^R = te^{ik\cdot jd_x}$. The current density in (71) in units of $\tilde{t} = \hbar^2/(2md_x^2)$ then becomes

$$J_j^R = \frac{|t|^2}{\hbar}\frac{d_x}{i}\left[e^{ik\cdot d_x} - e^{-ik\cdot d_x}\right] = \frac{|t|^2}{\hbar}2d_x\sin(k\cdot d_x), \tag{72}$$

where we've made use of Euler's equation in the final equality. The subscript j is kept to distinguish this from that found in (39) for the continuous case. Tracing the path of the discussion of the continuous system in Section 3.5, next, consider the velocity $\hbar v(k) \equiv \frac{\partial}{\partial k}E(k)$. Insert the dispersion relation for the tight-binding

model in (69) into this expression and add a subscript j to distinguish it from the continuous case. The velocity then becomes $\hbar v_j(k) = 2d_x \sin(kd_x)$. Use this to rewrite (72) giving

$$\begin{aligned} J_j^R &= |t|^2 v_j(k), \text{ with} \\ v_j(k) &\equiv \frac{1}{\hbar}\frac{\partial}{\partial k} E_j(k), \end{aligned} \tag{73}$$

still in units of $\tilde{t}$. On the other hand, for the scattered wave in the left-hand lead with wave function $\psi_j^L = e^{ikj} + re^{-ikj}$, (71) becomes

$$J_j^L = \left(1 - |r|^2\right) v_j(k). \tag{74}$$

Once again, conservation of current implies then that $1-|r|^2 = |t|^2 = |t'|^2 = 1-|r'|^2$. This makes the scattering matrix unitary, $SS^\dagger = 1$, as discussed in Section 3.5.

Notice that (73) and (74) have the same form as (40) and (41) in the continuous case. Inserting the discrete expressions for J^L and J^R into, for example, the expression for the real current in (43) yields the exact same results as was found in (44). All the remaining equations from Section 3.5 are equal in the discrete and the continuous case. The equation for the conductance found in (49) can be used to evaluate the conductance in the discrete system, namely

$$g(E_F) = 2e^2/h \cdot |t(E_F)|^2 = 2g_0 |t(E_F)|^2.$$

When evaluating the conductance one needs to first solve for the wave function in (70) and then insert the tunneling elements into (49). The implementation of this is done with the help of the open-source Python package Kwant [Groth et al. (2014)].

5.6 Level spacing statistics

As discussed in Section, 3.6, the energy level spacing statistics can yield information about the symmetries and periodicity of the system. However, in order to recover meaningful results, some important steps must be included. In this section, some details of the procedure are given, followed by a numerical example that demonstrates the method for two random matrices.

Details of the evaluation of level spacing statistics

There are a couple of important steps in the evaluation of level spacing statistics necessary to obtain sensible results that should be compared. First of all, the energy levels are sorted and the level spacings are found as the differences between consecutive energy levels. When evaluating numerical or experimental data, degenerate states are expected to be observed at slightly different energies. It is therefore important to set a sensible minimum value for the energy level spacing ΔE. Energy level spacings smaller than this minimum value are considered exactly zero and should not be included in the level spacing statistics.

Furthermore, one should apply a normalization procedure to the energy level spacings such that the mean level spacing becomes equal to 1. This normalization is frequently referred to as the *unfolding* of the level spacings. The unfolding procedure is essential for comparing the level spacing distributions of different systems because it removes system-specific features such as the overall energy scale and the density of states. This allows direct comparison of the underlying statistical properties of different systems. To do this, the energy levels are rescaled by a smooth function that represents the mean density of states in the following way.

For the sake of this discussion only, denote the original energy levels as E_n and the unfolded energy levels as e_n. Next, define $N(E)$ as the integrated or cumulative density of states, that is, the number of states with energy less than or equal to E. One can unfold the level spacings by writing the unfolded energies as

$$e_n = N(E_n). \tag{75}$$

The unfolded level spacings are then given by $\Delta e_n = e_{n+1} - e_n = N(E_{n+1}) - N(E_n)$. Naturally, when letting E_n and E_{n+1} be the energies of two consecutive states, the expectation value of the difference $\Delta e_n = N(E_{n+1}) - N(E_n)$ must equal 1. The unfolded level spacings will be referred to simply as ΔE throughout the rest of the thesis. In practice, finding a suitable function $N(E)$ can be difficult because it requires a good estimate of the mean density of states. In this thesis, $N(E)$ will be found numerically and a smooth curve will then be fitted to the numerical results and used in the unfolding in (75). Specifically, an optimized spline method will be used as a fit.

All energies with ΔE greater than the aforementioned minimum value are unfolded and distributed into a histogram. The obtained histogram should be considered a density and is therefore normalized to have a total area equal to 1. This concludes the preparation of the data, and this distribution is the one used in the level spacing statistics. The distribution can be compared with the theoretical predictions from random matrix theory, such as the Wigner-Dyson distribution in (53) or the Poisson distribution in (54).

To verify the method and become more acquainted with the procedure, an example is included in the following.

Example of level spacing distributions

Consider the Wigner-Dyson distribution in (53). As discussed in Section 3.6, different values of the exponent β are associated with the three main classes of random matrices. The main classes are the GOE, the GUE and the GSE. The exponent β can be measured from numerical or experimental data of the energy level spacings to classify systems into one of the three groups. By doing so, one gains information about the symmetries of the system. Such a classification is demonstrated for a random orthogonal and a random unitary matrix in Figure 18. Here, random matrices of size 20000×20000 were generated with the desired symmetries and the eigenvalues were solved by exact diagonalization. The energy levels were then sorted and the

level spacings were computed and normalized as discussed earlier in this section. Finally, fits using (50) and (51) were made. The results clearly show that the random orthogonal matrix is well described by a Wigner-Dyson distribution with exponent $\beta = 1$, and the random unitary matrix by $\beta = 2$. This is as expected from random matrix theory. A Poisson distribution is included in Figure 18 for comparison.

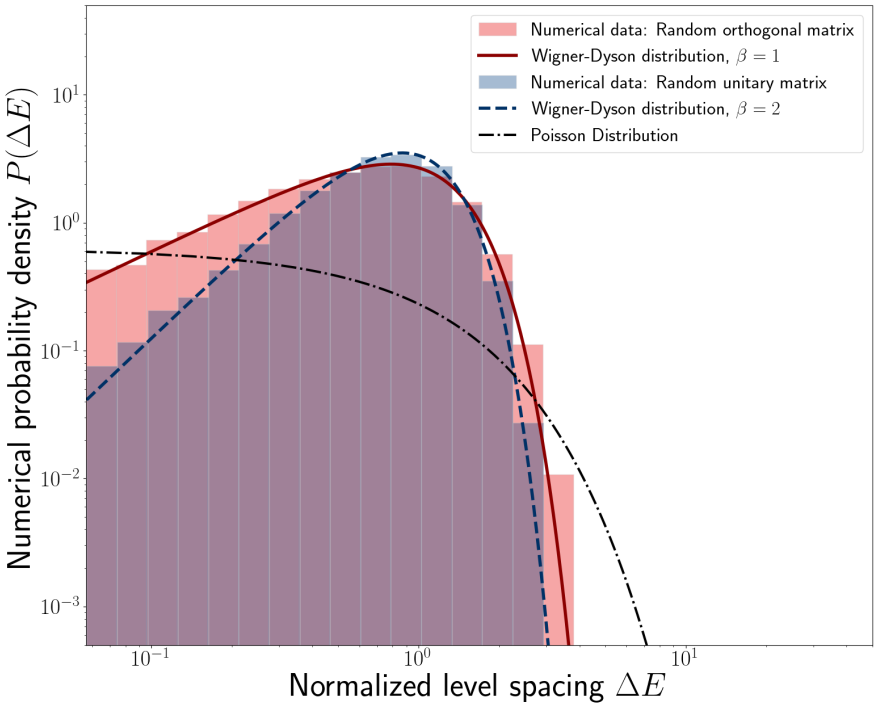


Figure 18: The level spacing distributions for random matrices with different symmetries are plotted along with the theoretically expected results on a log-log plot. In red is a histogram of the energy level spacings for a random orthogonal matrix. The histogram matches the solid red line, which reflects the Wigner-Dyson distribution with $\beta = 1$. A histogram of the energy level spacings for a random unitary matrix is shown in blue. This matches the dashed blue line which indicates a Wigner-Dyson distribution with $\beta = 2$. Finally, a Poisson distribution is included for comparison, given by the dash-dotted black line. The energy level spacings were calculated and normalized through a process known as unfolding to get comparable results.

6 Scaling of the ground state energy for increasing fractal iteration

Methods for generating fractals were discussed together with their properties in Section 4 and Appendix B. The formulation of a discrete Hamiltonian from these fractals was discussed in Sections 5.1−5.3. Furthermore, a method for evaluating the ground state energy when approaching infinite fractal iteration $l \to \infty$ was discussed in Section 5.4. With this background, the first spectral property of the fractals will be studied, namely the scaling of the ground state energy with increasing fractal iteration. The method will first be applied in detail to the Sierpinski Carpet,

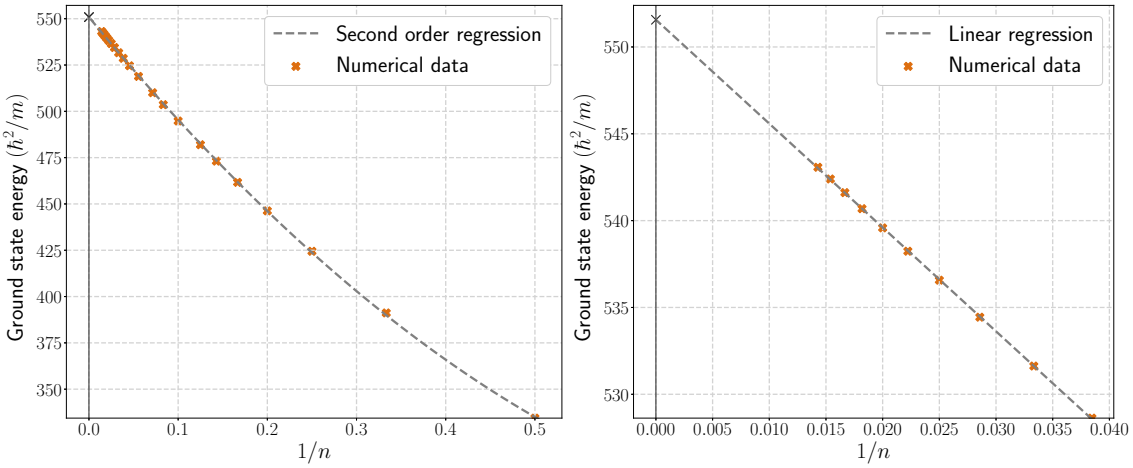
together with a brief discussion of the ground state wave functions of this fractal. Thereafter, the scalings of the ground state energies of other fractals are considered. These results and parts of the discussion were first introduced by Akre (2023).

6.1 Ground state of the Sierpinski Carpet

The probability densities and energy levels of the Sierpinski Carpet are computed for different fractal iterations. Following Section 5.4, the system is first evaluated at a fixed fractal iteration l. Next, the scaling of the ground state energy between fractal iterations will be considered.

The ground state energy at fixed fractal iteration

The groundstate energy at a given fractal iteration l is estimated by varying the grid resolution according to the method described in 5.4. A quadric fit of the Sierpinski Carpet at fractal iteration $l = 3$ is shown in Figure 19a. In Figure 19b only the last ten points are included and a linear fit is utilized. The energy is found from the intersection of the energy axis in units of $\hbar^2/m$ and was estimated to be $\tilde{E}_2(0) = 551.80$ and $\tilde{E}_1(0) = 551.78$, using the second-order and linear fit respectively. Only data points for large grid resolutions are used in the linear extrapolation since the convergence in $1/n$ is only approximately linear when the grid resolution is large. When large linear length scale resolutions n are used, these two fits give approximately the same extrapolated value. The agreement of the two fits serves as a test to see whether the resolution is sufficiently large and shows why both a linear and a quadric fit are considered. The extrapolated value from the second-order regression has been seen to converge faster than the one from the linear regression. Therefore, the extrapolated energy obtained from the second-order interpolation, $\tilde{E}_2(0)$, will be used in calculations. The linear fit is kept as a control to ensure that the system is evaluated at sufficiently high resolutions. Going to third-order regression yields results very similar to that of the second-order. The estimates of the ground state become less accurate for higher fractal iterations as it becomes more difficult to evaluate high resolutions.



(a) Second-order fit (b) Linear fit

Figure 19: The ground state energy of the Sierpinski Carpet at fractal iteration $l = 3$ plotted against the inverse linear length scale resolution $1/n$. An estimate for the ground state energy in the continuous system is obtained from evaluating the fitted functions at $1/n = 0$. In (a), a second-order regression $\tilde{E}_2(\frac{1}{n})$ is used over a large range of resolution values. In (b), a linear regression $\tilde{E}_1(\frac{1}{n})$ of the 10 largest resolutions is shown.

The ground state at different fractal iterations

The process is repeated for different values of the fractal iteration l. The results up to $l = 7$ are shown in a log-log plot in Figure 20 and given in Table 5. The slope of the logarithmic energies in Figure 20 is seen to become linear for large l, indicating an exponential dependence.

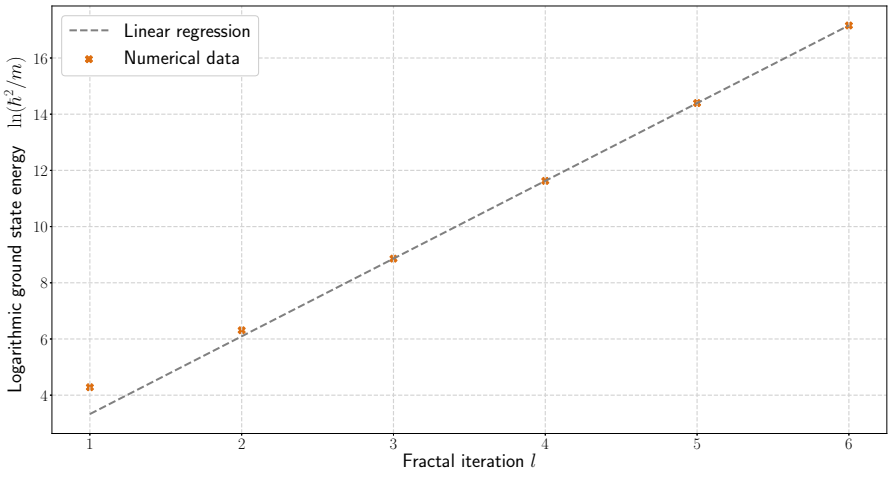


Figure 20: The natural logarithm of the ground state energy of the Sierpinski Carpet for increasing values of the fractal iteration l. The slope of the logarithmic energies is seen to approach a linear function, corresponding to an exponential dependence of the ground state energy with respect to l.

From Table 5, it is seen that, although the deviations between the linear and second-order fits become larger for increasing fractal iterations, the deviations remain an acceptable size.

Table 5: The extrapolated ground state energy of the Sierpinski Carpet for increasing fractal iteration. For each fractal iteration, the largest linear length scale resolution n used is also shown. Both second-order and linear intersects are shown. The two deviate more for higher fractal iterations when it is not possible to sample with as high resolutions compared to the system's detail.

l	Largest n-value used	Linear intersect $\left(\frac{\hbar^2}{m}\right)$	Second order intersect $\left(\frac{\hbar^2}{m}\right)$	Deviance $(\frac{2nd-1st}{2nd\ order})$ (%)
1	110	38.72	38.73	0.043
2	90	114.11	114.13	0.023
3	70	551.78	551.80	0.003
4	28	4566.23	4569.79	0.078
5	19	40 654.59	40 783.20	0.315
6	14	363 899.01	365 833.40	0.529
7	7	3 242 052.89	3 280 895.88	1.184

Finally, consider the probability density of the ground state at different fractal iterations. To obtain this, the absolute squares of the eigenvectors are taken. Furthermore, the Sierpinski Carpet is symmetric under a 90° rotation and exhibits 4-fold symmetry. The corresponding ground state wave function therefore also exhibits this symmetry. Because of this, the first four densities are summed and normalized. The probability densities of the ground states for the first six fractal iterations for the Sierpinski Carpet are shown in Figure 21.

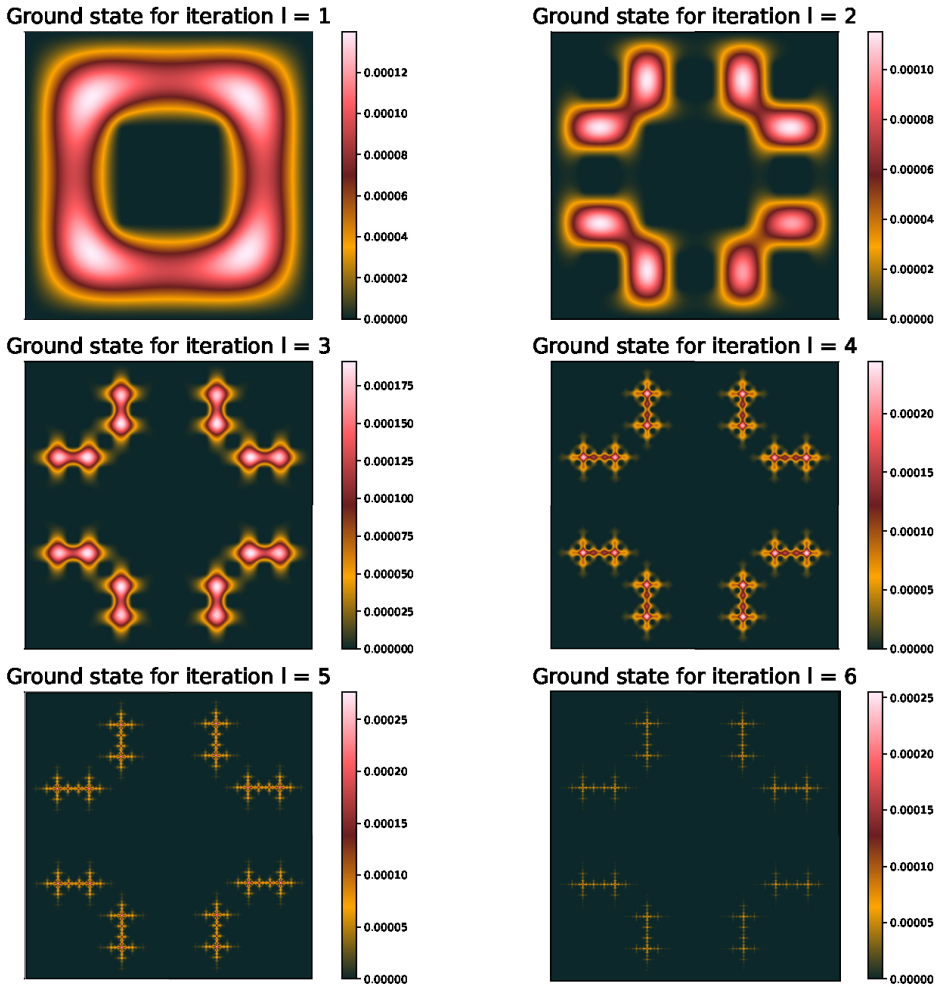


Figure 21: Probability densities of the ground state of the Sierpinski Carpet for the first few fractal iterations. A four-fold symmetry is evident.

Scaling of the ground state energy for increasing fractal iteration

Consider next the ratios between the ground state energies of subsequent fractal iterations s_l as discussed in Section 5.4. The obtained values are given in Table 6. The ratios s_l are not equal for each fractal iteration l like they were in the case for the particle in the two-dimensional box in Section 5.4. It is seen that as the fractal iteration l increases, the energy ratios s_l approach the value 9 in a seemingly asymptotic manner. Looking at the definition of the energy scaling factor s in (67), these results indicate that $s = 9$. Had there been a relation to the Hausdorff dimension $s = r^{D_H \cdot l}$ as suggested in Section 5.4, one would expect $s = r^{D_H} = 8$, but this is clearly not the case. Instead, the obtained result corresponds to $s = r^2 = r^{D_L}$, where D_L is the topological dimension or Lebesgue dimension of the fractals as described in Section 2.2. That is, the energy scaling for the Sierpinski Carpet corresponds to that of a regular two-dimensional system.

Table 6: Ratios between ground state energies of consecutive fractal iterations s_l for the Sierpinski Carpet. The individual energies can be found in Table 5.

l	$s_l = E_l/E_{l-1}$
2	2.9
3	4.8
4	8.3
5	8.9
6	9.0

The precision of the results for fractal iteration $l = 7$ was deemed too inaccurate to include in Table 5. This is because the interval of grid resolutions n considered for $l = 7$ was deemed too small, which could have led to errors that would have been be difficult to estimate. However, the result of $l = 7$ gave $s_l = 9$, which coincides with the other values.

6.2 Scaling of the ground state energy of other fractals

The same analysis as was done for the Sierpinski Carpet in Section 6.1 was repeated for the other fractals. The corresponding energy scaling factors s were evaluated for each fractal. The energy scaling factor describes the scaling of the ground state energy of a fractal as the fractal iteration l is increased, and it was defined in (67).

Recall that for the square considered in Section 5.4, it was found that $s = r^2$. It was also noted that for a general Euclidean object with an integral, topological dimension D_L, the expected energy scaling factor s equals r^{D_L}. The definition of the topological dimension, or Lebesgue dimension, was introduced in Section 2.2, and loosely speaking D_L is the intuitive, integer dimension of an object. For a Euclidean object, the Hausdorff dimension D_H is equal to the topological dimension and one can simply write $s = r^{D_L} = r^{D_H} = r^D$. It is however not trivial to see how this energy scaling factor generalizes for a fractal object with a Hausdorff dimension D_H different from its topological dimension D_L.

A total of thirty-three fractals were considered and their estimated energy scaling values are shown in Figure 22, plotted against the corresponding fractals' Hausdorff dimensions. It is not observed any correspondence between the Hausdorff dimension and the energy scaling factor s in these results. Generally, the objects with higher values of s tend to have larger fractal dimensions D_H, but this might be understood from other properties of the fractals. Specifically, the fractals with larger Hausdorff dimensions, also typically rescale their constituent parts by a smaller factor, $1/r$, per fractal iteration l than those with lower Hausdorff dimensions. The area where the wavefunction resides is expected to get squeezed more dramatically per fractal iteration l when $1/r$ is small. This is expected to yield a greater energy scaling factor s.

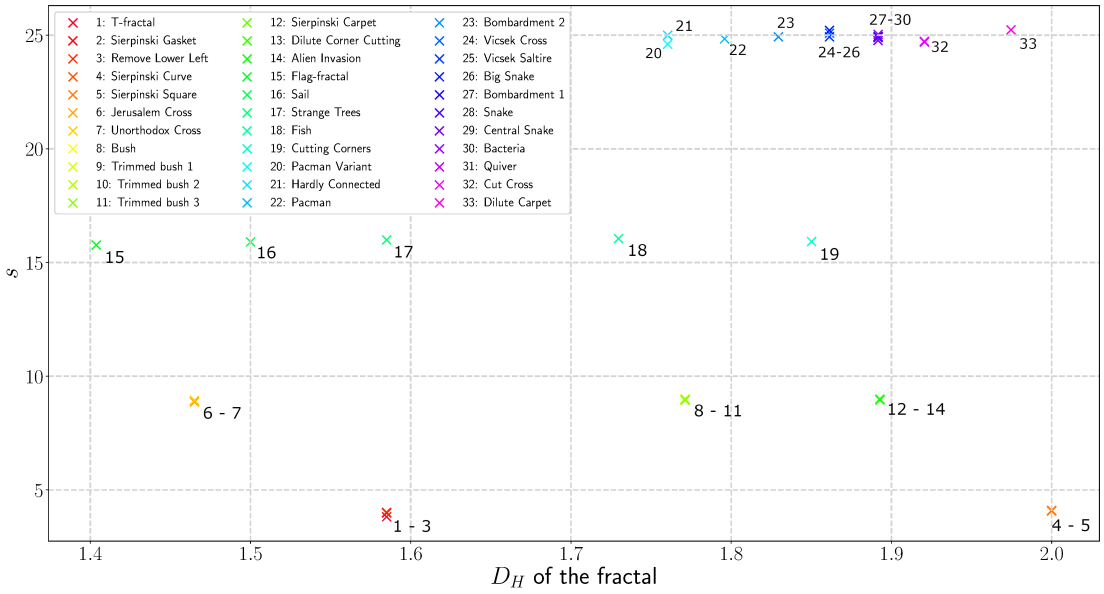


Figure 22: The scaling factors of the ground state energies s of different fractals are plotted against the Hausdorff dimensions D_H of the fractals. There is no observed correspondence between the scaling factors and the Hausdorff dimensions of the fractals.

It was seen in the case of the Sierpinski Carpet that $s = r^2 = r^{D_L}$. The other considered fractals also have $D_L = 2$. Motivated by this, the energy scaling factor s is plotted against the square of the fractal rescaling factor, r^2, in Figure 23. A dotted line corresponding to $s = r^2$ is included in the plot.

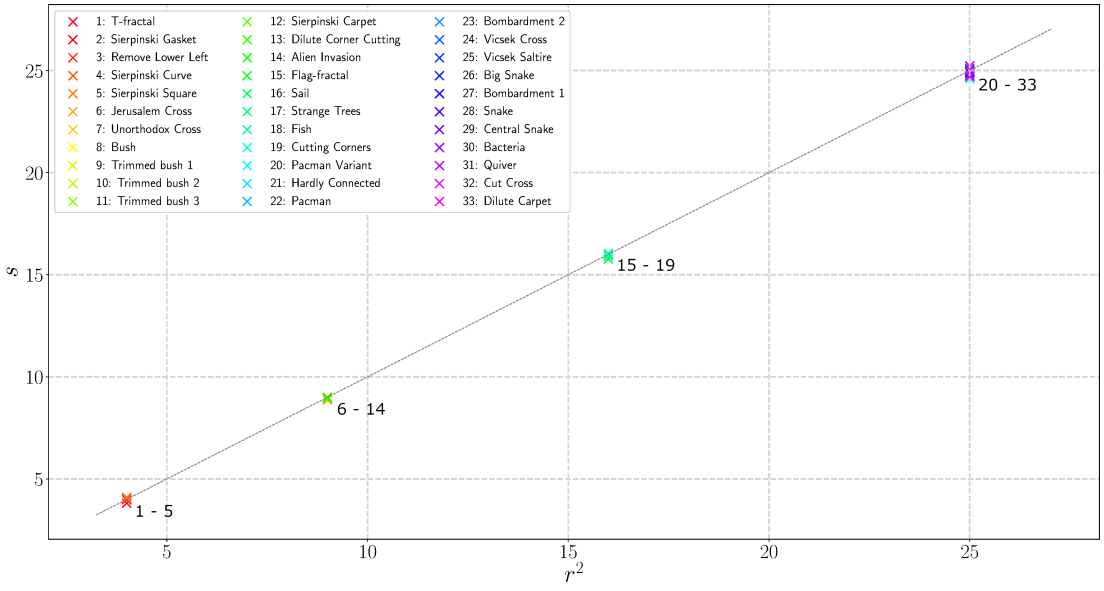


Figure 23: The energy scaling factors s for different fractals are plotted against the square of the linear rescaling factor r^2. The dotted line correspondences to $s = r^2$.

The results seen in Figure 23 correspond to the relation

$$s = r^2 = r^{D_L}, \tag{76}$$

where D_L is the topological dimension of the fractals. That is, it corresponds to the normal solution of a Euclidean object, as was the result found for the Sierpinski Carpet. To gain further confidence in this result, consider the implications of the alternative relation $s = r^{D_H}$.

An alternative energy scaling determined by the Hausdorff dimension

It has been observed that the energy scaling factor s is determined by (76). To gain further confidence in the result, consider the implications of the alternative relation $s = r^{D_H}$. The relation $s = r^{D_H}$ would imply a strong correspondence between s and the number of copies m. The number of copies m was introduced in Section 2.2 and gives how many copies of the fractal at iteration $l' - 1$ are found in the fractal at l'. For perfectly self-similar fractals, which satisfy the open set condition given in (7), one has $D_H = D_S = \log(m)/\log(r)$. Here, D_S is the similarity dimension from (6) and r is the linear rescaling factor. This would then yield the relation

$$r^{D_H} = r^{D_S} = r^{\frac{\log(m)}{\log(r)}} = m.$$

The energy scaling factor s is plotted against the number of copies m for different fractals in Figure 24. The found values of s are seen to pile up at horizontal levels. The plot does not demonstrate the property $s = r^{D_H} = m$. It could at first glance seem that there is a correspondence between the number of copies m and the found energy scaling factors s. However, the fractals with larger values of m also typically have larger values of the fractal rescaling factor r. Thus, the trend seen in Figure 24 is attributed to this correlation between m and r, and not to a relation between s and m directly. That is, it is concluded that no relation between s and m can be extracted from Figure 24. Instead, the energy scaling factor s is determined by the linear rescaling factor r and the topological dimension D_L.

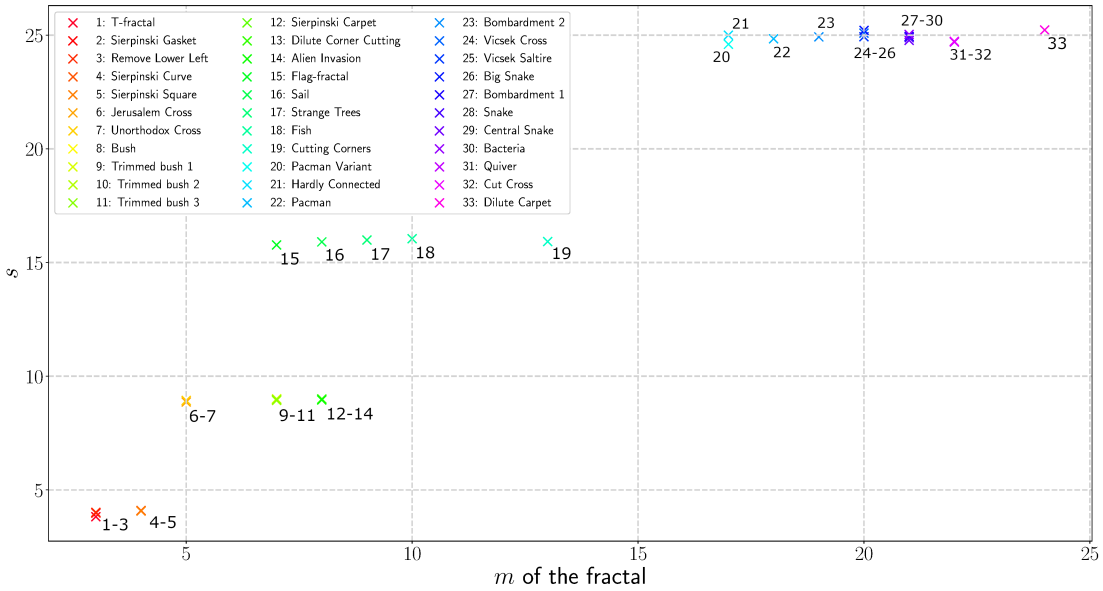


Figure 24: The energy scaling factor of the ground state s for different fractals is plotted against the number of copies m. The value m was introduced in Section 2.2, and is the number of copies of the fractal at iteration $l = l' - 1$ that can be found in the fractal at iteration $l = l'$. The number of copies m enters in the definition of the similarity dimension in (6), which is equal to the Hausdorff dimension for a perfectly self-similar object.

Impact of numerical precision

The impact of imprecise numerical calculations is included as a final remark to gain further confidence in the obtained result. It is difficult to conclude beyond any doubt that the obtained results are not influenced by numerical imprecision, but a compelling argument is given here.

Suppose that the relation $s = r^{D_L}$ is wrong and that the result was caused by insufficient numerical precision. This means that either finer grid resolutions or larger fractal iterations l, or both, would yield a different energy scaling factor s.

Consider first increasing the fractal iteration l. Based on Table 6 it is seen that the ratios between consecutive ground state energies s_l in fact become closer to the relation $s = r^{D_L}$ as l increases. It is therefore highly unlikely that considering even larger values of l would disprove the relation $\lim_{l\to\infty} s_l \to s = r^{D_L}$.

The remaining option is then to increase the grid resolution. This is done by increasing the linear length scale resolution n, which dictates the grid resolution. The easiest test is to run the numerical evaluations for lower values of n and compare the results. An example of using smaller grid resolutions in the calculations is shown in Figure 25. It is seen here that the obtained values of s for the different fractals lie lower than $s = r^{D_L} = r^2$ when n is small. In fact, it seems that when s only approaches r^{D_L} when both l and n are large. This advocates that the obtained relation for the energy scaling factor s is not due to low-precision calculation.

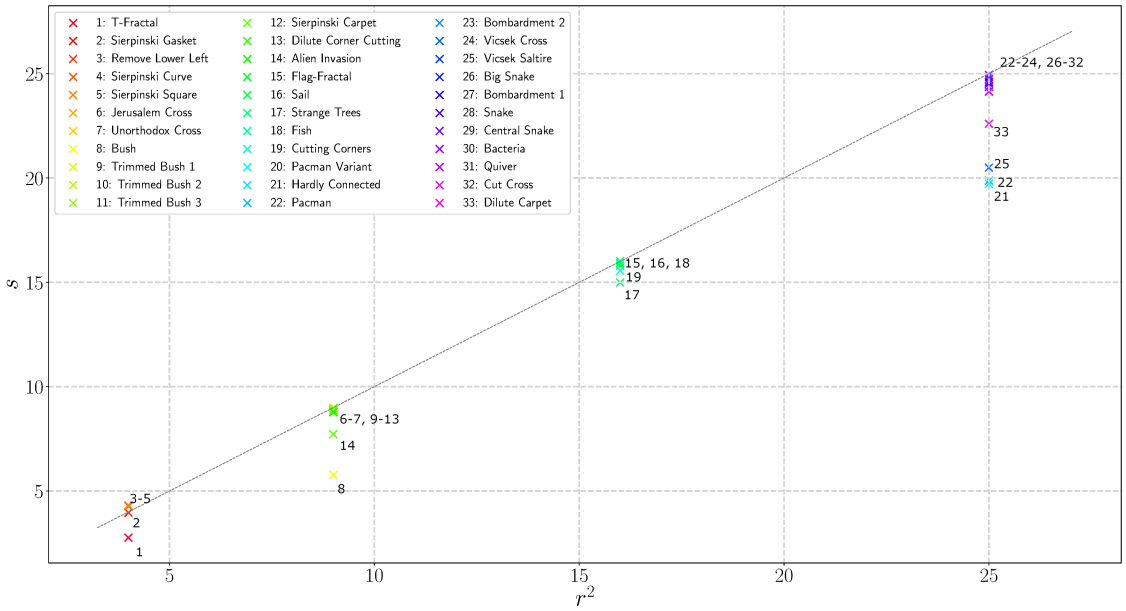


Figure 25: The energy scaling factor of the ground state s plotted against the fractals' linear rescaling factors r for lower resolutions in grid size and fractal iteration l. As the precisions in the calculations are increased, the results approach that of a regular two-dimensional object.

6.3 Interpretation of the ground state energy scaling

Consider a fractal with a Hausdorff dimension D_H and a topological dimension $D_L \neq D_H$. The analysis in Sections 6.1 and 6.2 shows that, for large values of the fractal iteration l, the ground state energies of subsequent iterations follow a power law, $E_{l+1} \approx s \cdot E_l \approx s^l \cdot E_0$. It is stressed that this only holds for large values of l. Furthermore, it was found in (76) that the energy scaling factor s is determined by the linear rescaling factor between iterations r and the topological dimension D_L as $s = r^{D_L}$. A possible explanation involves an increased localization in the ground state wave functions as the fractal iteration l increases.

Consider the different values of s_l found between fractal iterations for the Sierpinski Carpet, given in Table 6. For the intermediate values of the fractal iteration, $l = l'$, the found energy ratios were denoted $s_{l'}$. The results mean that the area in which the particle resides decreases by a factor of $1/s_{l'}$ when the fractal iteration advances from $l'-1$ to l'. For finite iterations, it was found that $s_{l'} < r^2$, and s approached r^2 for large l. Moreover, the fractal iteration l' consists of $m = 8$ copies of the fractal iteration $l'-1$, each linearly rescaled by a factor $1/r$. Since $s_{l'} < r^2$, this means that the particle must reside in more than one of these copies of $l'-1$. The wave function spreads out into neighboring copies, but not at a sufficient rate, as the area where the wave function resides still tends towards zero rapidly. This is also confirmed by inspecting the probability density in Figure 21. Here it can be confirmed that the particle spreads out to a much greater extent for the low fractal iterations.

The observed relation $\lim_{l\to\infty} s_l \to s = r^2$ for large values of l then corresponds

to the particle simply staying put in the structure of $l-1$ as the fractal iteration advances to l. In fact, in Figure 21 it is seen that the wave function resides in increasingly isolated islands as the fractal iteration grows. It does not make use of the full global structures of the fractals and therefore does not observe global properties such as the number of copies m. The plot between s and m in Figure 24 confirms that there is no observed relation between the two. In turn, this would correspond to a localized state in the limit of large l that doesn't perceive the change in the global structure. That is, the particle doesn't utilize the total available area in the fractal but is instead confined to several isolated regions.

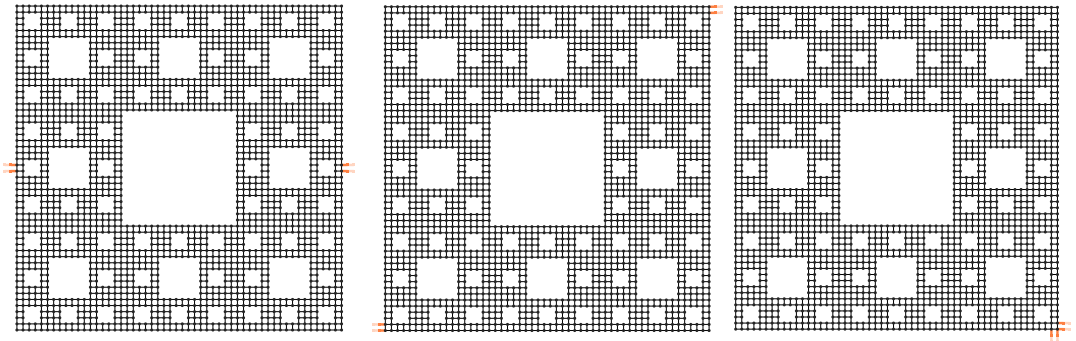
Based on this, it is theorized that as the fractal iteration l increases, the wave functions become increasingly localized to the point where they do not experience the global structures of the fractals. In this sense, they do not perceive the fractal dimensions of the confining potentials either. This leads to the obtained energy scaling factors in (76) being completely determined by the linear rescaling factors r and the topological dimensions D_L.

7 Conductance

This section carries on the research on properties of quantum particles in fractal potentials, now concentrating on transport. The conductance of a coherent electron current through a fractal potential is considered. The analysis will first be carried out for the Sierpinski Carpet and the Sierpinski Gasket. Next, the procedures are repeated for other fractals and the results are discussed. Finally, some additional considerations on multifractal analysis are made and an experimental setup is suggested. The theoretical background for the following discussion is the scattering theory of transport presented in Section 3.5. Specifics on the methodology were outlined in Section 5.5.

7.1 Conductance through the Sierpinski Carpet

In order to evaluate the transport properties through the Sierpinski Carpet, the system is discretized as discussed in Section 5.5. Next, two leads are attached to the fractal, and we're considering the transport of quantum particles between the two. Different lead positions can be used, as shown in Figure 26. The displayed lead positions will be referred to as central, diagonal and corner, respectively.



(a) Central (b) Diagonal (c) Corner

Figure 26: The discretized Sierpinski Carpet at fractal iteration $l = 3$ and linear length scale resolution $n = 2$. This setup is used for evaluating transport properties. The attached leads are indicated by orange lines. The configurations are referred to as (a) central, (b) diagonal, and (c) corner.

The conductance through the displayed system is evaluated numerically using the procedure described in Section 5.5 and (49). The conductance $g(E)$ here refers to the conductance from the state with energy E, and not the total conductance of all states with energies less than E. This $g(E)$ is also called the conductance fluctuation or differential conductance. The calculations are made for different lead configurations, fractal iterations l, and linear length scale resolutions n. The conductance for the Sierpinski Carpet with central lead position and linear length scale resolution $n = 2$ at varying fractal iterations is shown in Figure 27. The maximum values in the conductance are $g(E) = 2 \cdot G_0$, corresponding to two conducting channels. This means there are two sets of modes in the leads that contribute to the conduction in (49) at these energies. This would not have been obtained had we represented the leads with only a single line of points. Fifty thousand linearly spaced energies are used to sample the conductance in Figure 27. The number of energies used in the sampling of the conductance will be referred to by the symbol N_C. In the numerical calculations, N_C was of the order $10^5 - 10^6$.

It can be seen that as the fractal iteration l increases, more and more details appear in the conductance. In the case of $l = 4$, the number of sampled points $N_C = 50000$ used in Figure 27 is insufficient to demonstrate the full detail of the curve. Furthermore, recall that the true fractal is obtained when the fractal iteration l goes to infinity. This rapid increase in detail in the conductance for increasing l indicates that the conductance plot of the Sierpisnki Carpet at $l = \infty$ would have infinite detail. It is thereby recognized that the conductance is in fact a fractal itself. This result was first found by van Veen et al. (2016) in the case of the Sierpinski Carpet.

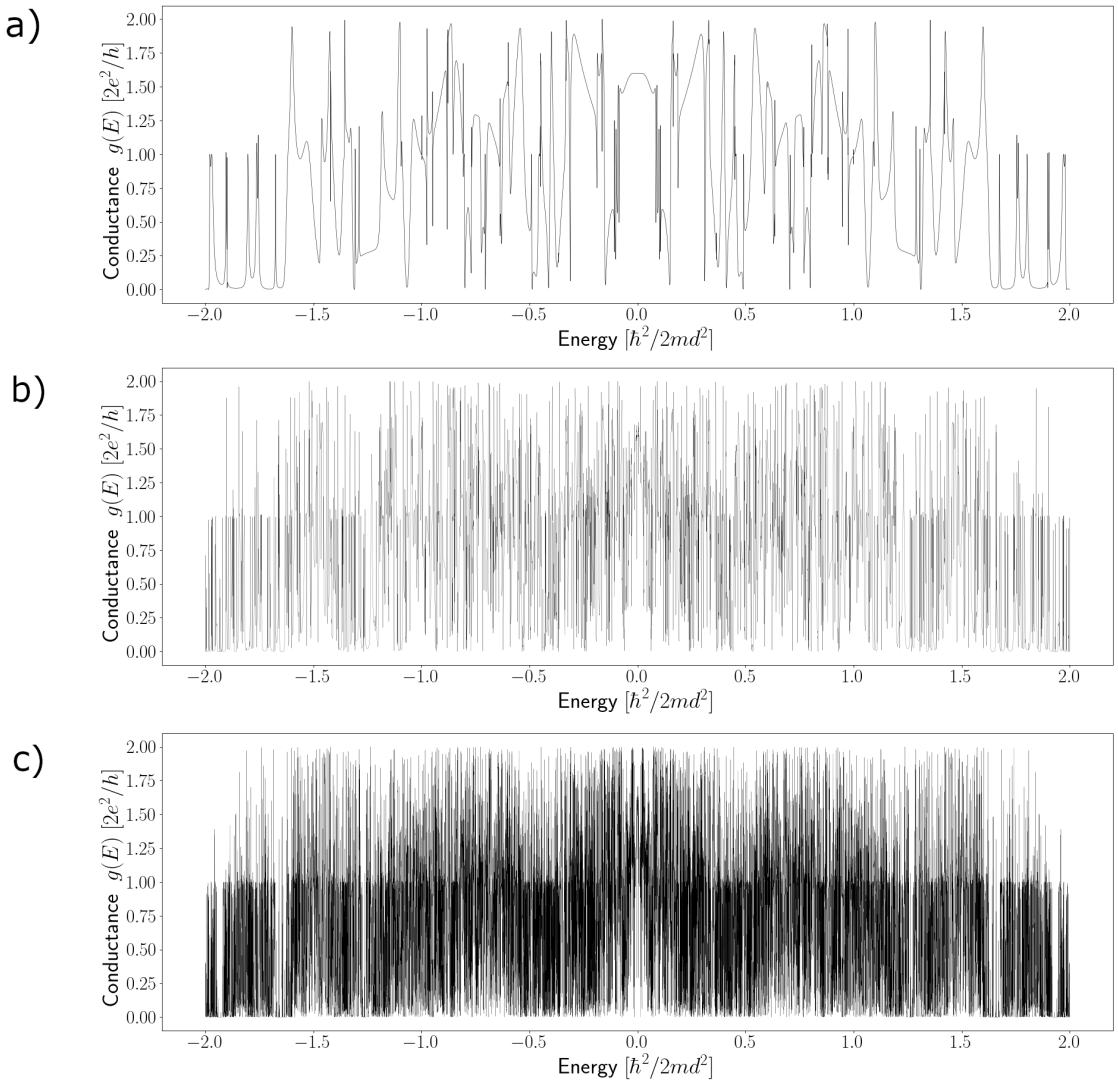


Figure 27: Conductance through the Sierpinski Carpet at different fractal iterations with linear length scale resolution $n = 2$. In all cases, the conductance $g(E)$ is sampled for 50000 linearly spaced energies. In (a), the fractal iteration $l = 2$ is used, and the sampling is sufficient to see all details. In (b), the fractal iteration is $l = 3$, and more details are seen to appear. In (c), the fractal iteration is $l = 4$, and the number of details is large. Increasing the number of sampled points further leads to even more details appearing.

Knowing that the conductance plot is fractal, we wish to evaluate the Hausdorff dimension. The box-counting method described in Section 2.3 is used to approximate the Hausdorff dimension. In short, one counts the number of boxes of a given size that are necessary to cover an object, next the box size is varied. For an intermediate region called the scaling region, a power-law dependence between the number of boxes and box size can be seen. From the slope of this power law, one can estimate the dimension of the system. The box-counting analysis is carried out for the conductance of the Sierpinski Carpet at fractal iteration $l = 3$, linear length scale resolution $n = 2$ and with a sampling of $N_C = 10^6$ points. The result is shown in Figure 28. In Figure 28, the dashed black line indicates a power law dependence

equal to the Hausdorff dimension of the Sierpinski Carpet. Notice how this coincides with the slope of the box-counting results in the intermediate, scaling region. This remarkable result shows that the box-counting dimension of the conductance plot in Figure 27, is the same as the Hausdorff dimension of the Sierpinski Carpet. We will investigate if this relation holds for other fractals as well. The result was first found for the Sierpinski Carpet in van Veen et al. (2016), however, the paper attempted to also evaluate the property for the Sierpinski Gasket but could not conclude.

In Figure 29, the same calculation is repeated for different lead positions, and the result is unaffected. Furthermore, even though this discussion is done for electrical current and transport of electrons, by a change of units this can also apply to the transport of other quantum particles as was done by Krinner, Esslinger and Brantut (2017).

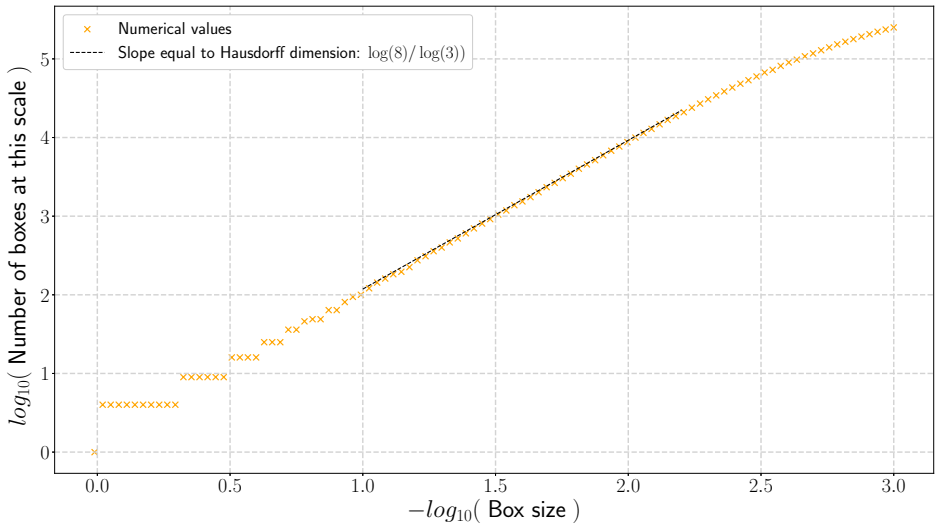
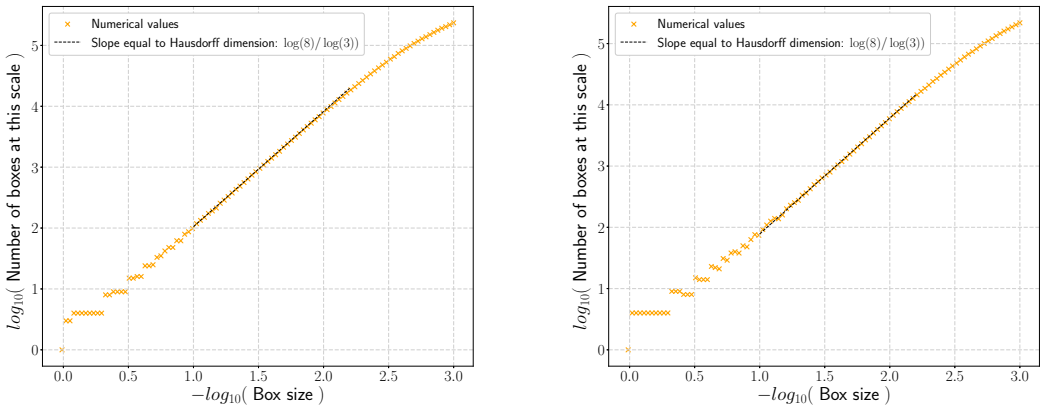


Figure 28: Box-counting analysis performed on the conductance plot of current through a Sierpinski Carpet at fractal iteration $l = 3$ and linear length scale resolution $n = 2$. The power-law scaling seen in the plots shows that the conductance plot has the same Hausdorff dimension as the Sierpinski Carpet itself, found in Section 4.3. This means that the fractal structure of the underlying object manifests in the transport properties through it. The conductance was sampled using $N_C = 10^6$ linearly spaced points, but the scaling can be seen for much smaller sampling rates as well.



(a) Diagonal (b) Corner

Figure 29: The box-counting analysis applied to the Sierpinski Carpet for different positions of the leads. Otherwise, the configurations are the same as in Figure 28. Figure (a) corresponds to *diagonal* lead positions, and (b) to the *corner* configuration. A small deviation is seen between the slope of the numerical points and the analytical scaling in (b). This is however contributed to the fact that it is difficult to obtain numerical accuracy in the *corner* configuration as the distance between leads is small.

7.2 Conductance through the Sierpinski Gasket

In order to compare our results with those of van Veen et al. (2016), the calculations are carried out for the Sierpinski Gasket before proceeding with other fractals. The conductance of the Sierpinski Gasket at fractal iteration $l = 6$ and linear length scale resolution $n = 2$ was computed using a sampling of $N_C = 6 \times 10^5$ points. The results are shown in Figure 30.

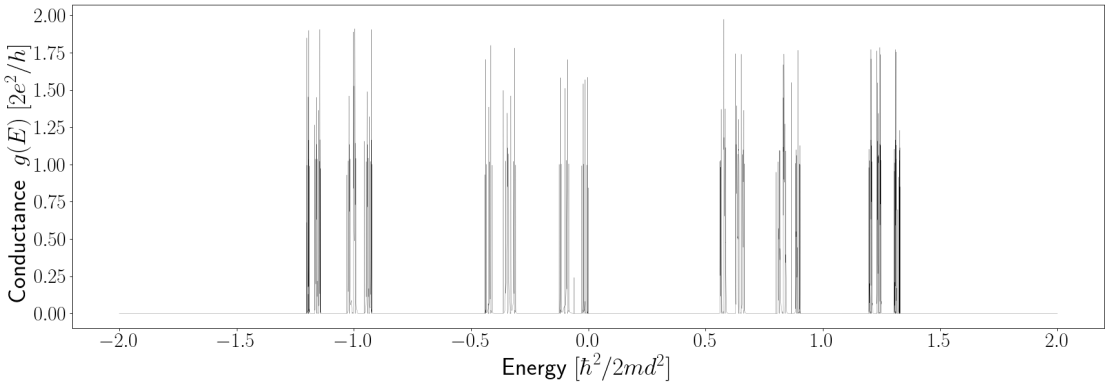


Figure 30: Conductance through a Sierpinski Gasket at fractal iteration $l = 6$ and linear length scale resolution $n = 2$ for varying gate potentials. The conductance displays regions of rapidly varying conductance separated by large energy gaps.

The conductance $g(E)$ in Figure 30 is qualitatively different from that of the Sierpinski Carpet in Figure 27. The conductance through the gasket displays islands of rapidly oscillating conductance, separated by large energy gaps. This indicates that for large ranges of energy, there is no wave function corresponding to a connection between the two leads. Thereby, there is no transport between the leads. These gaps are excluded when calculating the box-counting dimension of this plot. To do so, start by sampling the conductance with $N_C = 2000$ evenly spaced points. The energy gaps are then located as anywhere three consecutive points are approximately zero. A new sampling is made with $N_C \in (10^5, 10^6)$ points equally spaced over the remaining regions. Considering that the plot is fractal, the gaps might behave in a fractal way as well, and new gaps might appear in this second sampling. However, these are considered a part of the fractal structure and were not removed in the displayed result. Removing these was however tested, and it had a negligible effect on the results.

The Hausdorff dimension of the conductance plot is estimated by the box-counting method described in Section 2.3, and the result is shown in Figure 31. At first glance, the scaling relation is not as convincing as the one seen for the Sierpinski Carpet. The numerical data doesn't lie on a smooth line but seems to oscillate. Changing the lead positions was found to affect these oscillations and can make them more or less pronounced. This result is likely due to the numerical difficulty of evaluating the Sierpinski Gasket. It has a very low connectivity and is prone to imprecisions, see Section 4.8.

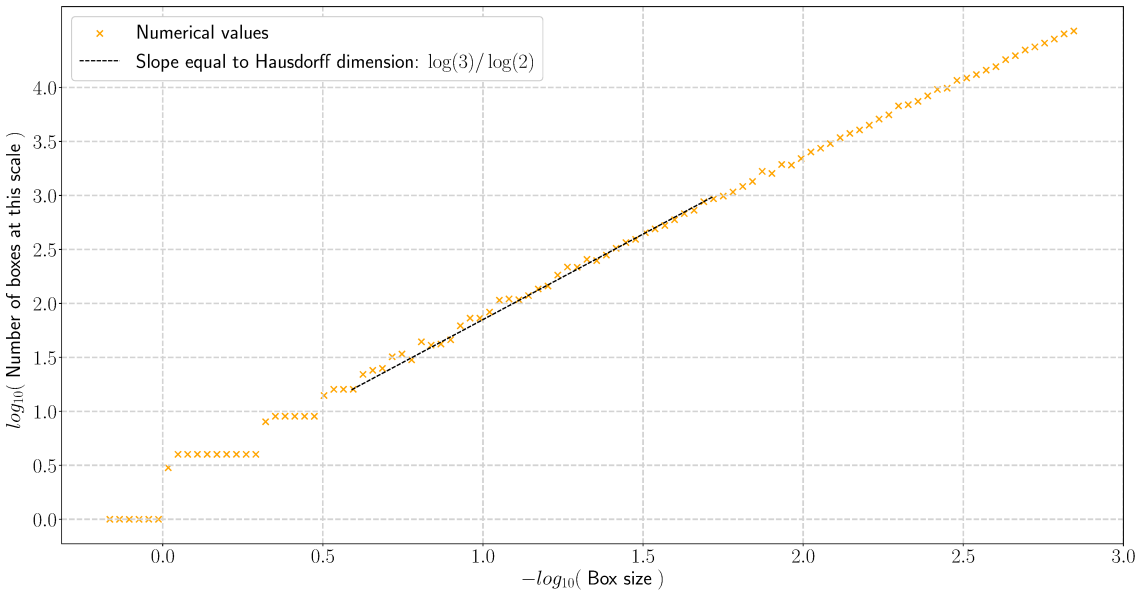


Figure 31: Box-counting analysis performed on the conductance plot for a current through a Sierpinski Gasket. The fractal was at fractal iteration $l = 6$ and linear length-scale resolution $n = 2$. The indicated power-law scaling corresponds to the Hausdorff dimension of the Sierpinski Gasket, $D_H = \log(3)/\log(2)$ as seen in Section 4.6. The result is not as convincing as the one seen for the Sierpinski Carpet in Figure 28.

The slope of the conductance plot is not affected by these oscillations and was found to be the same for different lead positions. That is, the slope is self-averaging and is recovered if sufficient data points are considered in the box-counting analysis. From Figure 31, it seems that the obtained numerical slope corresponds is the Hausdorff dimension of the Sierpinski Gasket. To verify this, zoom in on the scaling region of the box-counting analysis, using box sizes between 5% and 18% of the extent of the horizontal axis in the conductance plot. This is shown in Figure 32. Here, a linear regression of the data points is shown together with the theoretical scaling. The linear regression gives a numerical slope of 1.580, which is close to the predicted value of $\log(3)/\log(2) \approx 1.585$.

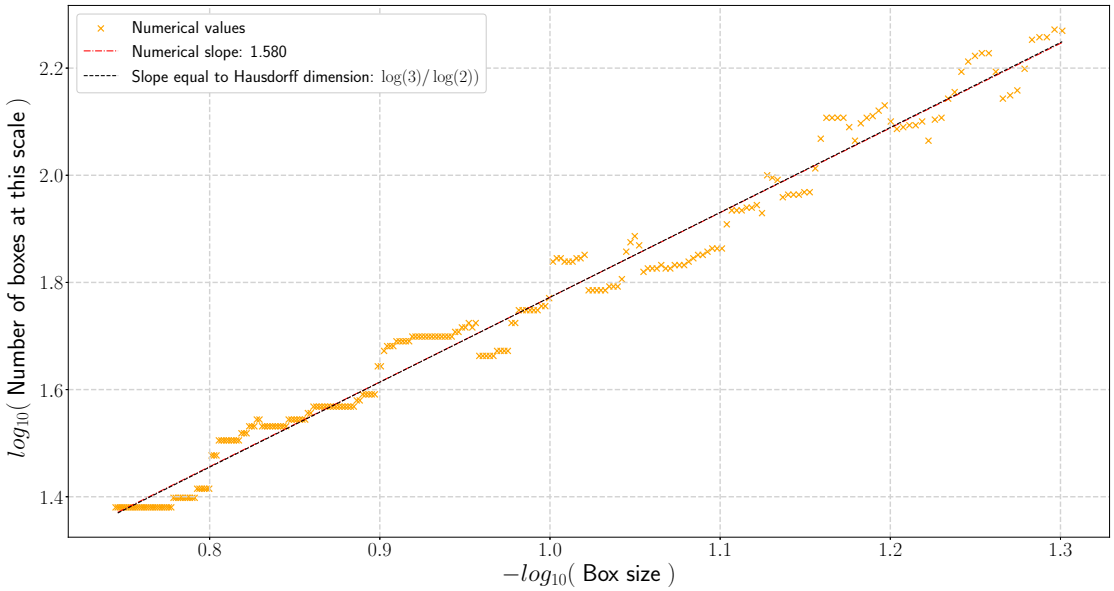


Figure 32: The scaling region of the box-counting analysis for the conductance plot of a Sierpinski Gasket. The points do not fall on a straight line, however, the average scaling found of 1.580 corresponds to the Hausdorff of the gasket, approximately 1.585.

To gain further confidence, the slope is calculated for different fractal iterations of the gasket, and the results are given in Table 7. The estimated dimensions are close to the theoretically predicted value of $\log(3)/\log(2) \approx 1.585$. The results show that the relation between conductance and fractal dimension found for the Sierpinski Carpet also holds in the case of the Sierpinski Gasket. That is, the Hausdorff dimension of the conductance plot is the same as the Hausdorff dimension of the underlying fractal. The result differs from that found by van Veen et al. (2016). That is, van Veen et al. (2016) did not recover the relation between the fractal dimensionality of the conductance and that of the underlying fractal potential for the Sierpinski Gasket.

Table 7: The estimated box-counting dimension of the conductance plot for the Sierpinski Gasket at different fractal iterations. The Hausdorff dimension of the Sierpinski Gasket itself is $\log(3)/\log(2) \approx 1.585$.

Fractal iteration l	Estimated box-counting dimension
2	1.427
3	1.534
4	1.619
5	1.557
6	1.580

From Table 7 it is also seen that using a large fractal iteration is not necessary to observe the Hausdorff dimension in the conductance plot. This is a rather peculiar result. Recall that the Hausdorff dimension of $\log(3)/\log(2) \approx 1.585$ corresponds to the fractal at iteration $l = \infty$. However, when calculating the conductance, a fractal at finite iteration l must be used. It seems that even if the fractal is represented at a low fractal iteration, and the potential does not accurately represents the true fractal, the conductance plot still exhibits a dimension close to the true Hausdorff dimension. From this, it would seem that the transport properties are determined by the larger, general structure of the fractal. Infinite, or high, detail is not required to get a decent estimate of the fractal dimension of the conductance plot in the limit $l = \infty$ for the Sierpinski Gasket. This is promising for anyone wanting to make use of this property in a physical realization of the Sierpinski Gasket.

7.3 Conductance through other fractals

The numerically estimated box-counting dimensions of the conductances $D_{BC}^{conductace}$ are plotted against the Hausdorff dimensions of the corresponding fractals $D_H^{fractal}$ in Figure 33. A linear slope is plotted together with the data points. This slope represents a relation that the fractal dimension of the conductance plot is equal to the fractal dimension of the underlying structure. The numerical data clearly fits this prediction.

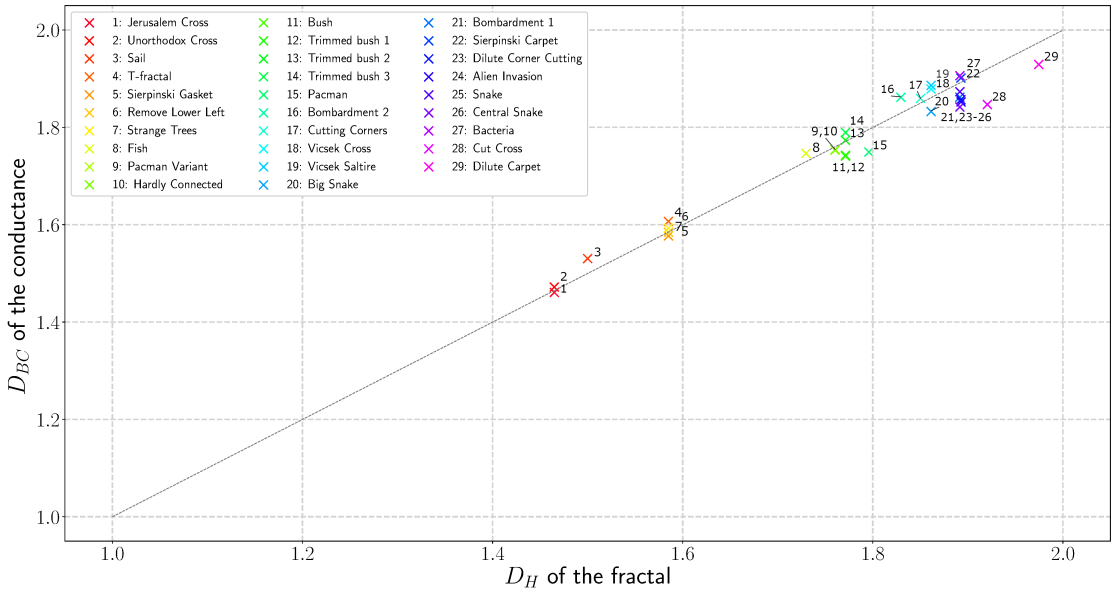


Figure 33: Numerically estimated dimensions of the conductances through fractals $D_{BC}^{conductance}$, plotted against the Hausdorff dimensions of the corresponding fractals $D_H^{fractal}$. A linear relation is evident, corresponding to $D_{BC}^{conductance} = D_H^{fractal}$. This shows that the fractal dimension of the conductance is determined by, and equal to the fractal dimension of the underlying structure.

Based on this result, together with the detailed study of the Sierpinski Carpet and Sierpinski Gasket in Sections 7.1 and 7.2, it is concluded that the discussed relation between the dimension of the conductance and the dimension of the underlying potential holds for the fractals studied in this thesis. That is, for transport through a fractal potential, the conductance is itself fractal with a fractal dimension determined by and equal to the Hausdorff dimension of the underlying potential. This can be written

$$D_{BC}^{conductance} = D_H^{fractal}. \tag{77}$$

The fractals considered here were simply connected, displayed a high degree of self-similar, and had vanishing areas as the fractal iteration increased. This includes a wide variety of fractals, and the result could hold for other fractals as well.

Upon increasing the fractal iteration l, the dimension of the conductance quickly approached the true Hausdorff dimension of the fractal at $l = \infty$. This fact made the systems possible to study numerically. This is also highly promising for anyone who wants to replicate such a system in a laboratory. Systems with more than high enough detail have already been realized by for example Kempkes et al. (2019). Based on the coherent transport model used here, it is expected that the conductance through such a system will carry information about the fractal nature of the structure.

Notice the fractals called Bush, Trimmed Bush 1, Trimmed Bush 2, and Trimmed Bush 3 in Figure 33. These four fractals are generated using the Method of Repeated Kronecker products given in Section 4.2. The four fractals have different details since their axioms are different, however, their generators are the same. In Section 4.2

it was predicted that the properties of the fractals should depend on the generator, and not the axiom. This is also what is seen from the numerical results in Figure 33, where the estimated dimensions of the conductances through these four fractals lie close to each other. The same holds for the fractals Jerusalem Cross and the Unorthodox Cross.

7.4 Significance of connectiviy

In the analysis of conductances through the Sierpinski Carpet and the Sierpinski Gasket, qualitative differences were found. Large energy gaps were found in the conductance plot of the gasket in Figure 30, which were not present in the results for the Sierpinski Carpet in Figure 27. The observed energy gaps can be related to the connectivity of the fractal as discussed in Section 4.8.

In the Sierpinski Gasket, there are relatively few available paths connecting any two points, and the fractal has low connectivity. In fact, one can separate the fractal into three equal parts by cutting only three edges or neighbor interactions. On the other hand, in the case of the Sierpinski Carpet, there exist many paths connecting different regions of the fractal, and the carpet is said to have high connectivity. The other fractals studied in this thesis also fall into one of the groups, those with high connectivity and those with low connectivity.

The fractals with low connectivity generally displayed large energy gaps in the conductance plots like those that were shown for the Sierpinski Gasket. On the other hand, the fractals with large connectivity did not display such gaps and their results looked qualitatively more like the results for the Sieprinski Carpet. This is likely related to the fact that the energy levels in the fractals with low connectivity share unique properties and can even be derived analytically [Shima (1996)]. These unique properties are discussed in greater detail in the context of level spacing statistics in Section 9.2.

The box-counting analysis for fractals with low connectivity was generally harder to evaluate. The scaling region was smaller, and larger values of the linear length scale resolution n and the conductance sampling N_C were necessary to study these systems. These systems also seemed more prone to numerical errors and displayed fluctuations in the box-counting analysis such as those seen in Figure 31. These issues are familiar limitations of the box-counting analysis. This was discussed briefly in Section 2.3, and a detailed discussion was carried out by Jiang and Liu (2012).

A method was applied to improve the results of the box-counting algorithm for a few of the fractals. Depending on the specific set-up, the conductances of the fractals might be able to take values between 0 and $2 \cdot G_0$, where G_0 is the conductance quantum defined in Section 3.5. This is not general but it was the case in the relevant fractals. It was found that the box-counting analysis was more stable when considering only the larger values of the conductances, specifically in the range of $(1-2)\,G_0$. The motivation for making this consideration in the first place was that the smaller values are expected to be more prone to numerical errors. Furthermore,

in some almost fully one-dimensional fractals, one channel was found to remain open in intervals, giving $g(E) \geq g \cdot G_0$. In these few cases, the fractal dimension was more clearly observed when considering only the larger values of $g(E)$, corresponding to two conducting channels being open. This method was used to obtain accurate results for the fractals named Jerusalem Cross, Unorthodox Cross and Remove Lower Left in Figure 33. In the Flag-fractal, it was difficult to recover a clear scaling in the box-counting analysis and it was excluded from Figure 33.

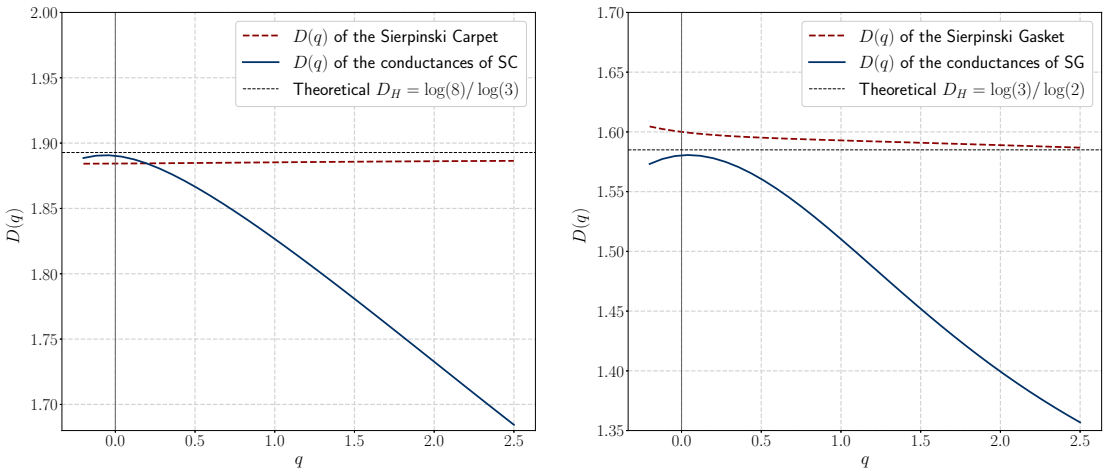
7.5 Multifractal analysis of the conductances

A possible explanation as to why the regular box-counting analysis sometimes struggled to characterize the dimensionality of the conductances could be because they are in fact multifractal. The concept of multifractals was discussed in Section 2.3. Multifractals are not completely described by a single fractal dimension, but can instead exhibit multiple dimensions for different regions or moments.

A multifractal analysis was suggested in Section 2.3 using the generalized dimension $D(q)$ which can be seen as an extension of the box-counting analysis. In this analysis, one considers the scaling of different statistical moments q in the system and finds a dimension $D(q)$ based on the scaling of each of these moments. The result from the box-counting analysis is recovered for $q = 0$. The generalized dimension $D(q)$ reveals if the system exhibits different fractal dimensions for different moments.

In a monofractal, there is only one fractal dimension and one expects that $D(q)$ is almost constant for different q. A slow decrease in $D(q)$ is however expected as the exponent q increases. The fractal potentials are for example monofractals. On the other hand, a multifractal is described by different fractal dimensions for different statistical moments. In this case, it is expected that the generalized dimension $D(q)$ has a much stronger dependence on the moment q. The goal is to determine whether the obtained conductances are monofractals or multifractals.

A multifractal analysis was performed on the Sierpinski Gasket and the Sierpinski Carpet along with the conductances through both systems. The results are shown in Figure 34. For both fractals, it is clear that the potentials themselves vary slowly with moments q. On the other hand, the generalized dimensions $D(q)$ for the conductances yield greater dependencies on q. Based on this, it is concluded that the conductances are multifractal and are characterized by more than one fractal dimension. As mentioned, the generalized dimension equals the box-counting dimension in the case of $q = 0$. In the context of multifractals, this dimension is referred to as the capacity dimension. A refined version of our statement from Section 7.3 would then be that for transport through a fractal, the conductance is multifractal with a capacity dimension equal to the Hausdorff dimension of the underlying fractal.



(a) Sierpinski Carpet

(b) Sierpinski Gasket

Figure 34: The generalized dimension $D(q)$ is plotted against moments q. Figure (a) displays the results for a discrete realization of the Sierpinski Carpet together with the results for the conductance for transport through this fractal. Figure (b) shows the results for a discrete realization of the Sierpinski Gasket and the conductance through this fractal. The results show that the conductances through the fractal structures are multifractal, meaning that they are characterized by more than one fractal dimension.

As a final note, it is added that the generalized dimension for the conductances in Figure 34b were calculated after removing energy gaps. If the energy gaps are kept, this makes the generalized dimension quickly decay to 1 when the momentum q is increased since the dimension of these gaps is 1. This is as expected and confirms that the analysis works. The reason it is obtained for large q is because the data points in these energy gaps lie closer to one another, i.e., they are denser, than the data points in the fluctuating parts of the fractal. Recall that the conductance was sampled by evenly spaced points. The dense regions will dominate for large moments q, as was discussed briefly at the end of Section 2.3. Naturally, the data points in the energy gaps scale as a regular one-dimensional straight line. Therefore, $D(q)$ quickly approaches 1 for increased q if the energy gaps are included.

7.6 Experimental realization

An experiment to investigate the conductance of quantum particles through fractals is suggested. The experiment is based on the work of Krinner et al. (2015) and Krinner, Esslinger and Brantut (2017) and is in a cold atoms system. Further details on the set-up can be found in See Krinner, Esslinger and Brantut (2017).

Starting with an atomic cloud, the cloud prepared into a cigar shape using a dipole trap as depicted in Figure 35a. Next, a blue-detuned TEM01-like laser mode is propagated along the x-axis and focused onto the center of the cigar as depicted in Figure 35b. Finally, the fractal structure should be imprinted onto the obtained

quasi-2D channel. The method for carrying out this final step is not fixed from this thesis, but the work of Kempkes et al. (2019) is suggested as a place to start.

In order to have transport, the chemical potential in the two reservoirs needs to be different. This can be obtained by creating one of the clouds bigger than the other when applying the laser mode. After this, one can imagine letting the experiment run while measuring the transport of atoms through the channels. This would yield the total conductance for varying voltage bias. This could then be used to find the differential conductance as used in this thesis. Alternatively, one can move the channel more to one side or the other, squeezing one side of the atomic cloud while stretching the other, thereby changing the chemical potentials.

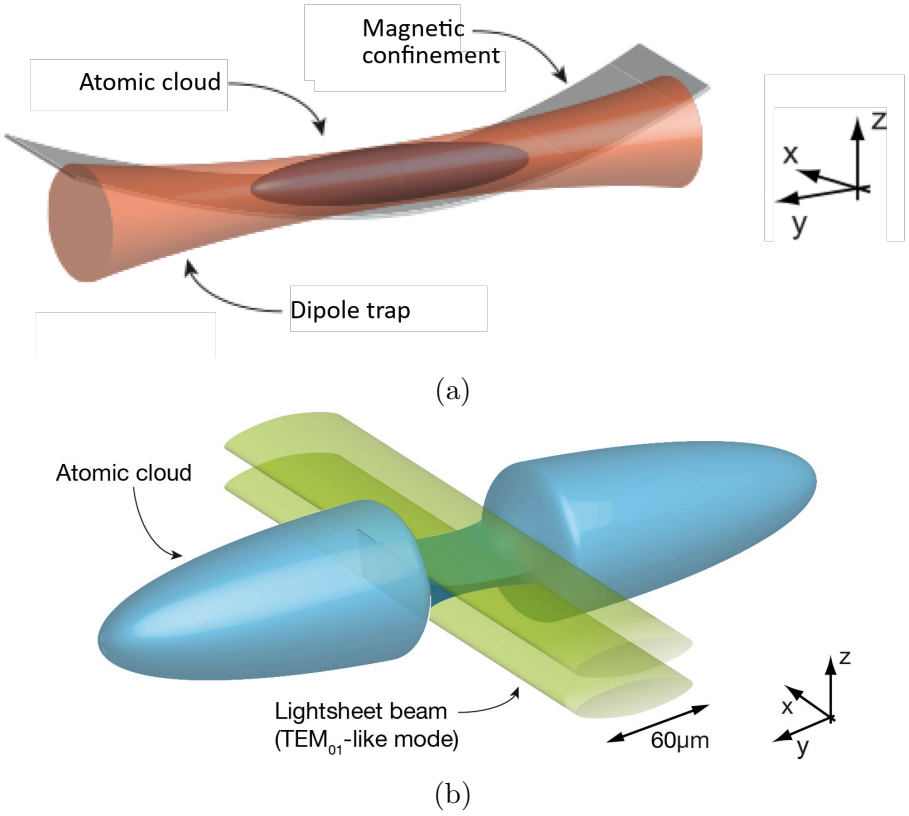


Figure 35: An experiment to measure the conductance through a fractal is suggested based on the work of Krinner, Esslinger and Brantut (2017). In (a), an atomic cloud is formed into a cigar shape using a dipole trap. In (b), a laser mode is used to separate the cloud into two reservoirs, connected through a quasi-2D channel. As a final step, one can imagine imprinting a fractal structure onto the channel.

Source: Krinner, Esslinger and Brantut (2017).

8 Participation ratio

In order to further investigate the cause of the results found for the conductances in Section 7, the localization of states is considered. This section starts with a short introduction to the motivation and methodology of studying the localization

of states. The discussion then continues on the localization of the eigenstates in fractal potentials. Next, an interpretation of the results is given together with their relation to the results found for the conductances. Finally, a discussion on the periodicity of fractals in the context of the observed results is made.

8.1 Participation ratio

From the scattering theory of transport, and specifically (70) and (49), it is seen that conductances greater than zero correspond to an eigenstate stretching between the two leads. Thus, if there one observes a conductance greater than zero between two sufficiently separated leads at a certain energy, it is expected that there is an extended state corresponding to this energy. The conductance is therefore closely related to the localization or extension of the wave functions. The states do not need to be fully extended, so long they make contact between the two leads.

Motivated by this, we want to investigate the localization of states in the fractals and determine whether this can be the cause of the fractal conductances seen in Section 7. Start by quantifying the localization of a state using the participation ratio defined as

$$PR(E) = \frac{(\int |\Psi(\mathbf{r},t)|^2 \, d\mathbf{r})^2}{\int |\Psi(\mathbf{r},t)|^4 \, d\mathbf{r}}. \tag{78}$$

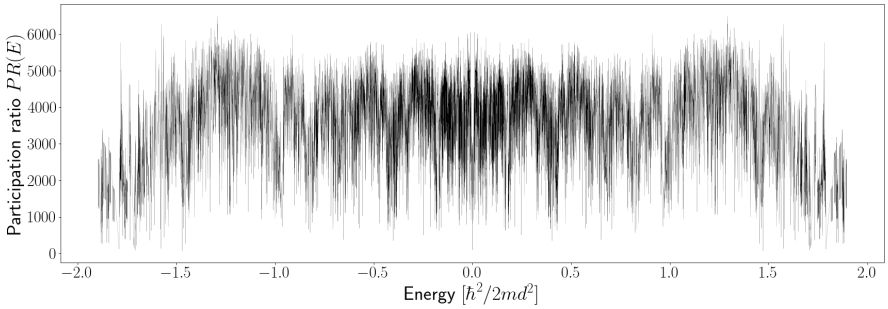
If the state is normalized, the numerator in (78) is simply equal to 1. Furthermore, for highly extended states, the in denominator (78) becomes small, and PR is large. Contrary, for an exactly isolated state, PR equals 1. For a normalized wave function in a time-independent system discretized onto a $N \times N$ grid, (78) then becomes

$$PR(E) = \frac{1}{\sum_i^N \sum_j^i |\psi_{i,j}|^4}, \tag{79}$$

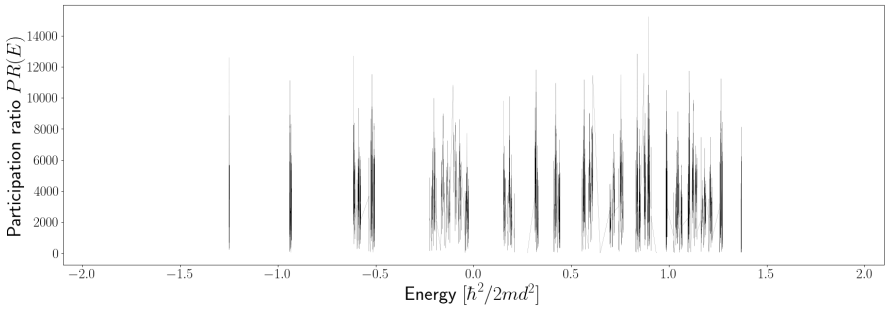
where $\psi_{i,j}$ is the amplitude of the wave function at site $\{i, j\}$. Equation (79) can be evaluated for the eigenstates found through exact diagonalization of the fractals.

8.2 Participation ratios of the fractals

The participation ratios of the eigenstates of the Sierpinski Carpet at fractal iteration $l = 4$ and linear length scale resolution $n = 2$ were evaluated using (79). The result is shown in Figure 36a. Figure 36a qualitatively resembles the plot of the conductance through the same fractal system in Figure 27. In addition, by adding more detail to the fractal potential, more detail appears in the plot of the participation ratio. The results indicate that the participation ratio as a function of energy is a fractal.



(a) Sierpinski Carpet



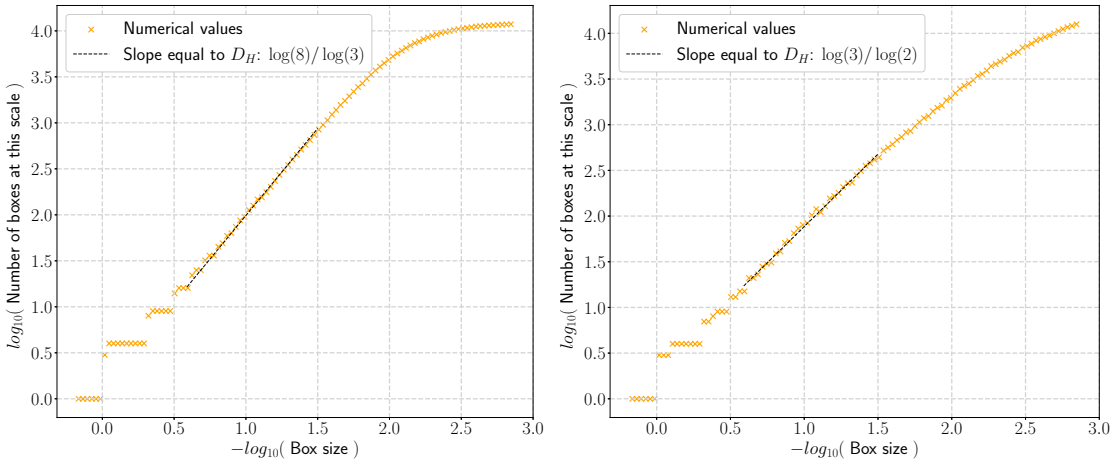
(b) Sierpinski Gasket

Figure 36: Participation ratios $PR(E)$ of the eigenvectors for the Sierpinski Carpet and the Sierpinski Gasket. The fractal iterations used were $l = 4$ and $l = 6$ and linear length scale resolution $n = 2$ and $n = 7$, respectively. Exact diagonalization is performed numerically on the discrete Hamiltonian of the system, and the participation ratios are calculated using (79). These are then plotted against the corresponding energy eigenvalues.

Motivated by Figure 36a and the results from Section 7, the box-counting dimension of the participation ratio is computed. It is expected that this numerical evaluation of the box-counting dimension will be less precise than those found for the conductances earlier. This is due to the relatively few data points available for the participation ratio as compared to the conductance. Following the same approach as in Section 7.1, we obtain an estimate of the box-counting dimension as shown in Figure 37a. It can be seen that, in the case of the Sierpinski Carpet, the fractal dimension of the participation ratio plot is approximately the same as the Hausdorff dimension of the fractal potential. This is the same result that was obtained for the conductance through the Sierpinski Carpet in Section 7.1.

The analysis is repeated for the Sierpinski Gasket, similar to what was done for the conductance in Section 7.2. The obtained result for the participation ratios is shown in Figure 36b. The participation ratios are to the results found for the conductance through the same structure in Figure 30, with islands of fluctuations, separated by large regions with no extended states. The box-counting analysis for the participation ratio of the Sierpinski Gasket is shown in Figure 37b. It is seen that the box-counting dimension of the participation ratio is equal to the Hausdorff dimension of the potential in this case as well. Note that when evaluating the box-counting dimension of the Sierpinski Gasket, the regions with no extended states

were removed, as was done in the conductance case. Details of this procedure were given in Section 7.2.



(a) Sierpinski Carpet (b) Sierpinski Gasket

Figure 37: The box-counting analysis applied to the participation ratios of (a) the Sierpinski Carpet and (b) the Sierpinski Gasket. The fractal iterations used were $l = 4$ and $l = 6$, respectively, and the linear length scale resolutions were $n = 2$ and $n = 7$. The participation ratio at a given energy is found by applying (79) to the eigenvectors after the exact diagonalization of the Hamiltonian.

When evaluating the conductances in Section 7, we could compute $10^5 - 10^6$ data points. In the case of the participation ratio, a mere $10^3 - 10^4$ data points were used. It is difficult, or rather impossible, to obtain equivalent precision in the participation ratio calculations as in the conductance calculations through the employed method. This is due to the calculations of participation ratios using exact diagonalization. For a given discrete realization of a fractal, one can only obtain so many eigenvectors from the exact diagonalization of the Hamiltonian. Therefore, there's a limited set of data points in the participation ratio plot, which affects the performance of the box-counting analysis. Increasing the size of the system quickly becomes unfeasible due to the time complexity of the exact diagonalization procedure, see Appendix A for details. In the method used for the conductances on the other hand, one could evaluate the conductance for as many energies as desired, yielding a large amount of data points to be used in the box-counting method. For this reason, it is not produced a plot for the box-counting dimensions of the participation ratios equivalent to that of Figure 33 for the conductances.

8.3 Interpretation of results and relation to conductance

The results in Figure 36 demonstrate that if there is an extended state at a specific energy, there does not exist a neighborhood in energy in which the state is guaranteed to remain extended. That is, there is no neighborhood of stability, and even an infinitesimal change in energy could change an extended state into a localized state,

and vice versa. In terms of quantum mechanics, there are no energy bands. Furthermore, Figure 37 shows that the manner in which the states fluctuate between being extended and localized is determined by the fractal dimensionality of the potential. This is seen as the Hausdorff dimension of the fractal potential manifests into the dimension of the participation ratios. One can write this property as

$$D_{BC}^{participation\ ratio} = D_H^{fractal}. \tag{80}$$

It is once again stressed that (80) has not been explicitly shown for all the fractals in this thesis due to the numerically exhaustive evaluation arising from the exact diagonalization in the employed mehod.

From the scattering theory of transport in Section 3.5, it is seen that in order to have a conducting state, there needs to be a connection between the two leads. If the leads are separated from one another, that means that a non-zero conductance is expected to correspond to an extended state. This means that large conductances are associated with large participation ratios. When the states rapidly fluctuate between being extended and localized, this will cause the conductance to rapidly fluctuate. At this point, it is additionally concluded that the discussed relationship between the dimension of the conductance and the Hausdorff dimension of the fractal potential arises due to these fluctuations between extended and localized states. This is based on the above discussion together with the agreement between the box-counting analysis applied to the conductances and participations ratios in Figures 28, 31 and 37, as well as the qualitative similarity between the plots of the conductances and participation ratios in Figures 27, 30 and 36. The relation given in (77) is thus the direct consequence of (80). The results can be written together as

$$D_H^{fractal} = D_{BC}^{participation\ ratio} = D_{BC}^{conductance}. \tag{81}$$

8.4 Periodicity of fractals

Locally, fractal structures appear irregular and aperiodic, with an intricate, infinite amount of detail on different length scales. However, the considered fractals also display translational invariance on large scales due to their self-similarity.

Highly extended states, such as those observed as large values of $PR(E)$ in Figure 36, are common in regular, periodic systems. On the other, irregular, aperiodic systems display localized states, such as those observed as small values of $PR(E)$ in Figure 36. It was shown above that extended and localized states are "intertwined" in the fractals, existing side by side, with no neighborhood of stability around them.

Although the fractals considered have translational invariance on large scales, it would seem that the infinite amount of detail leads to them to also displaying aperiodic behavior. One could therefore attempt to understand the fractals as displaying a combination of properties between periodic and aperiodic systems. This might help understand the fluctuations between extended and localized states which leads to the relationships in (77) and (80).

As it turns out, however, viewing the fractals simply as intermediately periodic systems is not satisfactory, and this viewpoint does not explain all spectral properties

of the fractals. This is seen from the analysis of the level spacing statistics in the following section.

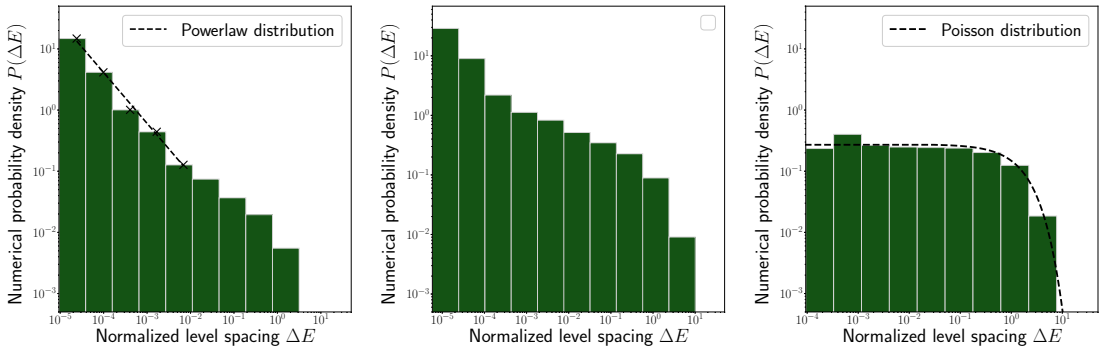
9 Level spacing statistics

In the following section, the level spacing statistics of the eigenvalues of the fractal potentials are discussed. First, a short motivation for this analysis is given. Then, the level spacing statistics of the different fractals are presented and discussed. Further discussion is given on the impact of the connectivity of the fractals on these results. Finally, a note on the terminology used in this discussion is given. The theoretical framework of this section was presented in 3.6 and the specifics of evaluation were considered in 5.6.

In Section 8, it found that the fractals display fluctuations between localized and extended states. As discussed in Section 8.4, one can attempt to model this as an interplay between periodic and aperiodic behavior. A way to investigate whether a system is periodic or aperiodic is by considering the level spacing statistics of the system. As discussed in Section 3.6, the level spacing distribution of a system is determined by the symmetries of the underlying problem. The Poisson distribution is characteristic of uncorrelated energy levels, as is often found in integrable, typically periodic, systems. On the other hand, the Wigner-Dyson distributions arise in systems with chaotic (aperiodic) or strongly disordered behavior, where the energy levels are highly correlated. Locally, the considered fractals can appear disordered, having intricate details on every length scale. However, they also display translational invariance and periodicity on large scales. It is then interesting to see whether the level spacing statistics reflect that of a periodic or aperiodic system. The results did however turn out unexpected.

9.1 Level spacing statistics of the fractals

Analysis of the level spacing statistics of the fractals was carried out as demonstrated in Section 5.6. Figure 38 shows the level spacings of the Sierpinski Gasket, Vicsek Saltire and Sierpinski Carpet. The results of these three systems are representative of the findings for all the fractals considered in this thesis. In the case of the Sierpinski Gasket, one observes a decreasing power-law scaling in the log-log histogram of the energy spacings. This is a highly unique energy level spacing distribution. The obtained level spacing distribution has been documented once before for the Sierpinski Gasket by using an analytical method, see Iliasov, Katsnelson and Yuan (2019) and Iliasov, Katsnelson and Yuan (2020), but not for other fractals. In the Vicsek Saltire, this region of power-law scaling is somewhat less pronounced, though still present. However, for large energy spacings, the histogram displays a different distribution, showing a smoother tail than the results for the Sierpinski Gasket. In the case of the Sierpinski Carpet, no clear region of decreasing power-law scaling can be observed. Instead, the distribution resembles a Poisson distribution, corresponding to a regular periodic system.



(a) Sierpinski Gasket (b) Vicsek Saltire (c) Sierpinski Carpet

Figure 38: Level spacing distributions of (a) the Sierpinski Gasket, (b) the Vicsek Saltire and (c) the Sierpinski Carpet. The fractal iterations l and linear length scale resolutions n used were (a) $l = 7$, $n = 3$, (b) $l = 3$, $n = 2$ and (c) $l = 3$, $n = 7$. The results display an interplay between two distributions. A decreasing power law scaling is visible for the Sierpinski Gasket in (a). The Poisson distribution, related to a periodic system from random matrix theory, appears in the case of the Sierpinski Carpet in (c). The results displayed for the Vicsek Saltire in (b) show the interplay between the two distributions. The result for the Vicsek Saltire is expected to approach that of the Sierpinski Carpet if calculated for higher resolutions, note that only $n = 2$ was used here.

Qualitatively, the fractals considered fall into one of the three cases, see Table 8 for details. Based on the observed results, the decreasing power-law scaling seems to be associated with the connectivity of the fractals.

Table 8: The table shows whether the level spacing distributions of the eigenvalues of given fractals exhibit a region of decreasing power-law scaling. See Figure 38 for examples of each category. This is based on the results from discrete realizations of the fractals. The decreasing power law scaling in the fractals marked *in between* are expected to become less pronounced or disappear completely in a continuous realization of the fractals.

Decreasing power-law scaling		
Clear scaling	In between	No clear scaling
Sierpinski Gasket	Vicsek Saltire & Cross	Sierpinski Carpet
T-fractal	Pacman & Variant	Dilute Corner Cutting
Jerusalem Cross	Bush	Bacteria
Unorthodox Cross	Trimmed Bush $1-3$	Alien Invasion
Hardly Connected	Bombardment 2	Fish
Flag-fractal	Cut Cross	Dilute Carpet 5
Strange Trees	Remove Lower Left	Quiver
Sierpinski Curve & Square Sail	Cutting Corners	

9.2 Level spacing distribution and connectivity

Connectivity and ramification numbers were discussed in Section 4.8. Simply put, low connectivity means that there are few paths connecting any two sites in the fractal. High connectivity means there are many or infinite paths connecting any two sites. High connectivity is associated with a large or infinite ramification number and low connectivity with a finite and small ramification number. For fractals with low connectivity, such as the Sierpinski Gasket, the decreasing power-law scaling in the level spacing statistics is evident. In the case of highly connected fractals, such as the Sierpinski Carpet, the level spacing follow a Poisson distribution, which is associated with a periodic system. One way of interpreting this is that in highly connected fractals, the states spread out and feel the periodicity of the fractal. On the other hand, in the less connected cases, the wave function is more isolated, and it does therefore not observe the periodicity.

The decreasing power-law scaling implies that there is a high likelihood of observing small energy level spacings in the systems with low connectivity. The energy levels are tightly packed, and there is no level spacing repulsion. On the contrary, there might seem to be an effective level spacing *contraction* based on the result. That is, the energy levels lie closer than what is expected from a system with fully independent degrees of freedom, which would follow a Poisson distribution.

Lastly, there are fractals displaying properties in between these two distributions, such as the Vicsek Saltire. However, some of these fractals have low connectivity due to the discrete realizations of the fractals. Because of the high complexity of the Vicsek Saltire, it is difficult to make a realization at sufficiently high fractal iteration l, while maintaining a large value for the linear length scale resolution n. Recall that n is defined as the number of grid points used to represent the smallest length scale in the system. In the discrete realization of the Vicsek Saltire, there was a limited amount of paths available between any two sites. This could have led to the level spacing attaining properties similar to that of lowly connected systems. However, in a continuous realization of the Vicsek Saltire, the system might attain properties closer to that of the Poisson distribution seen for the Sierpinski Carpet. This also goes for other fractals in this intermediate group.

Low connectivity, and a finite ramification number, are associated with fractals with analytically solvable eigenvalues. Particularly, it was shown by Shima (1996)[5] that the eigenvalues of a fractal with low connectivity at iteration $l = l'$ can be found from the eigenvalues of iteration $l = 0$ through a recursive process called spectral decimation. In the same paper, the existence of an upper bound for the integrated number of states $N(E)$ was found. The results of this thesis indicate that this is associated with a decreasing power law scaling in the level spacing distribution of the fractal.

The obtained level spacing distributions do not advocate viewing fractals as simply showing an interplay between periodic and aperiodic behavior. Instead, the level spacing statistics of fractals were found to entail a deeper complexity than expected. A decreasing power-law scaling was found in the level spacing distributions

[5]See 9.3 for an explanation of the terminology used in by Shima (1996).

of the fractals with low connectivity. This might be understood as an energy level contraction. The result does not seem to have a satisfactory explanation from random matrix theory. A correlation was not established between the slope of the decreasing power law and the properties of the underlying potential. However, such a relationship is not ruled out. One might consider quantifying the connectivity of the fractal and look for a relationship between the slope and the degree of connectivity. A possible quantization might be made considering the number of hopping terms connecting two blocks of a fractal, divided by the minimum resolution needed to represent the fractal. Alternatively, one can attempt to view the lattice and hopping terms as a complex network, and use for example the clustering coefficient to quantify how connected a fractal is. One can also consider measures such as Lacunarity, betweenness or concepts from network partition. It is also possible to study whether the slope is determined by the fractal dimensionality of the potential. A more extensive analysis of the level spacing statistics of fractals can be carried out.

9.3 A comment on terminology

This thesis references a paper by Shima (1996). Shima (1996) uses a terminology different from that of this thesis, and a comparison is included here for the convenience of the reader. Specifically, Shima (1996) carries out calculations for objects referred to as "p.c.f. self-similar sets", or post-critically finite self-similar sets. This is related to the connectivity used here.

First of all, an Iterated Function System (IFS) is a method of constructing fractals iteratively [Falconer (2003), Chapter 9]. A critical point is where the derivative of such a function is zero. P.c.f. self-similar then means that the post-critical set is finite, that is, there are only finitely many distinct critical points after applying the functions in the IFS any number of times. Next, to see the relation to connectivity, one must realize that the critical points of the iterated function system (IFS) are the points where the fractal branches or splits. This being finite, means that there are a finite number of branching points. This means that there is a finite number of connections one would have to sever in order to extract a subset of the fractal. This is how finite ramification number was defined earlier, which is associated with low connectivity. Therefore, if a set is post-critically finite, this means the set has a finite ramification number and low connectivity.

10 Closing remarks

Several spectral properties have been studied for multiple fractals. Specifically, the ground state energy at increasing fractal iteration $l \to \infty$, conductance through fractals, the localization of states and the level spacing statistics were studied. A summary of the results will be given here together with a concluding discussion, followed by an outlook on potential further research in this field.

10.1 Summary and conclusion

Consistent results have been obtained across the different fractal potentials. This has made it possible to distinguish between numerical artifacts and physical properties.

The first sections of this thesis provided discussions on the underlying theory for the study of fractals. Topics from quantum mechanics, quantum transport, level spacing statistics, measure theory, topology and chaos theory were discussed in a consistent language, bridging concepts between the different fields. Furthermore, the methodology for the study of fractals was considered, and new methods were discussed. A method for reducing the complexity of the system's Hamiltonians through interior indexing was derived. The method was found to significantly improve the performance, see Appendix A.2.

Generating and characterizing fractals are not trivial. The fractals studied in this thesis were highly or exactly self-similar, simply connected and most had areas that tended to zero as more detail was added. The fractal Hasudorff dimension D_H, the integer topological dimension D_L, the linear rescaling factor r and the number of copies m were used as the primary tools of characterization for the fractal potentials, all defined in Section 2.2. A new and highly efficient method for generating fractals using Kronecker products was introduced and dubbed the Method of Repeated Kronecker Products. In this method, all of the above characteristics become trivial to assess through what is referred to as the "generator". Furthermore, the discrete realizations of the fractals were characterized by the fractal iteration l and the linear length scale resolution n, both discussed in Section 4.1. In addition, two main groups were considered, fractals with low and high degrees of connectivity, see Section 4 for details.

The ground state energy as a function of the fractal iteration was studied for the different fractals. The energy at a given iteration l' was studied in relation to the energy at the preceding iteration, $l' - 1$. The scaling was quantized by the energy scaling factor s such that $\lim_{l\to\infty} E_l \propto s \cdot E_{l-1}$. It was found that the energy scaling factor was given by $s = r^{D_L}$. This is what one would expect for a normal Euclidean system. That is, the fractal nature of the system had no manifestation in the results for the scaling of the ground states. It was in Figure 21 demonstrated that the ground state wave function becomes highly localized as the fractal iteration increases. This was also seen indirectly through the scaling between consecutive energy levels in Table 6. It could seem that the ground state wave function only resides in multiple localized islands in the system for large iterations. It is theorized that, as a consequence of this, the wave function does not experience the global structures of the system, and therefore not the fractal nature of the system. This is supported by the fact that the found energy scaling factor has no dependency on the number of copies in the system m which gives information about the global structure of the fractal.

Next, the conductances $g(E)$ of transport through the fractal potentials were considered. Here, $g(E)$ is the contribution to the total conductance from the state with energy E. The conductances were found to fluctuate rapidly for varying energy and displayed ever-increasing detail as the details of the fractals were increased. From

this, it was concluded that the conductances themselves were fractal. By further analysis, they were found to be multifractals, meaning they display different scaling properties for different moments. The non-integer box-counting dimensions, also known as the capacity dimensions, of the conductances were found to be equal to the Hausdorff dimensions of the underlying fractal potentials. This was shown for several fractals, and the results are displayed in Figure 33. The results show that the fractal nature of the potentials led to consequences in the physically observable quantities of the systems.

To investigate the cause of the conductance results, the localization of states was studied. The participation ratios $PR(E)$ of the eigenvectors at a given energy were evaluated. As the energy varied, the eigenvectors fluctuated rapidly between localized and extended states. Adding more details to the fractal potentials led to increased detail appearing in the participation ratios, and the participation ratios were found to be fractal. The results show that if there exists an extended state at a specific energy, there does not necessarily exist a neighborhood around this energy where the state remains extended. In terms of quantum mechanics, there are no energy bands. Furthermore, the box-counting dimensions of the participation ratios were the same as the Hasudorff dimensions of the underlying potentials. This is the same result that was obtained for the conductances.

It is argued that the fractal quality of the conductance is a direct consequence of the fractal quality of the participation ratio. If one attaches leads to the fractal sufficiently far from each other, one must have an extended state in order to measure non-zero conductance. The criterion is not sufficient, but it is necessary and can be seen from the quantum scattering theory of transport, discussed in Section 3.5. A fluctuation between extended and localized states will therefore lead to a fluctuation in conductance. It is from this understood that the oscillation in localization is what drives the oscillation in conductance. This is also supported by the qualitative similarity between the plots of conductances and participation ratios of the fractals in Figures 27, 30 and 36, as well as the agreement between the box-counting dimensions of the conductances and the participation ratios. Hence, the presence of the Hausdorff dimension of the fractal potential in the conductance is a result of its appearance in the participation ratio. The results were summarized in (81) which reads

$$D_H^{fractal} = D_{BC}^{participation\ ratio} = D_{BC}^{conductance}.$$

It is stressed at this point that it was not obtained accurate results for the participation ratios of all fractals due to the time complexity of the applied method. The result for the localization of states has therefore not been shown for as many fractals as the conductance relation. In addition, it is worth noting that this thesis only deals with a specific group of fractals, as detailed above. Fractals are a vast and vaguely defined set of objects, and one should be careful if one wishes to extrapolate the results to other fractals. Finally, it is noted that the procedures employed to evaluate the participation ratios and the conductances are markedly different. Participation ratios were found through an exact diagonalization of the fractal without any leads, followed by the application of (79). Conductances, on the other hand, were found by solving for the wave functions directly in (70) at fixed energy levels and for given lead configurations, thereafter inserting the obtained tunneling elements into (49).

The fact that one can observe the fractal dimension in both cases is reassuring for the methodology.

Based on the rapid fluctuations between extended and localized states, it was hypothesized that the fractals could be thought of as displaying a combination of periodic and aperiodic behavior. To investigate this, the level spacing statistics were studied. It is expected from random matrix theory that aperiodic systems display energy level repulsion. This leads to the energy level spacings attaining a Wigner-Dyson distribution, which follows an increasing power law for small energy-level spacings. Periodic systems on the other hand have no level repulsion and are expected to follow a Poisson distribution. However, a completely different level spacing statistic was obtained for some of the fractals. The level spacing distributions followed *decreasing* power-law scalings in fractals with low connectivity. For fractals with large connectivity, the results followed a Poisson distribution. Fractals with intermediate connectivity displayed an interplay between these two distributions as shown in Figure 38. The decreasing power-law distribution is suggested to be a property of all such self-similar, simply connected fractals with low connectivity. This suggestion is made in part because the property was seen to hold for the fractals studied here, and in part due to the findings of Shima (1996). Here, Tadashi Shima demonstrates that the eigenvalues of this group of fractals can be solved analytically. Furthermore, he derives that the cumulative level distributions of such fractals have common properties, including an upper bound. As a result, it is reasonable to believe that the observed result in level spacing distribution is also a common property amongst the members of this group.

It is interesting to note that some spectral properties of the fractals were found to be determined by the integer topological dimension of the system, D_L, while others were determined by the non-integer Hausdorff dimension D_H. This shows once again that the study of fractals is highly non-trivial. One can not simply replace every appearance of dimensionality in regular equations with the fractal dimension and obtain the correct results. Rather, some properties are determined by the one, and others are determined by the other.

10.2 Outlook

In this final section, reflections on the work carried out in this thesis are included, together with some potential future directions for research in this field.

Carrying out precise calculations for the fractals brought about the demand for efficient numerical solutions and modern computational infrastructure. It was necessary to customize existing algorithms and develop new methods to optimize performance. In addition, accurate characterization and classification of fractals can be challenging. That is, knowing by which quantities to describe the fractals, and to distinguish them into different groups. This is a common problem in the treatment of fractals, and, as discussed in Section 2.2, even the very definition of a fractal is far from trivial. There are large gaps between the different fields which study fractals. The use of different terminology and methodology poses a challenge when combining results from fields such as quantum mechanics, network theory and fractal geometry.

One interesting path of investigation for a short-to-medium-term project in the field would be to look for experimental validation of the conductance results. The conductance for transport through a fractal has been shown numerically to be determined by the fractal's dimensionality. A possible realization to observe this effect could be a cold atoms experiment as suggested in Section 7.6.

Another potential path is to look into the discussed localization effects. It has been observed in this thesis that the eigenstates fluctuate rapidly between extended and localized states in small energy ranges. In condensed matter physics, the well-known phenomenon of Anderson localization describes how the introduction of disorder can inhibit the propagation of waves. At a fundamental level, this effect is about the wave nature of particles, and how these waves interact with a complex potential landscape. The result is a localization effect that is unexpected from classical particles and whose character depends on the dimensionality of the system. This prompts the question of how the localization fluctuations observed in this thesis relate to the Anderson localization in disordered quantum systems. In a periodic system, one expects delocalized bloch states and a Fourier space consisting of a single, discrete point. In the quasi-periodic case, one obtains several discrete points in the Fourier space. In a disordered system, one expects a Fourier space with states spread out over a range of momenta. There's also the possibility of a mobility edge depending on the system dimension. A guess would be that the fractals display an intermediate state between the quasi-periodic and the fully disordered. One can also imagine introducing disorder into the fractal and consider how the Anderson localization behaves as compared to integer-dimensional systems. It's important to note that the Anderson localization is typically concerned with the transition from extended to localized and not fluctuations as was discussed here. However, both effects seem to be caused by the wave properties of particles in complex potentials. Looking into this would deepen the understanding of fractals in general, as well as the cause of the localization phenomena which somehow carry the fractal dimensionality of the structure.

In the context of level spacing statistics, it would be a good next step to quantize the connectivity in fractals. One possible quantization might be made considering the number of hopping terms connecting two blocks of a fractal, divided by the minimum resolution needed to represent the fractal. These minimum resolutions depend on the fractal at hand and the iteration l considered. In the terminology of this thesis, this would be the linear grid size N in the case of $n = 1$. These resolutions can be found for some fractals in the tables of Section 4, and are also possible to evaluate directly from the generators and axioms in Appendix B. Another possibility would be to consider the tight-binding model as a complex system and use the clustering coefficient as an estimate for connectivity, or to borrow insights from network partition. Having a good measure for connectivity, one could investigate whether there exists a correlation between the slope of the decreasing power-law scaling in the level spacing distributions and the connectivity or dimension of the fractals. Studying the level spacing statistics of these systems might also help understand quantum chaos in fractals.

Some additional topics are suggested that are expected to not be within close reach. First, the work of this thesis highlighted that certain properties are determined by

the fractal dimension, while others are dictated by the topological dimension. With this in mind, a deeper exploration of what governs whether the fractal- or topological dimension is applicable is warranted. Furthermore, in the context of dimensionality, it is also interesting to expand the study to include the multifractal properties of the systems.

Finally, it is interesting to consider some of the broader implications of fractal dimensionality in physics. For instance, the Mermin-Wagner theorem states that continuous symmetries cannot be spontaneously broken in one- and two-dimensional systems at finite temperatures. This is due to thermal fluctuations. The theorem forbids, for example, having a Bose-Einstein condensate in low-dimensional systems at finite temperatures. The key question is then, how do such theorems apply to systems like the Menger Sponge, which has a dimension of 2.73?

In conclusion, there is a multitude of intriguing possibilities for future research at the intersection of quantum physics and fractal geometry. The field has broad implications for theoretical physics and is expected to bring about a variety of technological applications.

Appendix

A Numerical performance

Finding the eigenvalues of fractals numerically brings about demanding calculations. The fractals need to be created in fine detail. Furthermore, the corresponding Hamiltonian needs to be generated, which requires large amounts of memory. Finally, the eigenvalue problem must be solved. Multiple algorithms were tested and custom algorithms were also implemented to enhance performance. Some numerical considerations are included here.

The code was written in Python, but exploits C-based libraries such as Numpy, Numba and Scipy. Numba compiles Python code into optimized machine code making performance comparable to C and FORTRAN [Lam, Pitrou and Seibert (2015)]. In addition, parallel processing techniques were implemented where possible.

A.1 Choice of algorithms

To create fractals efficiently, multiple methods were tested. The Lindenmayer systems described in Section 2.4 and the Method of Repeated Kronecker Products described in Section 4.2 were eventually used. Both these methods can be implemented with high efficiency, but the latter is preferable when possible.

Generating the fractals

When employing the Lindenmayer system, the boundary of the fractal is obtained, and not the grid representation directly. Although it may seem trivial at first glance, ideally representing an arbitrary boundary on a finite grid can be a demanding process, especially in large systems. Algorithms such as the flood fill algorithm [Burtsev and Kuzmin (1993)] require the boundary coordinates to be placed directly onto the grid. Such solutions are efficient, but will however result in an imprecise representation of the object due to the boundary being enforced onto the grid.

There exist many algorithms to ideally represent an arbitrary shape on a grid. For example ray tracing method [Glassner (1989)], the point-in-polygon method, which is often made GPU based and applied in e.g. VR [Hormann and Agathos (2001)], and there are also premade methods in for example the Maplotlib library in Python. However, most Python implementations of these algorithms become staggeringly slow for the size of systems considered in this thesis. That is also when making use of libraries such as Numba and Numpy. A version of the point-in-polygon method, using parallel processing, was eventually applied. A task that took ten minutes using the method found in matplotlib.path, took roughly six seconds using this method on a basic four-core CPU laptop. This difference will become larger if more cores are available.

Representing the Hamiltonian

The viable option for representing the Hamiltonian of large systems with only neighboring interactions is using sparse dictionaries. The matrices used were of size up to 10^{16} elements. Representing each element in a double-precision floating-point format would require $10^{16} \cdot 64/8 = 80$ petabytes of memory. To further increase performance in both RAM and CPU, a reduction of the eigenvalue problem was performed. The method encompasses excluding all rows and columns that correspond to illegal points in the Hamiltonian, as well as all coupling elements coupling to such points. Had this reduced method not been employed, the most extreme cases would lead to Hamiltonians of about 10^{28} elements. This also makes the calculations less prone to swamping errors from using large and small numerical values in the same calculation. The reduced method is described in Sections 5.2 and 5.3 and the performance of this method will be treated below.

Solving the eigenvalue problem

Lastly, when solving the eigenvalue problem, different algorithms were used. When only the lowest-lying eigenvalues were of interest, the shift sigma algorithm and the Von Mises iteration were used. The numerical shift sigma algorithm uses the shift-and-invert method. Near a given value σ it computes $(A-\sigma \cdot I)x = b$ instead of $A \cdot x$. This is solved with LU decomposition for A. When looking for the ground state we want σ equal to zero. This was used in most cases. The other algorithm uses a Von Mises iteration, also called a power iteration. It chooses a linear combination of found eigenvectors that gives the smallest amplitude. Both algorithms were called through the python package *scipy.sparse*. The algorithm is chosen based on empirical performance for the given problem. That is, the first few fractal iterations are computed with both methods for a given fractal. Based on this the method which is expected to give the best results is used for the higher fractal iterations. This desired method varies for different problems.

A.2 Performance of the reduced method

When solving the eigenvalue problem, a method referred to as the *reduced method* was used. The method was introduced in Section Sections 5.2 and 5.3 and entails removing the rows and columns corresponding to illegal areas in the Hamiltonian as well as the associated coupling elements. The performance of this reduced method will be compared to evaluating the eigenvalue problem directly, which will be referred to as the *normal method*. The reduced method includes both the time of doing the transformation and applying the eigenvalue solver. The same eigenvalue solvers were used in both cases.

The transformation used to reduce the Hamiltonian is of complexity $\mathcal{O}(N^2)$, where N is the linear grid size. Furthermore, solving an eigenvalue problem has a theoretical ideal complexity of $\mathcal{O}(M^{2.376})$ [Demmel, Dumitriu and Holtz (2006)], while practical implementations of exact diagonalization typically have a complexity of roughly

$\mathcal{O}(M^3)$ [Eberly et al. (2006)]. The matrix diagonalized here is the Hamiltonian, which has elements $M = N^4$, where N is the linear grid size. Using the reduced method yields a new number of elements $\tilde{M} = \tilde{N}^4$, where $\tilde{M} \leq M$ in general. The equality holds for the completely open system.

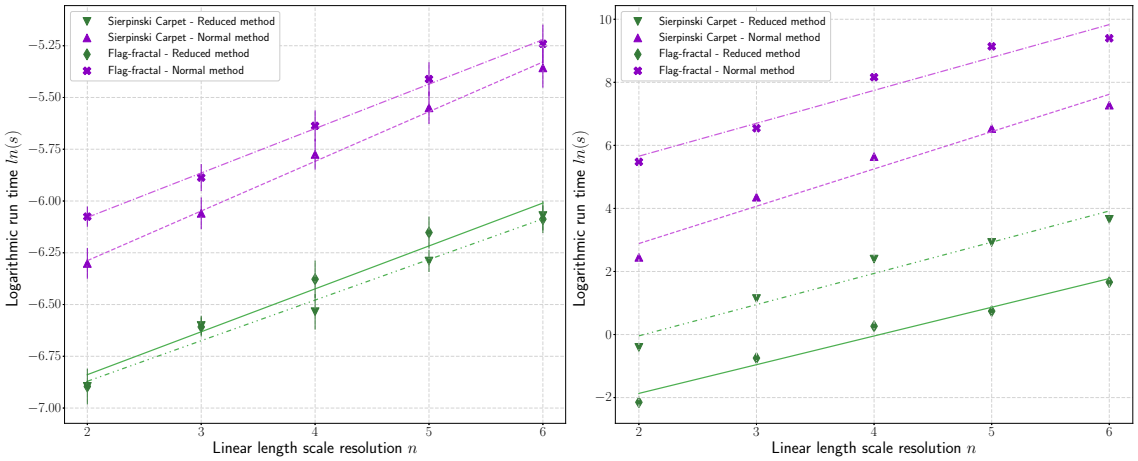
The time complexities of the two methods therefore become

$$\begin{aligned} &\text{Normal system (natural indexing)} \propto \mathcal{O}(M^3) = \mathcal{O}(N^{12}), \text{ and} \\ &\text{Reduced system (interior indexing)} \propto \mathcal{O}(N^2) \times \mathcal{O}(\tilde{M}^3) = \mathcal{O}(N^2) \times \mathcal{O}(\tilde{N}^{12}). \end{aligned} \tag{82}$$

The first factor in the reduced method is due to transformation. Furthermore, most of the considered fractals have areas that tend to zero as the fractal iteration increases. This means more and more of the grid becomes unavailable for the wave function. The reduced Hamiltonian size $\tilde{M}$ only includes the allowed points. Therefore, as the fractal's area tends to zero, $\tilde{M}$ becomes much smaller than M. One then expects the reduced method to be significantly faster than the normal method.

For a Sierpinski Gasket at fractal iteration $l = 10$, one finds $M/\tilde{M} \approx 1.784 \cdot 10^{-3}$. That means the complexity of exact diagonalization of the reduced Hamiltonian is of order $(1.784 \cdot 10^{-3})^3 \approx 5.68 \cdot 10^{-9}$ compared to the original system. This is however an extreme case. In addition, often only the lowest-lying eigenvalue was of interest, meaning that algorithms with small time-complexities were used. Therefore, to estimate the impact of the reduced method in these cases, performance tests were made.

The first few lowest-lying eigenvalues were calculated for different grid resolutions $N \times N$, for a fixed fractal at a fixed iteration l. Two different fractals are considered here, the Sierspinski Carpet and the Flag-fractal found in Sections 4.3 and 4.7, respectively. Both the reduced and the normal method were applied and the median times used in the calculation were considered for multiple runs. The estimated performances of the different methods are shown in Figures 39a and 39b for fractal iterations $l = 1$ and $l = 5$. The grid resolutions are here given by the length scale resolution n, which determines how many grid points were used to represent the smallest distance in the system. Evidently, the time of calculation increases exponentially as the grid resolution increases. The reduced method is significantly faster than the normal method for both fractals. For fractal iteration $l = 5$, it's roughly $3 - 4$ orders of magnitude faster in the case of the Sierpinski Carpet, and about 8 orders of magnitude faster in the case of the Flag-fractal. Notice that at $l = 5$, the Flag-fractal is the most demanding in the case of the normal method, but the most efficient using the reduced method. The ordering is not the same in the case of $l = 1$. The reason for this was briefly mentioned in Section 4.7. The Flag-fractal becomes detailed very rapidly with increasing l, with minimal grid resolutions following (62). However, the area of the allowed region also tends to zero fast. This means that many rows and columns can be removed from the Hamiltonian using the transformation in the reduced method.



(a) Fractal iteration $l = 1$ (b) Fractal iteration $l = 5$

Figure 39: The first few lowest-lying eigenvalues were evaluated for the Sierpinski Carpet and the Flag-fractal, and the times used in the numerical calculations were considered. The median performance times after multiple runs are shown. In the plot, a comparison is made between the reduced method and the normal method for varying different resolutions n at fixed fractal iterations l. In (a), a fractal iteration $l = 1$ is used, and in (b), a fractal iteration of $l = 5$ is used. Notice that the flag fractal in the reduced method is the fastest method in (b), while the normal method for the same fractal is the slowest.

For a given fractal iteration, the percentage of points that can be removed remains constant over different resolutions n. Therefore, the complexities of the different methods have the same exponential evolutions with increasing grid resolution. That is, the plots in Figure 39 are all linear, and have approximately the same slope.

Next, choose a constant value of the length scale resolution n and vary the fractal iteration l. The performances of the different methods for the two fractals are shown in Figure 40. When increasing the fractal iteration l, the percentage of points that can be removed in the reduced method also increases. The effect of the reduced method, therefore, becomes gradually more and more significant. Because of this, the slopes in Figure 40 are no longer of the same shape and with a constant shift between them, as was the case for the results when varying grid resolutions. Instead, it is seen that the complexity of the normal method grows faster than that of the reduced method. This demonstrates why the reduced method is especially useful when considering large fractal iterations of fractals with a vanishing area.

The reduced method works especially well for the Flag-fractal. However, most fractals considered in this project thesis have vanishing areas as the fractal iteration l increases. In all these cases, the reduced method is considerably faster than the normal method.

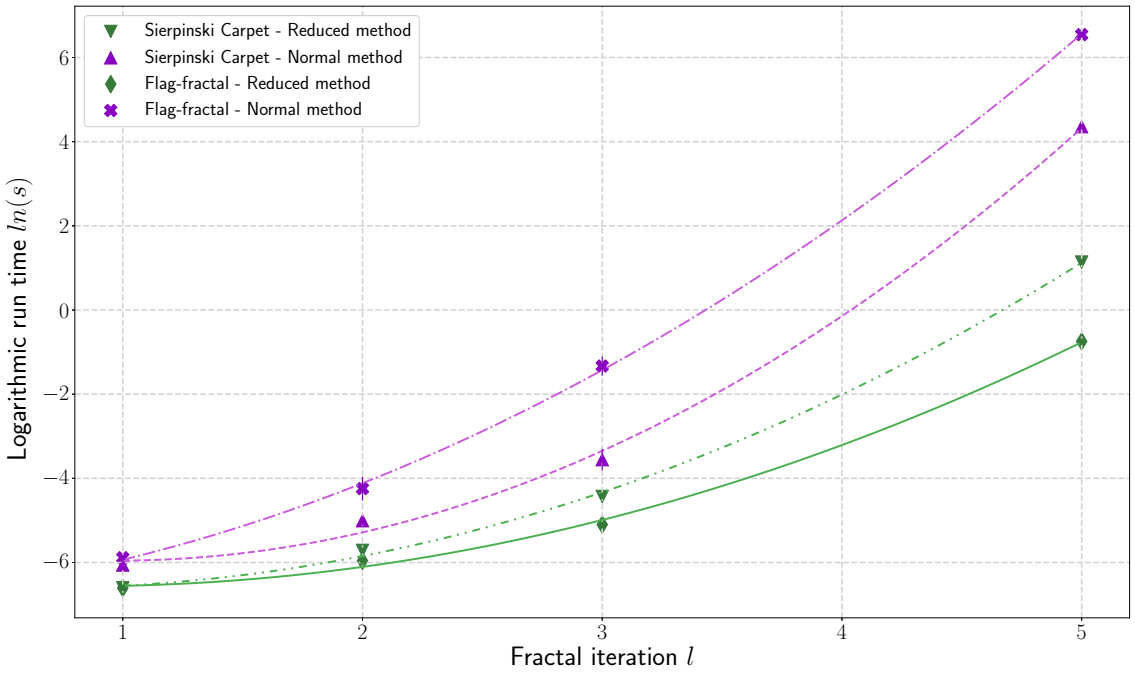
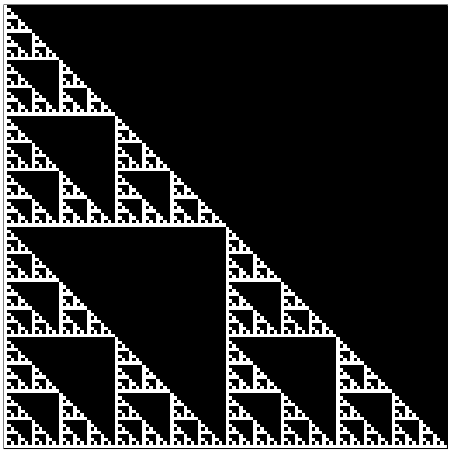


Figure 40: The numerical performances when solving the lowest-lying eigenvalues of the Sierpinski Carpet and the Flag-fractal for varying fractal iterations. The plot is equivalent to Figure 39, only now varying the iteration l instead of the grid resolution n. The two methods called the reduced method and the normal method are compared. Multiple runs were made and the median of the total run times of the methods are used. The complexity of the normal method grows faster than that of the reduced method. The lines between points are second-order fits and are only added to assist visualization. It does not make sense to extract values at non-integer values of l.

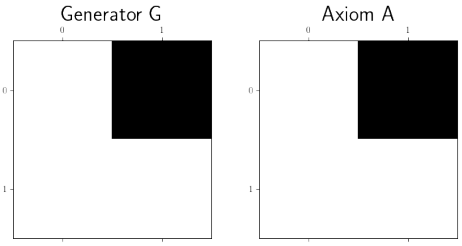
B Additional fractals

Some fractals were discussed in depth in Section 4. The remaining fractals are included below. The fractals were generated using the repeated Kronecker Product method described in Section 4.2. Their generators, axioms and Hausdorff dimensions are given along with images at intermediate fractal iterations.

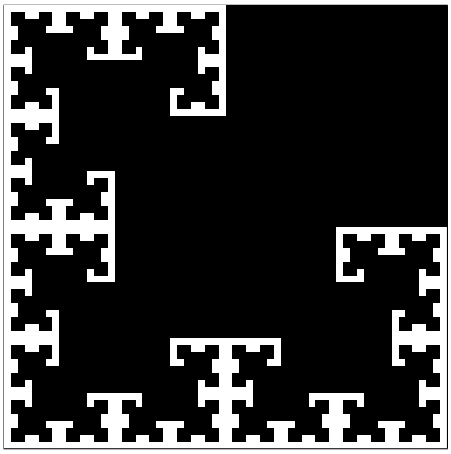
Sierpinski gasket. Fractal iteration $l = 6$.



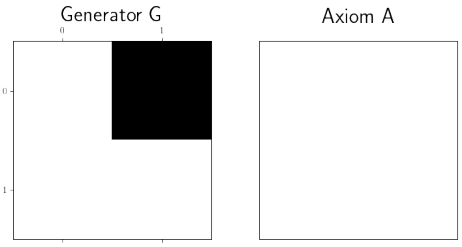
$D_H = \frac{\log(m)}{\log(r)} \approx 1.58$



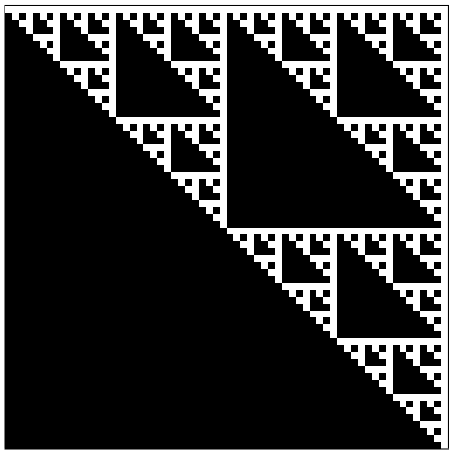
T-fractal. Fractal iteration $l = 6$.
The T-fractal is created similarly to the Sierpinski Gasket, but after each application of the generator, the upper left quarter is rotated 90° clockwise and the lower right corner is rotated 90° counterclockwise.



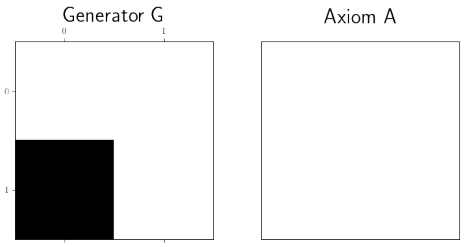
$D_H = \frac{\log(m)}{\log(r)} \approx 1.58$



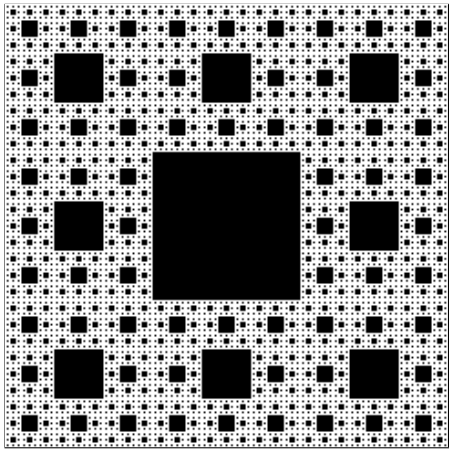
Remove lower left. Fractal iteration $l = 6$.



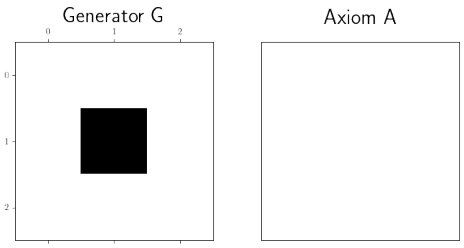
$D_H = \frac{\log(m)}{\log(r)} \approx 1.58$



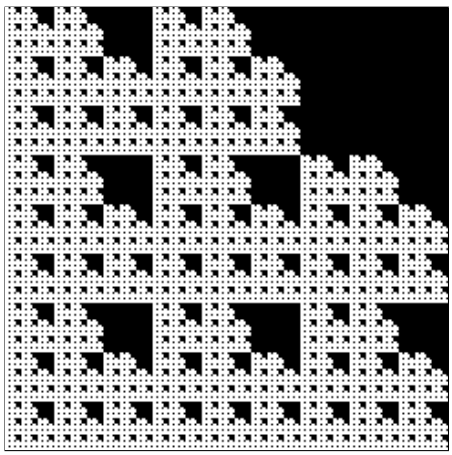
Sierpinski Carpet. Fractal iteration $l = 5$.



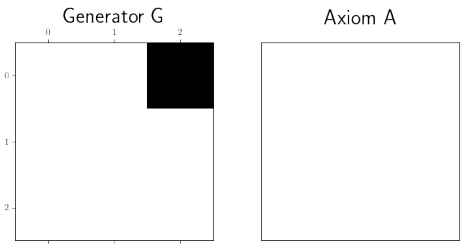
$D_H = \frac{\log(m)}{\log(r)} \approx 1.89$



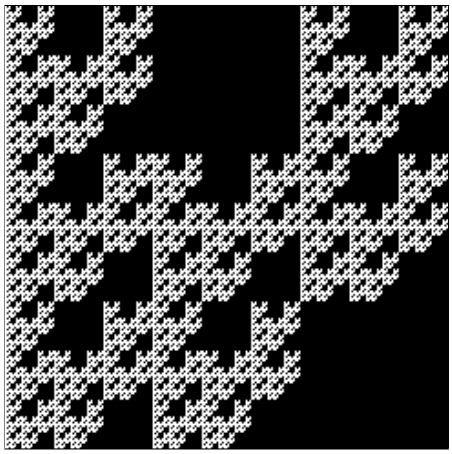
Dilute Corner Cutting. Fractal iteration $l = 5$.



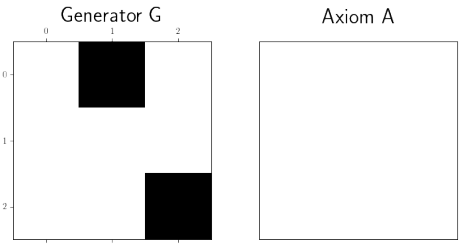
$D_H = \frac{\log(m)}{\log(r)} \approx 1.89$



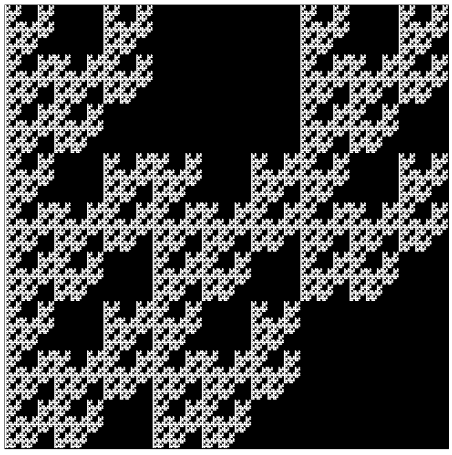
Bush. Fractal iteration $l = 5$.



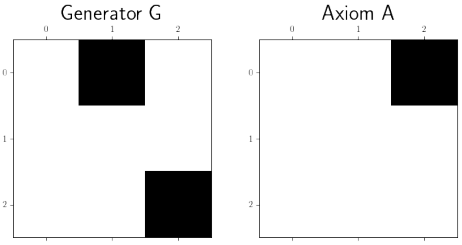
$$D_H = \frac{\log(m)}{\log(r)} \approx 1.77$$



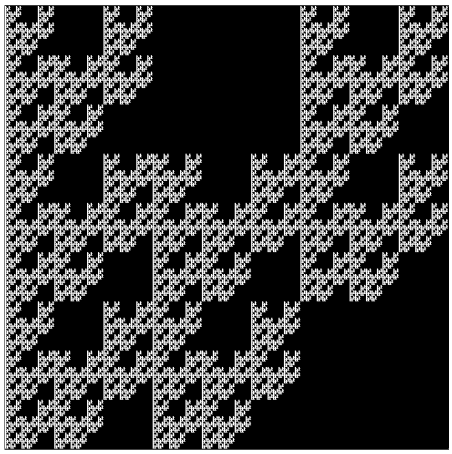
Trimmed Bush 1. Fractal iteration $l = 5$.



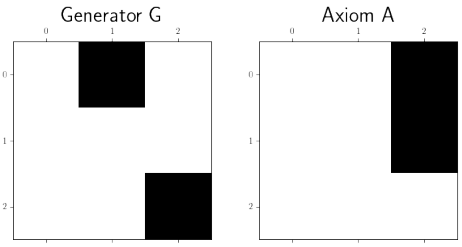
$$D_H = \frac{\log(m)}{\log(r)} \approx 1.77$$



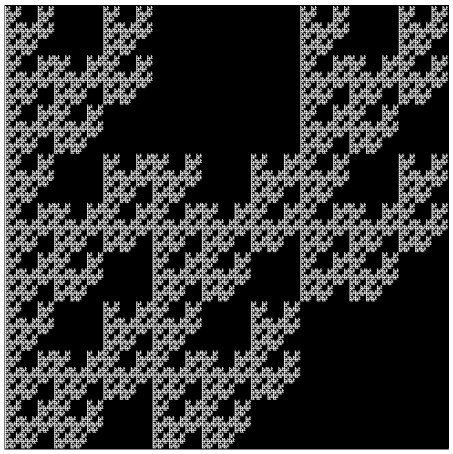
Trimmed Bush 2. Fractal iteration $l = 5$.



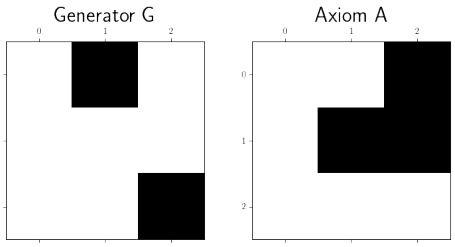
$$D_H = \frac{\log(m)}{\log(r)} \approx 1.77$$



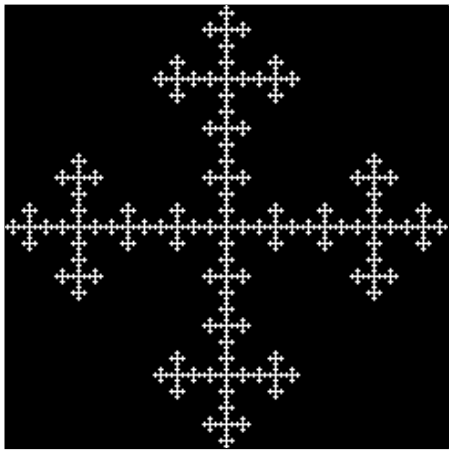
Trimmed Bush 3. Fractal iteration $l = 5$.



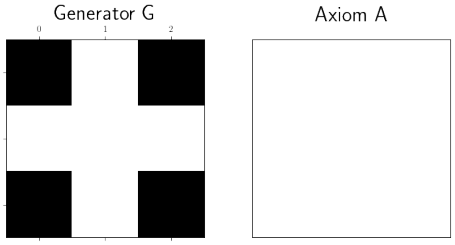
$$D_H = \frac{\log(m)}{\log(r)} \approx 1.77$$



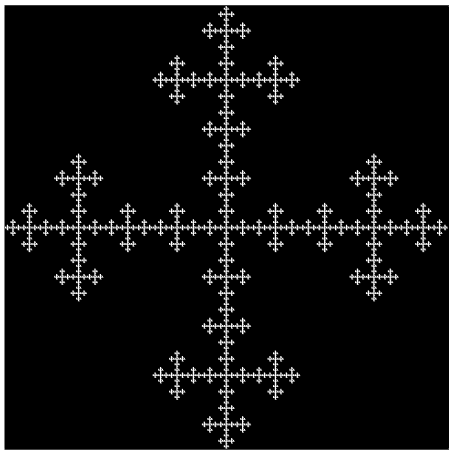
Jerusalem Cross. Fractal iteration $l = 5$.



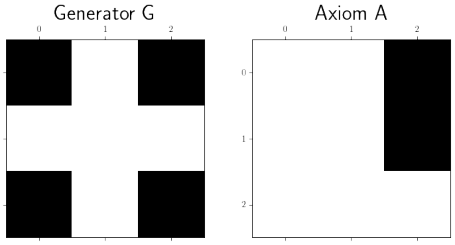
$$D_H = \frac{\log(m)}{\log(r)} \approx 1.46$$



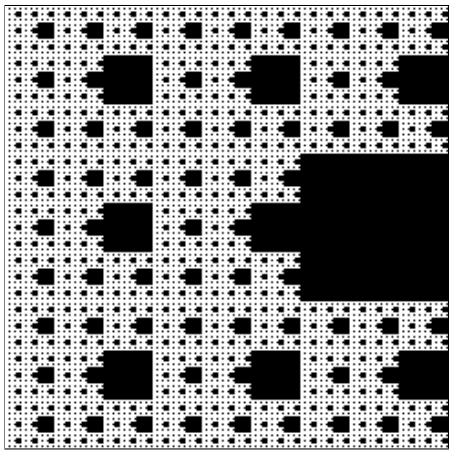
Unorthodox Cross. Fractal iteration $l = 5$.



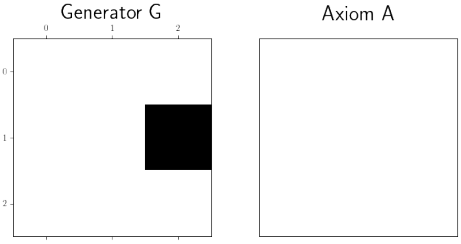
$$D_H = \frac{\log(m)}{\log(r)} \approx 1.46$$



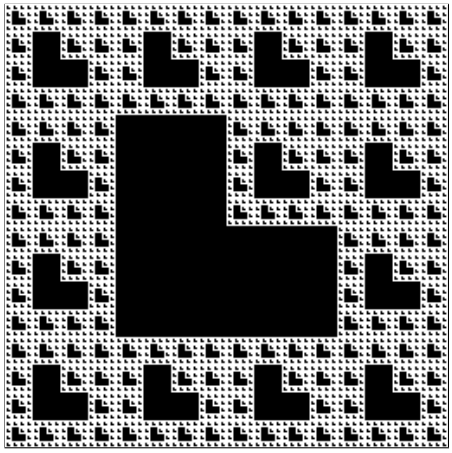
Alien Invasion. Fractal iteration $l = 5$.



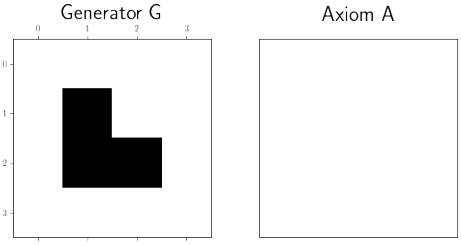
$D_H = \frac{\log(m)}{\log(r)} \approx 1.89$



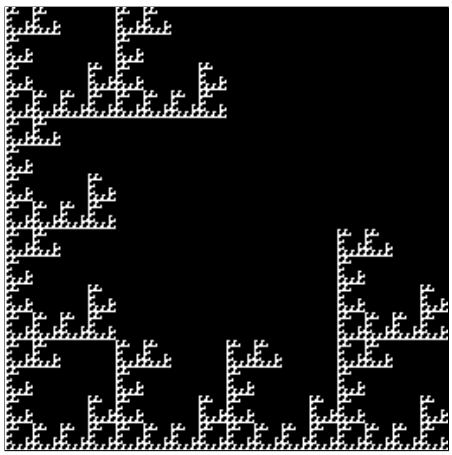
Cutting Corners. Fractal iteration $l = 4$.



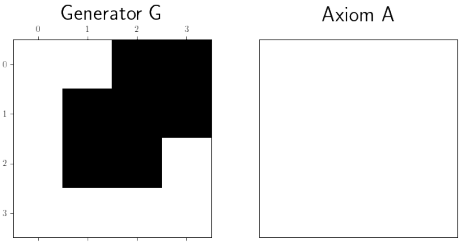
$D_H = \frac{\log(m)}{\log(r)} \approx 1.85$



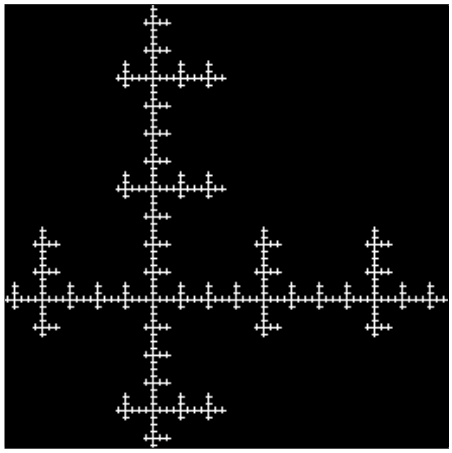
Strange Trees. Fractal iteration $l = 4$.



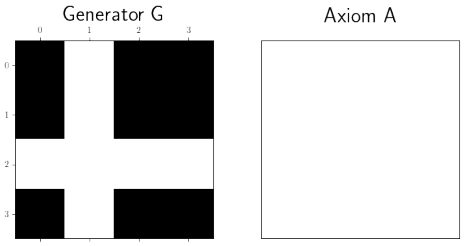
$D_H = \frac{\log(m)}{\log(r)} \approx 1.58$



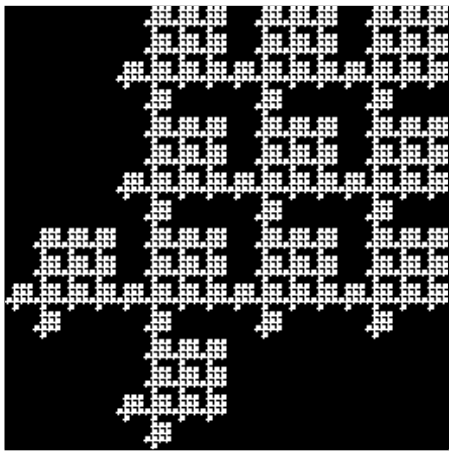
Flag-fractal. Fractal iteration $l = 4$.



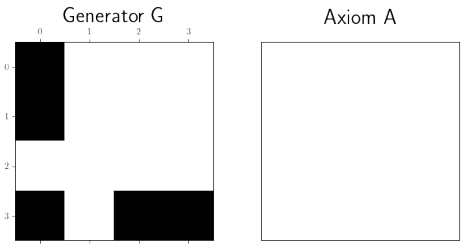
$D_H = \frac{\log(m)}{\log(r)} \approx 1.40$



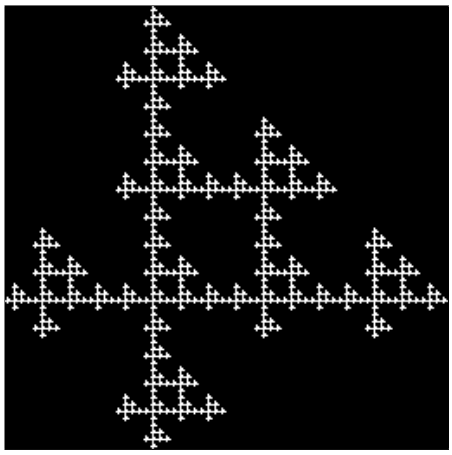
Fish. Fractal iteration $l = 4$.



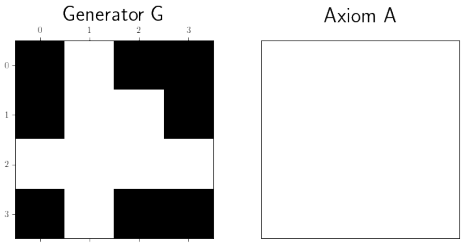
$D_H = \frac{\log(m)}{\log(r)} \approx 1.73$



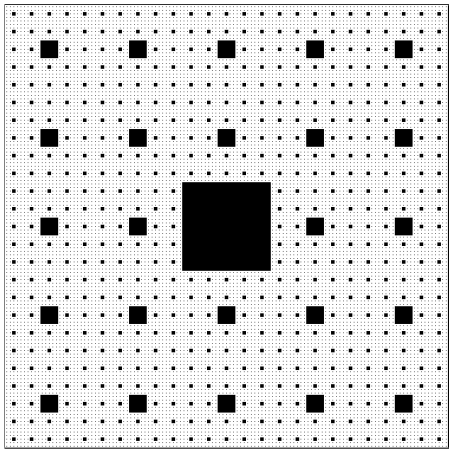
Sail. Fractal iteration $l = 4$.



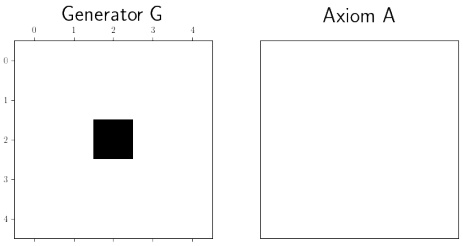
$D_H = \frac{\log(m)}{\log(r)} \approx 1.50$



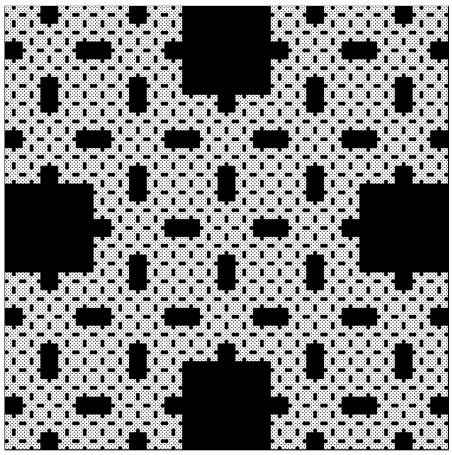
Dilute Carpet. Fractal iteration $l = 4$.



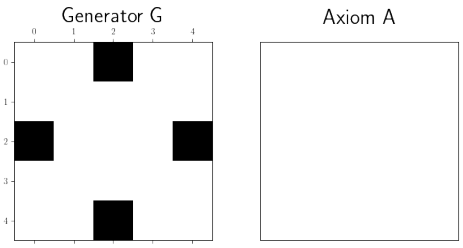
$D_H = \frac{\log(m)}{\log(r)} \approx 1.97$



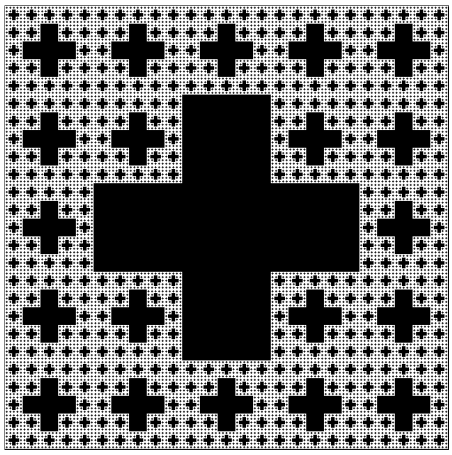
Bacteria. Fractal iteration $l = 4$.



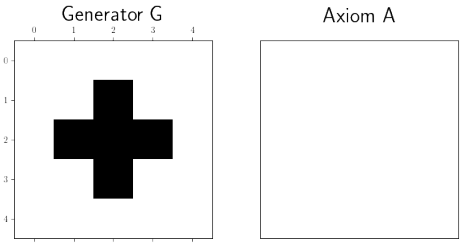
$D_H = \frac{\log(m)}{\log(r)} \approx 1.89$



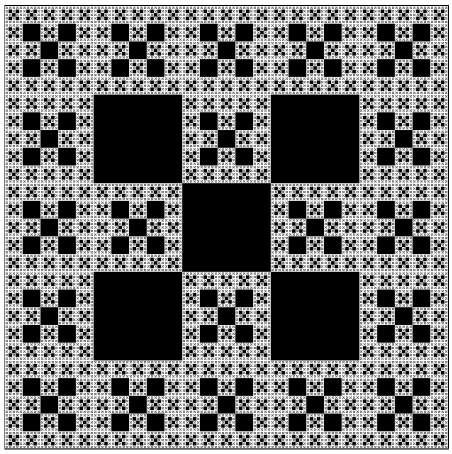
Vicsek Saltire. Fractal iteration $l = 4$.



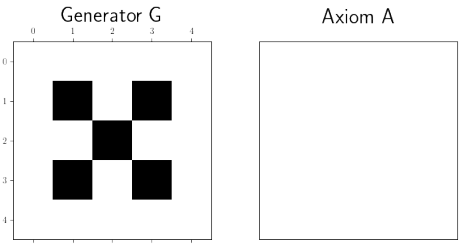
$D_H = \frac{\log(m)}{\log(r)} \approx 1.86$



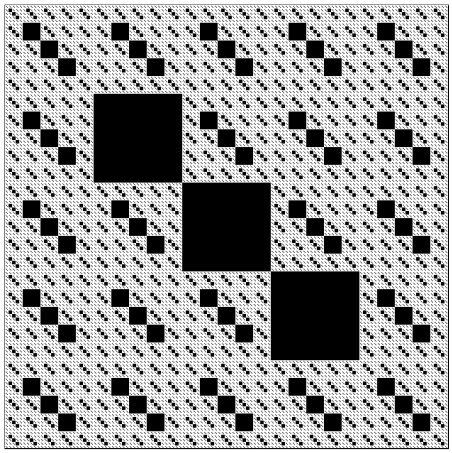
Vicsek Cross. Fractal iteration $l = 4$.



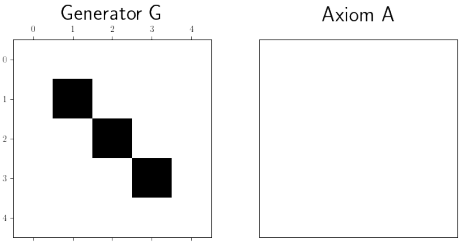
$$D_H = \frac{\log(m)}{\log(r)} \approx 1.86$$



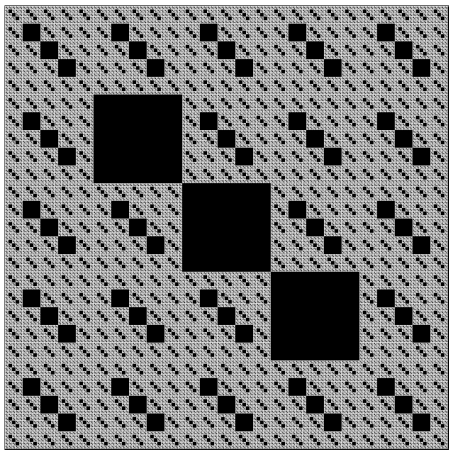
Cut Cross. Fractal iteration $l = 4$.



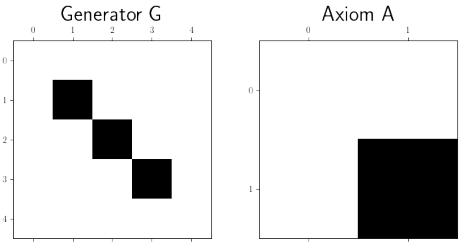
$$D_H = \frac{\log(m)}{\log(r)} \approx 1.92$$



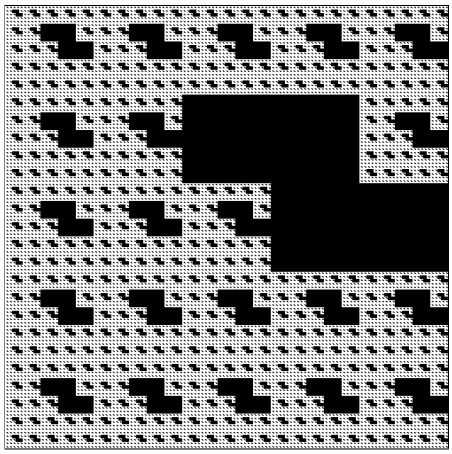
Quiver. Fractal iteration $l = 4$.



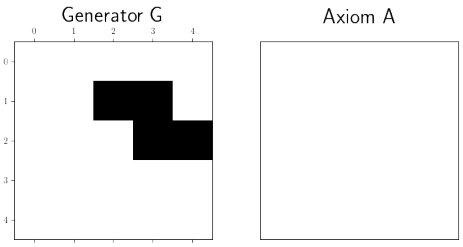
$$D_H = \frac{\log(m)}{\log(r)} \approx 1.92$$



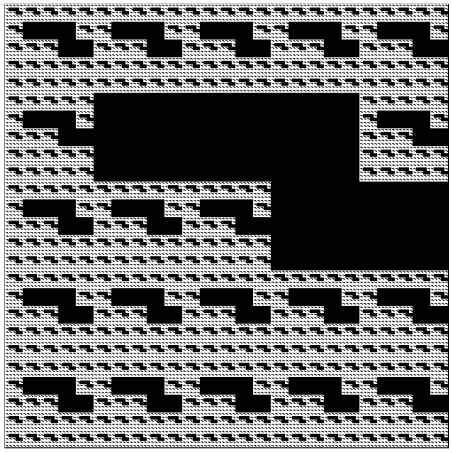
Snake. Fractal iteration $l = 4$.



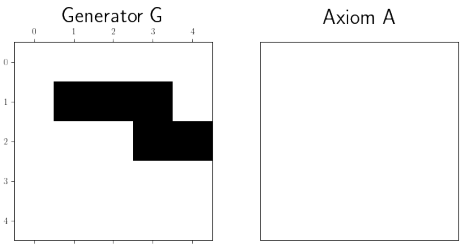
$$D_H = \frac{\log(m)}{\log(r)} \approx 1.89$$



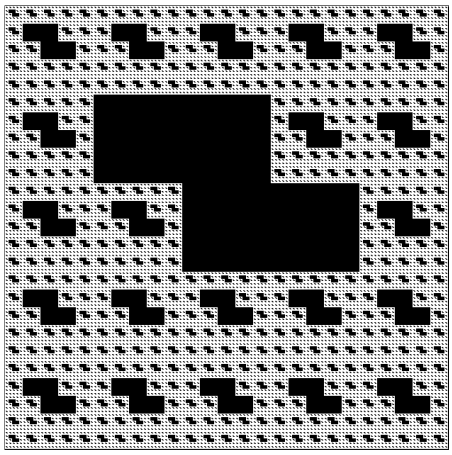
Big Snake. Fractal iteration $l = 4$.



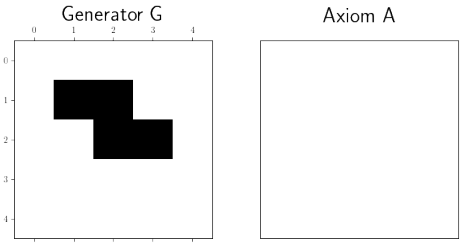
$$D_H = \frac{\log(m)}{\log(r)} \approx 1.86$$



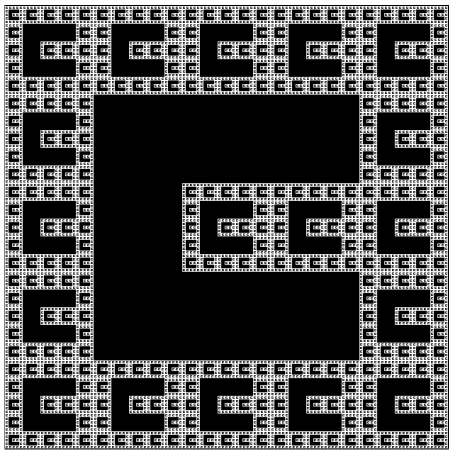
Central Snake. Fractal iteration $l = 4$.



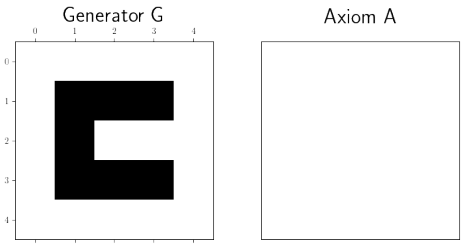
$$D_H = \frac{\log(m)}{\log(r)} \approx 1.89$$



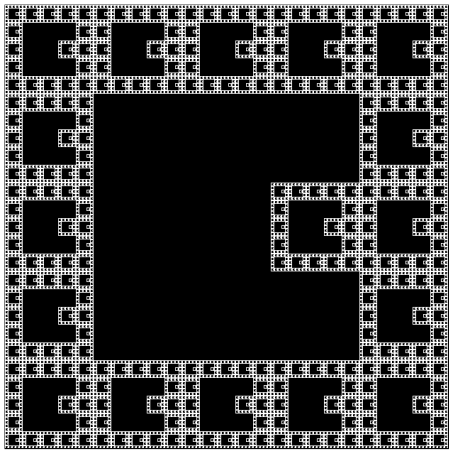
Pacman. Fractal iteration $l = 4$.



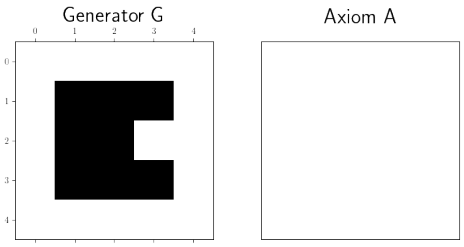
$$D_H = \frac{\log(m)}{\log(r)} \approx 1.80$$



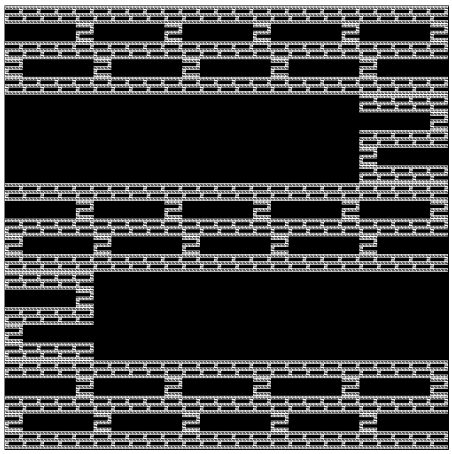
Pacman Variant. Fractal iteration $l = 4$.



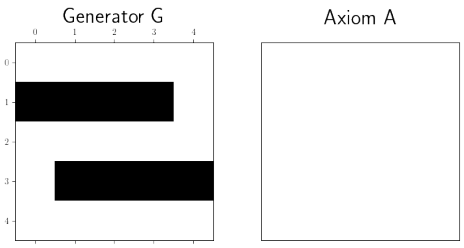
$$D_H = \frac{\log(m)}{\log(r)} \approx 1.76$$



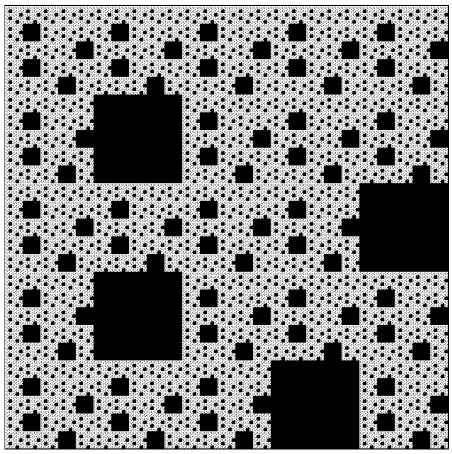
Hardly Connected. Fractal iteration $l = 4$.



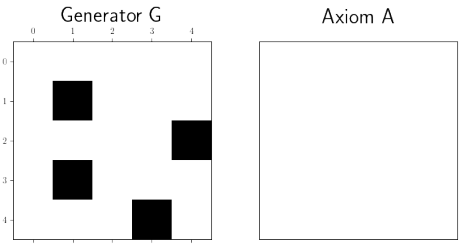
$$D_H = \frac{\log(m)}{\log(r)} \approx 1.76$$



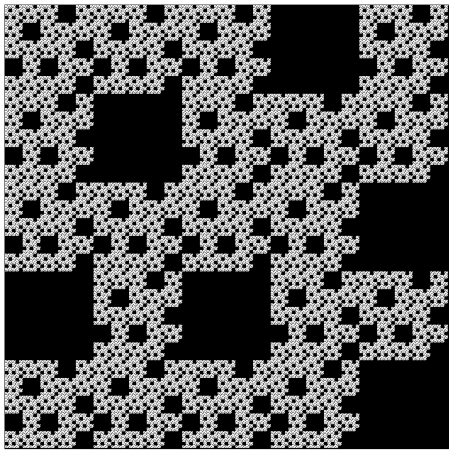
Bombardment 1. Fractal iteration $l = 4$.



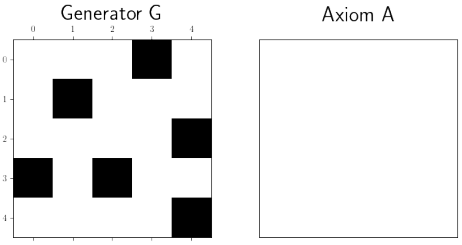
$D_H = \frac{\log(m)}{\log(r)} \approx 1.89$



Bombardment 2. Fractal iteration $l = 4$.



$D_H = \frac{\log(m)}{\log(r)} \approx 1.83$



Bibliography

Adams, R. (2013). *Calculus: A complete course* (8th ed.). Pearson Education.

Aidelsburger, M., Atala, M., Lohse, M., Barreiro, J. T., Paredes, B., & Bloch, I. (2013). Realization of the hofstadter hamiltonian with ultracold atoms in optical lattices. *Phys. Rev. Lett.*, *111*(18), 185301. https://doi.org/10.1103/PhysRevLett.111.185301

Akre, F. E. (2023). Project thesis, spectral properties of quantum particles in fractal potentials [Unpublished. Available upon request]. *Department of physics, Norwegian University of Science Technology & Polytechnic University of Catalonia*.

Azeez, A., Jabbar, S., & Wang, D. (2016). Fractal antennas (study and review). *International Journal of Computers & Technology*, *15*, 7387–7400. https://doi.org/10.24297/ijct.v15i13.31

Billingsley, P. (1995). *Probability and measure* (3rd ed.). John Wiley; Sons.

Bresenham, J. E. (1965). Algorithm for computer control of a digital plotter. *IBM Systems Journal*, *4*(1), 25–30. https://doi.org/10.1147/sj.41.0025

Brewer, J. (1978). Kronecker products and matrix calculus in system theory. *IEEE Transactions on Circuits and Systems*, *25*(9), 772–781. https://doi.org/10.1109/TCS.1978.1084534

Budroni, M. A., Baronchelli, A., & Pastor-Satorras, R. (2017). Scale-free networks emerging from multifractal time series. *Phys. Rev. E*, *95*(5), 052311. https://doi.org/10.1103/PhysRevE.95.052311

Burtsev, S., & Kuzmin, Y. P. (1993). An efficient flood-filling algorithm. *Computers & Graphics*, *17*(5), 549–561.

Büttiker, M. (1988). Absence of backscattering in the quantum hall effect in multiprobe conductors. *Phys. Rev. B*, *38*(14), 9375–9389. https://doi.org/10.1103/PhysRevB.38.9375

Cantor, G. (1883). Über unendliche, lineare punktmannichfaltigkeiten. *Mathematische Annalen*, *21*, 541–591.

Carathéodory, C. (1913). *Vorlesungen über reelle funktionen* (2nd ed.). Teubner Verlag Wiesbaden. https://doi.org/10.1007/978-3-663-15768-7

Datta, S. (1995). *Electronic transport in mesoscopic systems*. Cambridge University Press. https://doi.org/10.1017/CBO9780511805776

Datta, S. (2005). *Quantum transport: Atom to transistor*. Cambridge University Press. https://doi.org/10.1017/CBO9781139164313

Dean, C., Wang, L., Maher, P., Forsythe, C., Ghahari, F., Gao, Y., Katoch, J., Ishigami, M., Moon, P., Koshino, M., Taniguchi, T., Watanabe, K., Shepard, K., Hone, J., & Kim, P. (2013). Hofstadter's butterfly and the fractal quantum hall effect in moire superlattices. *Nature*, *497*, 598. https://doi.org/10.1038/nature12186

Demmel, J., Dumitriu, I., & Holtz, O. (2006). Fast linear algebra is stable. *Numerische Mathematik*, *108*, 59–91. https://doi.org/10.1007/s00211-007-0114-x

Dyson, F. (1962). A brownian-motion model for the eigenvalues of a random matrix. *Journal of Mathematical Physics*, *3*, 1191. https://doi.org/10.1063/1.1703862

Eberly, W., Giesbrecht, M., Giorgi, P., Storjohann, A., & Villard, G. (2006). Solving sparse integer linear systems. *arXiv*. https://doi.org/10.48550/ARXIV.CS/0603082

Edgar, G. A. (2008). *Measure topology and fractal geometry* (2nd ed.). Springer.

Falconer, K. (2003). *Fractal geometry:: Mathematical foundations and applications* (3rd ed.). John Wiley & Sons, Ltd. https://doi.org/10.1002/0470013850

Glassner, A. S. (Ed.). (1989). *An introduction to ray tracing*. Academic Press Ltd.

Groth, C. W., Wimmer, M., Akhmerov, A. R., & Waintal, X. (2014). Kwant: A software package for quantum transport. *New Journal of Physics*, *16*(6), 063065. https://doi.org/10.1088/1367-2630/16/6/063065

Gutzwiller, M. C. (1990). *Chaos in classical and quantum mechanics*. Springer. https://doi.org/10.1007/978-1-4612-0983-6

Haake, F. (2010). *Quantum signatures of chaos* (3rd ed.). Springer.

Hardt, G. H. (1916). Weierstrass's non-differentiable function. *Transactions of the American Mathematical Society*, *17*(3), 301–325. https://doi.org/10.2307/1989005

Hatsuda, Y., Katsura, H., & Tachikawa, Y. (2016). Hofstadter's butterfly in quantum geometry. *New Journal of Physics*, *18*(10), 103023. https://doi.org/10.1088/1367-2630/18/10/103023

Havlin, S., & Ben-Avraham, D. (1987). Diffusion in disordered media. *Advances in Physics*, *36*(6), 695–798. https://doi.org/10.1080/00018738700101072

Hemmer, P. C. (2005). *Kvantemekanikk* (5th ed.). Tapir akademisk forlag.

Hofstadter, D. R. (1976). Energy levels and wave functions of bloch electrons in rational and irrational magnetic fields. *Phys. Rev. B*, *14*(6), 2239–2249. https://doi.org/10.1103/PhysRevB.14.2239

Hormann, K., & Agathos, A. (2001). The point in polygon problem for arbitrary polygons. *Computational Geometry*, *20*, 131–144. https://doi.org/10.1016/S0925-7721(01)00012-8

Hutchinson, J. E. (1981). Fractals and self similarity. *Mathematics Journal*, *30*, 713–747.

Iliasov, A. A., Katsnelson, M. I., & Yuan, S. (2019). Power-law energy level spacing distributions in fractals. *Phys. Rev. B*, *99*(7), 075402. https://doi.org/10.1103/PhysRevB.99.075402

Iliasov, A. A., Katsnelson, M. I., & Yuan, S. (2020). Linearized spectral decimation in fractals. *Phys. Rev. B*, *102*(7), 075440. https://doi.org/10.1103/PhysRevB.102.075440

Jiang, S., & Liu, D. (2012). Box-counting dimension of fractal urban form: Stability numbers and measurement design. *International Journal of Artificial Life Research*, *3*, 41–63. https://doi.org/10.4018/jalr.2012070104

Johnson, P. E. (1972). The genesis and development of set theory. *The Two-Year College Mathematics Journal*, *3*, 55–62.

Kempkes, S., Slot, M., Freeney, S., Zevenhuizen, S., Vanmaekelbergh, D., Swart, I., & Morais Smith, C. (2019). Design and characterization of electrons in a fractal geometry. *Nature Physics*, *15*, 127–131. https://doi.org/10.1038/s41567-018-0328-0

Krinner, S., Esslinger, T., & Brantut, J.-P. (2017). Two-terminal transport measurements with cold atoms. *Journal of Physics: Condensed Matter*, *29*(34), 343003. https://doi.org/10.1088/1361-648x/aa74a1

Krinner, S., Stadler, D., Husmann, D., Brantut, J.-P., & Esslinger, T. (2015). Observation of quantized conductance in neutral matter. *Nature*, *517*, 64–67. https://doi.org/10.1038/nature14049

Lam, S. K., Pitrou, A., & Seibert, S. (2015). Numba: A llvm-based python jit compiler. *Proceedings of the Second Workshop on the LLVM Compiler Infrastructure in HPC*, 1–6.

Landauer, R. (1957). Spatial variation of currents and fields due to localized scatterers in metallic conduction. *IBM Journal of Research and Development*, *1*(3), 223–231. https://doi.org/10.1147/rd.13.0223

Lindenmayer, A. (1968). Mathematical models for cellular interactions in development i. filaments with one-sided inputs. *Journal of Theoretical Biology*, *18*(3), 280–299. https://doi.org/10.1016/0022-5193(68)90079-9

Lorenz, E. N. (1963). Deterministic nonperiodic flow. *Journal of Atmospheric Sciences*, *20*(2), 130–141. https://doi.org/10.1175/1520-0469(1963)020⟨0130:DNF⟩2.0.CO;2

Mandelbrot, B. B. (1982). *The fractal geometry of nature*. W.H Freeman; Company.

Mehta, M. L. (1967). *Random matrices* (1st ed.). Academic Press New York; London.

Mehta, M. L. (2004). *Random matrices* (3rd ed.). Elsevier Academic Press.

Ni, X., Chen, K., Weiner, M., Apigo, D., Prodan, E., Alù, A., Khanikaev, A., & Prodan, C. (2019). Observation of hofstadter butterfly and topological edge states in reconfigurable quasi-periodic acoustic crystals. *Communications Physics*, *2*, 55. https://doi.org/10.1038/s42005-019-0151-7

Press, W., Teukolsky, S., Vetterling, W., & Flannery, B. (2007). *Numerical recipes: The art of scientific computing* (3rd ed.). Cambridge University Press.

Priyadarshinee, P., Lim, K., & Lee, H. (2018). Fractal diffusers as noise barrier top-edge devices. *Journal of Physics: Conference Series*, *1075*, 012032. https://doi.org/10.1088/1742-6596/1075/1/012032

Rényi, A. (1961). On measures of entropy and information. *Proceedings of the Fourth Berkeley Symposium on Mathematical Statistics and Probability*, *1*, 547–561.

Roe, E., Bies, A., Montgomery, R., Watterson, W., Parris, B., Boydston, C., Sereno, M., & Taylor, R. (2020). Fractal solar panels: Optimizing aesthetic and electrical performances. *PLOS ONE*, *15*, e0229945. https://doi.org/10.1371/journal.pone.0229945

Samavati, H., Hajimiri, A., Shahani, A., Nasserbakht, G., & Lee, T. (1998). Fractal capacitors. *IEEE Journal of Solid-State Circuits*, *33*(12), 2035–2041. https://doi.org/10.1109/4.735545

Sauer, T. (2011). *Numerical analysis* (2nd ed.). Pearson plc.

Shima, T. (1996). On eigenvalue problems for laplacians on p.c.f. self-similar sets. *Japan Journal of Industrial and Applied Mathematics*, *13*, 1–23.

Strogatz, S. (2015). *Nonelinear dynamics and chaos : With applications to physics, biology, chemistry, and engineering*. Westview Press.

Sutherland, W. A. (2009). *Introduction to metric and topological spaces* (2nd ed.). Oxford University Press.

Tao, T. (2011). *An introduction to measure theory*. American Mathematical Society.

van Veen, E., Yuan, S., Katsnelson, M. I., Polini, M., & Tomadin, A. (2016). Quantum transport in sierpinski carpets. *Phys. Rev. B*, *93*(11), 115428. https://doi.org/10.1103/PhysRevB.93.115428

Weierstrass, K. (2013). *Mathematische werke: Herausgegeben unter mitwirkung einer von der königlich preussischen akademie der wissenschaften eingesetzten commission*. Cambridge University Press. https://doi.org/10.1017/CBO9781139567817.006

Wigner, E. P. (1955). Characteristic vectors of bordered matrices with infinite dimensions. *Annals of Mathematics*, *62*(3), 548–564.

Zhiwei, H., Hwang, Y., Aute, V., & Radermacher, R. (2016). Review of fractal heat exchangers. *Conference: International Refrigeration and Air*, 10.



NTNU
Norwegian University of
Science and Technology

UPC
UNIVERSITAT POLITÈCNICA
DE CATALUNYA